BUBBLE DYNAMICS IN A COMPRESSIBLE VISCOUS LIQUID

by

WENKE LIU

A thesis submitted to

The University of Birmingham

for the degree of

DOCTOR OF PHILOSOPHY

School of Mathematics

The University of Birmingham

September 2017

Abstract

Microbubble dynamics are associated with cavitation damage to pumps, turbines and propellers, as well as applications in biomedical ultrasonics, sonochemistry and cavitation cleaning. The compressible effects of liquid are essential, which are associated with acoustic radiation at the inception of a bubble and the end of collapse. Viscous effects are important for microbubbles. This thesis is concerned with microbubble dynamics in a viscous compressible liquid near a rigid boundary. The compressible effects are modelled by using the weakly compressible theory of Wang & Blake [103, 104]. The viscous effects are approximated using the viscous potential flow theory of Joseph & Wang [29], because the flow field is characterised as being an irrotational flow in the bulk volume but with a thin viscous boundary layer at the bubble surface. Consequently, the phenomenon is modelled by using the boundary integral method. The numerical results are shown in good agreement with the Keller-Miksis equation, experiments and computations based on the Navier-Stokes equations. Numerical studies were carried out for microbubble dynamics near a rigid boundary as well as subject to an acoustic wave. The bubble oscillation, topological transform, jet development and penetration through the bubble and the energy of the bubble system are simulated and analysed regarding the compressible and viscous effects.

Acknowledgements

I would like to thank my project supervisor, Dr Qianxi Wang, for his constants support. It is a pleasure working with them and, most importantly, he has made working on this project enjoyable.

I also need to express my sincere appreciation to my parents and my girlfriend Li Shem who supported me to complete the long journey. They cherished me every single moment and supported me whenever I needed.

Contents

Chapter 1

INTRODUCTION

1.1 Research Background

The study of bubble dynamics in the neighbourhood of a rigid boundary is associated with cavitation erosion to propellers, turbines and pumps [84, 41, 110, 74, 44, 67]. The cavitation damage mechanism is believed to be associated with shock waves [87, 94] and bubble jetting [63, 83], both of which are formed at the end of collapse. Similarly, the damage mechanism of an underwater explosion is associated with a shock wave emitted at the inception of an underwater explosion bubble and bubble jetting formed at the end of collapse [52, 65, 59]. Gas-filled bubbles can be found not only in some natural processes such as fermentation, boiling and sedimentation but also within several aspects, for instance, fluidised beds and nucleate boiling reactors.

Recent research on ultrasound cavitation bubbles is associated with several important medical applications, including extracorporeal shock wave lithotripsy [55, 64, 47, 60, 75, 76], tissue ablating [88, 53, 54], and oncology and cardiology [73]. In these applications, cavitation microbubbles absorb and concentrate a significant amount of energy from ultrasound, leading to shape oscillation, shock waves, violent collapsing and strong bubble jetting [22]. These

mechanisms are also associated with sonochemistry [91, 92] and ultrasound cavitation cleaning which is one of the most effective cleaning processes for electrical and medical micro-devices [86, 90].

In spite of their size (usually of the order 1 μm), cavitation bubbles demonstrate extreme physical feature with immense pressure and temperatures during collapse (although over tiny timescales). Their tendency of focusing and concentrating energy, focus and stresses as well as emission of shockwaves means they could potentially damage the nearby surface structures.When a bubble oscillates near a rigid boundary, the liquid jet can be formed when the bubble collapses in the asymmetry fluid flow. The parameters of the surface will determine the direction of the liquid jet. If the bubble is too close to the rigid boundary, it will lead to the direct impact of the jet on the rigid wall. When the bubble initially is a little bit far away from the rigid boundary the jet will impact on another side of the bubble and release a shockwave. Because the expanding and collapsing of the bubble occurs very abruptly in microseconds, it is difficult to observe this process and the exact mechanisms of cavitation damage are still unknown. According to the studies of Chen and Israelachvili [121], which have been shown that damage to a nearby rigid wall, can be more likely to take place during the formation of cavities. It is obvious that acquiring sufficient understanding of cavitation damage is vital to many biomedical, chemical and engineering applications.

1.2 Previous works

Controlling and understanding the dynamics of the bubbles, on the other hand, assists us to learn their ubiquitous nature, and on the other hand, facilitates their application in intensifying chemical or physical processes. The boundary integral method (BIM) is grid-free in the flow

domain and computationally efficient and is thus widely used in the field of bubble dynamics. It has been applied for bubble dynamics near a free surface or compliant surface in axisymmetric configuration [7, 41-43, 45, 56-58, 71, 77-78, 81, 105, 111-112] as well as in three dimensional configuration [36, 48-51, 65, 61-62, 98-99]. The axisymmetric BIM was employed to study acoustic bubble dynamics in an infinite fluid [64, 103-104] and close to a rigid boundary subject to ultrasound which propagates perpendicularly to the rigid boundary [18-19, 20-21, 7]. Dynamics of a bubble close to a rigid wall driven by ultrasound which propagating parallel to the wall were modelled by the three dimensional BIM [22].

Compressible effects

The BIM model is suitable for incompressible flow and does not account for the significant energy loss due to the emission of shock waves associated with bubble dynamics. Lee et al. [70] modified the BIM model by removing a part of the bubble potential energy empirically at the end of the first cycle of oscillation.

A bubble initiated near a rigid boundary can be almost in contact with the boundary because of its expansion and migration to the boundary as a result of the attraction by the second Bjerknes force [82]. This leads to the direct impact of a liquid jet on the boundary once it penetrates through the bubble, the direct contact of the bubble at the minimum volume at high pressure and high temperature with the boundary, and the direct impingement of shock waves on the boundary once emitted. We believe that these phenomena have clear damage potential to the boundary. It is, therefore, very important to study bubble dynamics in near contact with a rigid boundary.

Prosperetti & Lezzi [72, 85] developed the weakly compressible theory for spherical bubbles. Further, Wang & Blake [103, 104] developed this theory for non-spherical bubbles using the method of matched asymptotic expansions. In the weakly compressible theory, the flow to second order in the outer region far away from the bubble satisfies the wave equation, and that is acquired analytically. The flow to second order in the inner region near the bubble satisfies Laplace's equation and thus is modelled by using the BIM.

Viscous effects

The viscous effects of microbubble dynamics, may not be negligible as the Reynolds number associated may not be large. There are plenty of important medical applications of this phenomenon, such as extracorporeal shock wave lithotripsy [1, 47, 64, 60], oncology, cardiology [8] and tissue ablating [8, 6, 7]. Taking viscous effects into consideration is vital because the Reynolds number R_e for the microbubble dynamics is relatively small. The Reynolds number Re is denoted as $Re = \left(R_m \sqrt{\frac{\Delta p}{\rho}} \right) \Big/ \upsilon$, where Δp is the pressure difference of ambient pressure at infinity and vapour pressure, R_m is the maximum bubble radius, ρ is the density and ν viscosity of the liquid. We can estimate the Reynolds number by given the following parameters for water: Δp = 100 kPa, σ = 0.07 N/m, $\nu = 10^{-3}$ Pa s and $\rho = 1000$ kg/m^{-3}. For $R_m \geq 10$ μm, we have $Re \geq 10$. An irrotational flow is in the bulk liquid domain but also a thin vorticity layer at the bubble surface for microbubble dynamics.

The viscous bubble dynamics were modelled by using the Navier-Stokes equation with the finite element method or finite volume method [23, 27, 28]. Out of the demand of computation,

the domain approaches are normally used for one cycle oscillation.

When a bubble is spherical, the viscous effect only enters the analysis through the normal stress on the bubble surface but no effect in the fluid domain, except viscous dissipation. This can be physically understood as extra work required to against the normal viscous force on the bubble surface during the expansion of the bubble [25, 84].

The model of bubble dynamics with the viscous effect will formulate based on the viscous potential flow theory following [29, 24, 30]. Based on the above considerations, a bubble is approximately keeping spherical at the most time during its lifetime because of the surface tension. Comparing with the whole lifetime, there will be a quite short time when it may become non-spherical at the end of the collapse, and at that time, the viscous effects are not dominant during this period [22].

1.3 Current works

This thesis is concerned with microbubble dynamics in a viscous compressible liquid near a rigid boundary. The compressible effects are modelled by using the weakly compressible theory of Wang & Blake [103, 104], since the Mach number is small. The viscous effects are approximated using the viscous potential flow theory of Joseph & Wang [29], because the flow field is characterised as being an irrotational flow in the bulk volume but with a thin viscous boundary layer at the bubble surface. Consequently, the phenomenon is modelled by using the boundary integral method, in which the compressible and viscous effects are

incorporated into the model through including corresponding additional terms in the far field condition and the dynamic boundary condition at the bubble surface, respectively.

The structure of the thesis is organised as follows. The modelling of the BIM for incompressible potential flow is introduced in details in Chapter 2. In Chapter 3, a bubble initiated near a rigid boundary is modelled by using the weakly compressible theory coupled with the BIM. The wall effects are modelled using the method of the image. The numerical instabilities caused by the near contact of the bubble surface with the boundary are handled by removing a thin layer of water between them and joining the bubble surface with its image to the boundary. Our computations correlate well with experiments for both the first- and second-cycle of oscillation. Some mechanisms of cavitation damage are discussed.

In Chapter 4 we study microbubble dynamics using the viscous potential flow theory coupled with the BIM, where the viscous effects are approximated using the viscous correction pressure. This model agrees well with the Keller Miksis equation for spherical bubble damping in an infinite fluid with the viscous effects and the experiments for bubble dynamics near a rigid wall [86].

In Chapter 5, we model microbubble dynamics in a compressible viscous liquid near a rigid boundary using the viscous potential flow theory and the weak compressible theory. The numerical results are shown in good agreement with the Keller-Miksis equation, experiments and computations based on the Navier-Stokes equations. The bubble oscillation, topological transform, jet development and penetration through the bubble and the energy of the bubble system are simulated and analysed regarding the compressible and viscous effects.

In Chapter 6, we study microbubble dynamics subject to an ultrasound acoustic wave, using the model developed in Chapter 5. This phenomenon has important applications in sonochemistry, ultrasound cleaning and bioscience. The viscous compressible BIM is shown in good agreement with the Keller-Miksis equation for spherical bubble dynamics subject to an acoustic wave. The compressible viscous BIM is also shown in good agreement with the experiments for dynamics of non-spherical bubble subject to ultrasound.

Chapter 2

BOUNDARY INTEGRAL METHOD FOR BUBBLE DYNAMICS

Bubble dynamics have been successfully modelled for decades by using the incompressible potential flow theory coupled with the boundary integral method. The boundary integral method described in the research of Black, Taib and Doherty [12, 13, 43] who took a single axisymmetric cavitation bubble close to free surface and a rigid wall into consideration, respectively. Bubble dynamics near a rigid boundary [48, 58, 71, 111, 112, 117] or a free surface [13, 81, 118] were simulated by the axisymmetric BIM. The viscous effects and compressible effects were neglected by the authors because the large Reynolds number and small Mach number associated with bubble dynamics.

Green's formula has laid the foundation for the Boundary integral method which makes us reformulate the potential flow problem by using the Fredholm integral equation. The potential and its normal derivative on the boundary of the bubble surface occur in the equation. By using this formulation, the dimension of this problem is reduced by one. By integrating through the polar angle, two-dimensional integrals can be lowered to one-dimensional regarding axisymmetric potential problems. Complete elliptic integrals were involved in Green's formula.

In this chapter, the boundary integral method is described for axisymmetrical bubble dynamics, which will be used in the subsequent chapters.

2.1 Boundary integral equation

In an axisymmetric configuration, we consider bubble dynamics near a free surface. Because of the Reynolds, the number associated is usually large, the water flow induced is assumed inviscid. The velocity potential φ satisfies Laplace's equation

$$\nabla^2\varphi = 0. \tag{2.1.1}$$

Using the second Green identity, the velocity potential thus satisfies the boundary integral equation as follows

$$c(\boldsymbol{r},t)\varphi(\boldsymbol{r},t) = \int_S \left(\frac{\partial\varphi(\boldsymbol{q},t)}{\partial n} G(\boldsymbol{r},\boldsymbol{q}) - \varphi(\boldsymbol{q},t)\frac{\partial G(\boldsymbol{r},\boldsymbol{q})}{\partial n} \right) dS(\boldsymbol{q}), \tag{2.1.2}$$

where $\boldsymbol{r}$ is the field point, $\boldsymbol{q}$ is the source point, and $\boldsymbol{n}$ is the unit outward normal of the boundary surface S of the flow field. The Green function is $G(\boldsymbol{r},\boldsymbol{q}) = 1/|\boldsymbol{r}-\boldsymbol{q}|$. $c(\boldsymbol{r}, t)$ is the solid angle

$$c(\boldsymbol{r},t) = \begin{cases} 2\pi & \text{if } \boldsymbol{r} \text{ is at the bubble surface} \\ 4\pi & \text{if } \boldsymbol{r} \text{ is in the flow field} \end{cases}. \tag{2.1.3}$$

The kinematic boundary conditions on the bubble surface S requires a liquid particle on the bubble surface remains on the bubble surface, i.e.

$$\frac{D\boldsymbol{r}}{Dt} = \nabla\varphi \quad \text{on } S, \tag{2.1.4a}$$

the dynamic boundary condition on the bubble surface S is

$$\frac{D\varphi}{Dt} = \frac{1}{2}|\nabla\varphi|^2 - \frac{p-p_\infty}{\rho} - gz \quad \text{on } S, \tag{2.1.4b}$$

which is the balance of the normal stress on the bubble surface. Here p_∞ is the ambient

pressure and g is the gravity acceleration. The coordinate system is set with the z-axis opposite to the gravity direction.

The position vector $\boldsymbol{r}$ and $\boldsymbol{q}$ are the on the boundary of the fluid domain Ω which can be defined as

$$\boldsymbol{r} = (r_0, 0, z_0), \quad \boldsymbol{q} = (r, \theta, z), \tag{2.1.5}$$

where (r, θ, z) is the cylindrical coordinates. By choosing **r** on the surface if, we know either φ or $\partial\varphi/\partial n$ on the bubble surface the other can be found by equation (2.1.2). Once we know both φ and $\partial\varphi/\partial n$ on the surface by using equation (2.1.2) can calculate φ at any point in the fluid domain.

By using cylindrical polar coordinates, the Green function $G(\boldsymbol{r}, \boldsymbol{q})$ can be expressed as follows:

$$\begin{aligned} G(\boldsymbol{r},\boldsymbol{q}) &= \frac{1}{|\boldsymbol{r}-\boldsymbol{q}|} = \frac{1}{\left[(r_0 - r\cos\theta)^2 + (r\sin\theta)^2 + (z_0 - z)^2\right]^{\frac{1}{2}}} \\ &= \frac{1}{\left[r_0^2 - 2r_0 r\left(1 - 2\cos^2\frac{\theta}{2}\right) + r^2 + z_0^2 - 2z_0 z + z^2\right]^{\frac{1}{2}}} \\ &= \frac{1}{\left[(z - z_0)^2 + (r + r_0)^2 - 4r_0 r\cos^2\frac{\theta}{2}\right]} \end{aligned} . \tag{2.1.6}$$

As it is an axisymmetric problem, we can express the surface using the two parameters (θ, ζ), where ζ is the parameter to express the intersection of the bubble surface with the plane $\theta = \theta$. The surface element dS thus can be expressed as follows

$$dS = \left|\frac{d\boldsymbol{q}}{d\zeta}\right| \times \left|\frac{d\boldsymbol{q}}{d\theta}\right| d\zeta d\theta .$$

The partial different vector $\boldsymbol{q}$ with respect to ζ and θ can be obtained

$$\frac{d\boldsymbol{q}(\zeta,\theta)}{d\zeta} = \left(\frac{dr(\zeta)}{d\zeta}\cos\theta, \frac{dr(\zeta)}{d\zeta}\sin\theta, \frac{dz(\zeta)}{d\zeta} \right),$$

$$\frac{d\boldsymbol{q}(\zeta,\theta)}{d\zeta} = \left(-r(\zeta)\sin\theta, r(\zeta)\cos\theta, 0\right).$$

The cross product is calculated as

$$\begin{aligned}\left|\frac{d\boldsymbol{q}}{d\zeta}\times\frac{d\boldsymbol{q}}{d\theta}\right| &= \left(-r(\zeta)\frac{dz(\zeta)}{d\zeta}\cos\theta\right)\boldsymbol{i} + \left(r(\zeta)\frac{dz(\zeta)}{d\zeta}\sin\theta\right)\boldsymbol{j} \\ &\quad \left(r(\zeta)\frac{dr(\zeta)}{d\zeta}\cos^2\theta + r(\zeta)\frac{dr(\zeta)}{d\zeta}\sin^2\theta\right)\boldsymbol{k} \\ &= \left(-r(\zeta)\frac{dz(\zeta)}{d\zeta}\cos\theta\right)\boldsymbol{i} + \left(r(\zeta)\frac{dz(\zeta)}{d\zeta}\sin\theta\right)\boldsymbol{j} \\ &\quad + \left(r(\zeta)\frac{dr(\zeta)}{d\zeta}\right)\boldsymbol{k}\end{aligned}.$$

hence the first surface integral in (2.1.2) can be calculated as follows

$$\begin{aligned}\int_S \frac{1}{|\boldsymbol{r}-\boldsymbol{q}|}dS &= \int_0^1 \frac{1}{|\boldsymbol{r}-\boldsymbol{q}|}\left[\left(\frac{dz}{d\zeta}\right)^2 + \left(\frac{dr}{d\zeta}\right)^2\right]^{\frac{1}{2}} r(\zeta)\,d\zeta \\ &\quad \int_0^{2\pi} \frac{d\theta}{\left[\left(z_0 - z(\zeta)\right)^2 + \left(r_0 + r(\zeta)\right)^2 - 4r_0 r(\zeta)\cos^2\frac{\theta}{2}\right]^{\frac{1}{2}}} \\ &= \int_0^1 \left[\left(\frac{dz}{d\zeta}\right)^2 + \left(\frac{dr}{d\zeta}\right)^2\right]^{\frac{1}{2}} \frac{1}{\left(z_0 - z(\zeta)\right)^2 + \left(r_0 + r(\zeta)\right)^2} r(\zeta)\,d\zeta \\ &\quad \int_0^{2\pi} \frac{d\theta}{\left[\dfrac{\left(z_0 - z(\zeta)\right)^2 + \left(r_0 + r(\zeta)\right)^2 - 4r_0 r(\zeta)\cos^2\frac{\theta}{2}}{\left(z_0 - z(\zeta)\right)^2 + \left(r_0 + r(\zeta)\right)^2}\right]^{\frac{1}{2}}}\end{aligned}$$

$$= \int_0^1 \frac{\left[\left(\frac{dz}{d\zeta}\right)^2 + \left(\frac{dr}{d\zeta}\right)^2\right]^{\frac{1}{2}}}{(z_0 - z(\zeta))^2 + (r_0 + r(\zeta))^2} r(\zeta) d\zeta$$

$$\int_0^{2\pi} \frac{d\theta}{\left[1 - \frac{4 r_0 r(\zeta) \cos^2 \frac{\theta}{2}}{(z_0 - z(\zeta))^2 + (r_0 + r(\zeta))^2}\right]^{\frac{1}{2}}} . \qquad (2.1.7)$$

We then define the variable k^2

$$k^2 = \frac{4 r_0 r(\zeta) \cos^2 \frac{\theta}{2}}{(z_0 - z(\zeta))^2 + (r_0 + r(\zeta))^2}, \qquad (2.1.8)$$

the integral in (2.1.7) in terms of θ can be expressed as following by defining $\beta = \frac{\theta}{2}$

$$\int_0^{2\pi} \frac{d\theta}{\left[1 - k^2 \cos^2 \frac{\theta}{2}\right]^{\frac{1}{2}}} = 2\int_0^{\pi} \frac{d\beta}{\left[1 - k^2 \cos^2 \beta\right]^{\frac{1}{2}}} = 4\int_0^{\frac{\pi}{2}} \frac{d\beta}{\left[1 - k^2 \cos^2 \beta\right]^{\frac{1}{2}}} = 4K(k), \qquad (2.1.9)$$

with *K(k)* is the first kind complete elliptic integral. Now the equation (2.1.7) can be written as

$$\int_S \frac{1}{|\boldsymbol{r} - \boldsymbol{q}|} dS = 4\int_0^1 \frac{r(\zeta)\left[\left(\frac{dr}{d\zeta}\right)^2 + \left(\frac{dz}{d\zeta}\right)^2\right]^{\frac{1}{2}}}{\left[\left(r(\zeta) + r_0\right)^2 + \left(z(\zeta) + r_0\right)^2\right]^{\frac{1}{2}}} d\zeta , \qquad (2.1.10)$$

similarly we have

$$\int_S \frac{\partial}{\partial n} \frac{1}{|\boldsymbol{r} - \boldsymbol{q}|} dS = -4\int_0^1 \frac{r(\zeta) d\zeta}{\left[\left(r(\zeta) + r_0\right)^2 + \left(z(\zeta) - z_0\right)^2\right]^{\frac{3}{2}}}$$

$$\left[\frac{dz}{d\zeta}\left(r(\zeta) + r_0\right) - \frac{dr}{d\zeta}\left(z(\zeta) - z_0\right) - \frac{2}{k^2(\zeta)} \frac{dz}{d\zeta} r_0\right] \frac{E(k)}{1 - k^2(\zeta)}$$

$$-4\int_0^1 \frac{r(\zeta)d\zeta}{\left[(r(\zeta)+r_0)^2+(z(\zeta)-z_0)^2\right]^{\frac{3}{2}}}\frac{2}{k^2(\zeta)}\frac{dz}{d\zeta}r_0K(k), \tag{2.1.11}$$

with *E(k)* and $\frac{E(k)}{1-k^2}$ are the second kind complete elliptic integral and the third kind complete elliptic integral, respectively. Hastings (1995) provided approximations for the first and second kind complete elliptic integral as follow

$$K(k)=P\left(1-k^2(\zeta)\right)-Q\left(1-k^2(\zeta)\right)\ln\left(1-k^2(\zeta)\right), \tag{2.1.12}$$

$$E(k)=R\left(1-k^2(\zeta)\right)-S\left(1-k^2(\zeta)\right)\ln\left(1-k^2(\zeta)\right), \tag{2.1.13}$$

where the function $P(1-k^2(\zeta))$, $Q(1-k^2(\zeta))$, $R(1-k^2(\zeta))$ and $S(1-k^2(\zeta))$ are tabulated polynomials.

2.2 Numerical procedure

2.2.1 Linear elements

To proceed with the computation, we need to choose a representation for the surface, and also for the potential and its normal derivative on the surface. To some extent, these choices can be independent, but as the movement of the surface is computed using the potential and its normal derivative, the two should be considered together. In the description which follows, a plane section through the axis of symmetry of the surface is taken, rotational symmetry about the axis is understood, the potential and its normal derivative will be call functions.

ϕ_i and $\chi_i=\frac{\partial\varphi_i}{\partial n}$ are assumed to be single-valued at the endpoints of the linear segments which approximate the surface. If the segment is parameterised by ζ in the range (0, 1) we can define

$$\begin{cases} M_1(\zeta)=1-\zeta, \\ M_2(\zeta)=\zeta, \end{cases} \tag{2.2.1.1}$$

and use the isoparametric approximations for both the surface and the functions. On a

segment S_i we have,

$$\begin{cases} z(\zeta) = z_{i-1}(1-\zeta) + z_i\zeta \\ r(\zeta) = r_{i-1}(1-\zeta) + r_i\zeta \\ \varphi(\zeta) = \varphi_{i-1}(1-\zeta) + \varphi_i\zeta \\ \chi(\zeta) = \chi_{i-1}(1-\zeta) + \chi_i\zeta \end{cases}. \tag{2.2.1.2}$$

The collocation points are chosen at the ends of each segment, yielding N+1 equations in the $N+1$ unknowns. The integrals on each segment can be written N+1

$$\int_{S_i} \frac{\partial\phi}{\partial n} \frac{1}{|p_j - q_i|} dS = b_{1ij} \frac{\partial\phi_{i-1}}{\partial n} + b_{2ij} \frac{\partial\phi_i}{\partial n}, \tag{2.2.1.3}$$

with

$$b_{1ij} = S_i \int_0^1 (1-\zeta) d\zeta \int_0^{2\pi} \frac{d\theta}{|p_j - q(\zeta,\theta)|},$$

$$b_{2ij} = S_i \int_0^1 \zeta d\zeta \int_0^{2\pi} \frac{d\theta}{|p_j - q(\zeta,\theta)|},$$

and

$$\int_{S_i} \phi \frac{\partial}{\partial n}\left(\frac{1}{|p_j - q_i|}\right) dS = a_{1ij}\phi_{i-1} + a_{2ij}\phi_i, \tag{2.2.1.4}$$

with

$$a_{1ij} = S_i \int_0^1 (1-\zeta) d\zeta \int_0^{2\pi} \frac{\partial}{\partial n}\left(\frac{1}{|p_j - q(\zeta,\theta)|}\right) d\theta,$$

$$a_{2ij} = S_i \int_0^1 \zeta d\zeta \int_0^{2\pi} \frac{\partial}{\partial n}\left(\frac{1}{|p_j - q(\zeta,\theta)|}\right) d\theta.$$

2.2.2 Calculation of the influence matrix

To evaluate the elements of the matrices is carried out numerically. Guass Legendre quadrature is usually sufficient, except the collocation point is p_i one of the endpoints. By

subtracting the logarithmic term to eliminate the singularity the singular integrals are performed. And then use a quadrature scheme collaborating the logarithm to fulfil the integration.

Since we have

$$k(\zeta)^2 = \frac{4r_0 r(\zeta)\cos^2\frac{\theta}{2}}{(z_0 - z(\zeta))^2 + (r_0 + r(\zeta))^2}, \tag{2.2.2.1}$$

and then define *y* as

$$y = 1 - k(\zeta)^2 = \frac{(z_0 - z(\zeta))^2 + (r_0 - r(\zeta))^2}{(z_0 - z(\zeta))^2 + (r_0 + r(\zeta))^2}. \tag{2.2.2.2}$$

For example if the singularity happens when $(r_0, z_0) = (r(1), z(1))$, we can use the Taylor expansions around it as following

$$r(\zeta) = r_0 + (\zeta - 1)\frac{dr}{d\zeta} + \frac{1}{2}(\zeta - 1)^2 \frac{d^2 r}{d\zeta^2} + \cdots$$

$$z(\zeta) = z_0 + (\zeta - 1)\frac{dz}{d\zeta} + \frac{1}{2}(\zeta - 1)^2 \frac{d^2 z}{d\zeta^2} + \cdots.$$

Now we can estimate *y* as

$$y = 1 - k(\zeta)^2 \approx \frac{(\zeta - 1)^2}{4r_0^2}\left[\left(\frac{dr}{d\zeta}\right)^2 + \left(\frac{dz}{d\zeta}\right)^2\right], \tag{2.2.2.3}$$

so that essential *K(ζ)* behaves like

$$K(\zeta) \approx P(x) - Q(x)\ln\left(A(\zeta - 1)^2\right). \tag{2.2.2.4}$$

This information is sufficient to allow us to deal with the singularity.

Singularity at *ζ=0*

This singularity occurs when $\boldsymbol{r}$ is the point $(r_0, z_0) = (r(0), z(0))$. If we define the equation $E(\zeta)$ and $F(\zeta)$ as follows:

$$F(\zeta) = \left[\left(\frac{dz}{d\zeta} \right)^2 + \left(\frac{dr}{d\zeta} \right)^2 \right]^{\frac{1}{2}}, \tag{2.2.2.5}$$

$$G(\zeta) = \left[(z_0 - z(\zeta))^2 + (r_0 + r(\zeta))^2 \right]^{\frac{1}{2}}. \tag{2.2.2.6}$$

then equation (2.1.10) and (2.1.11) can be rewrite as

$$\int_S \frac{1}{|\boldsymbol{r} - \boldsymbol{q}|} dS = 4 \int_0^1 \frac{r(\zeta) F(\zeta) K(k)}{G(\zeta)} d\zeta \tag{2.2.2.7}$$

and

$$\begin{aligned} \int_S \frac{\partial}{\partial n} \left(\frac{1}{|\boldsymbol{r} - \boldsymbol{q}|} \right) dS = & -4 \int_0^1 \frac{r(\zeta)}{G^3(\zeta)} \frac{E(k)}{1 - k^2(\zeta)} \\ & \left[\frac{dz}{d\zeta} (r(\zeta) + r_0) - \frac{dr}{d\zeta} (z(\zeta) - z_0) - \frac{2}{k^2(\zeta)} \frac{dz}{d\zeta} r_0 \right] d\zeta \\ & - 8 \int_0^1 \frac{r(\zeta)}{G^3(\zeta)} \frac{1}{k^2(\zeta)} \frac{dz}{d\zeta} r_0 K(k) d \end{aligned}. \tag{2.2.2.8}$$

By expressing ln(x) as two added parts

$$\ln(x) = \ln\left(\frac{x}{\zeta^2} \right) + 2\ln(\zeta) \tag{2.2.2.9}$$

with equations (2.1.12) and (2.1.13) we can express equations (2.2.2.7) (2.2.2.8) as

$$\int_S \frac{1}{|\boldsymbol{r}-\boldsymbol{q}|}dS = 4\int_0^1 \frac{r(\zeta)F(\zeta)K(K)}{G(\zeta)}d\zeta$$
$$= 4\int_0^1 \frac{r(\zeta)F(\zeta)\left[P(y)-Q(y)\ln(y)\right]}{G(\zeta)}d\zeta$$
$$= 4\int_0^1 \frac{r(\zeta)F(\zeta)P\left(y(\zeta)\right)}{G(\zeta)}d\zeta \qquad (2.2.2.10)$$
$$-4\int_0^1 \frac{r(\zeta)F(\zeta)Q\left(y(\zeta)\right)\ln\left(\frac{y(\zeta)}{\zeta^2}\right)}{G(\zeta)}d\zeta$$
$$-8\int_0^1 \frac{r(\zeta)F(\zeta)Q\left(y(\zeta)\right)\ln\zeta}{G(\zeta)}d\zeta$$

and

$$\int_S \frac{\partial}{\partial n}\frac{1}{|\boldsymbol{r}-\boldsymbol{q}|}dS = -4\int_0^1 \frac{r(\zeta)}{G^3(\zeta)}\frac{R(y)-S(y)\ln(y)}{1-k^2(\zeta)}$$
$$\left[\frac{dz}{d\zeta}\left(r(\zeta)+r_0\right)-\frac{dr}{d\zeta}\left(z(\zeta)-z_0\right)-\frac{2}{k^2(\zeta)}\frac{dz}{d\zeta}r_0\right]d\zeta$$
$$-8\int_0^1 \frac{r(\zeta)}{G^3(\zeta)}\frac{1}{k^2(\zeta)}\frac{dz}{d\zeta}r_0\left[P(y)-Q(y)\ln(y)\right]d\zeta$$
$$= -4\int_0^1 \frac{r(\zeta)}{G^3(\zeta)}\frac{R(y)-S(y)\ln\left(\frac{y}{\zeta^2}\right)}{1-k^2(\zeta)}$$
$$\left[\frac{dz}{d\zeta}\left(r(\zeta)+r_0\right)-\frac{dr}{d\zeta}\left(z(\zeta)-z_0\right)-\frac{2}{k^2(\zeta)}\frac{dz}{d\zeta}r_0\right]d\zeta$$
$$-8\int_0^1 \frac{r(\zeta)}{G^3(\zeta)}\frac{1}{k^2(\zeta)}\frac{dz}{d\zeta}r_0\left[P(y)-Q(y)\ln\left(\frac{y}{\zeta^2}\right)\right]d\zeta$$
$$= -4\int_0^1 \frac{r(\zeta)}{G^3(\zeta)}\frac{R(y)-S(y)\ln\left(\frac{y}{\zeta^2}\right)}{1-k^2(\zeta)}$$
$$\left[\frac{dz}{d\zeta}\left(r(\zeta)+r_0\right)-\frac{dr}{d\zeta}\left(z(\zeta)-z_0\right)-\frac{2}{k^2(\zeta)}\frac{dz}{d\zeta}r_0\right]d\zeta$$
$$-8\int_0^1 \frac{r(\zeta)}{G^3(\zeta)}\frac{1}{k^2(\zeta)}\frac{dz}{d\zeta}r_0\left[P(y)-Q(y)\ln\left(\frac{y}{\zeta^2}\right)\right]d\zeta$$

$$-8\int_0^1 \frac{r(\zeta)}{G^3(\zeta)}\frac{S(y)\ln(\zeta)}{1-k^2(\zeta)}$$
$$\left[\frac{dz}{d\zeta}(r(\zeta)+r_0)-\frac{dr}{d\zeta}(z(\zeta)-z_0)-\frac{2}{k^2(\zeta)}\frac{dz}{d\zeta}r_0\right]d\zeta\ . \qquad (2.2.2.11)$$
$$-16\int_0^1 \frac{r(\zeta)}{G^3(\zeta)}\frac{1}{k^2(\zeta)}\frac{dz}{d\zeta}r_0 Q(y)\ln(\zeta)d\zeta$$

Singularity at ζ=1

For this case, the point ***r*** is given as $(r_0, z_0)=(r(1), z(1))$. By setting

$$\ln(y)=\ln\left(\frac{y}{(1-\zeta)^2}\right)+2\ln(1-\zeta), \qquad (2.2.2.12)$$

we can express

$$\int_S \frac{1}{|\boldsymbol{r}-\boldsymbol{q}|}dS = 4\int_0^1 \frac{r(\zeta)F(\zeta)P(y(\zeta))}{G(\zeta)}d\eta$$
$$-4\int_0^1 \frac{r(\zeta)F(\zeta)Q(y(\zeta))\ln\left(\frac{y(\zeta)}{(1-\zeta)^2}\right)}{G(\zeta)}d\eta$$
$$-8\int_0^1 \frac{r(1-\eta)F(1-\eta)Q(y(1-\eta))\ln\eta}{G(1-\eta)}d\eta \qquad (2.2.2.13)$$

and

$$\int_S \frac{\partial}{\partial n}\frac{1}{|\boldsymbol{r}-\boldsymbol{q}|}dS = -4\int_0^1 \frac{r(\zeta)}{G^3(\zeta)}\frac{R(y)-S(y)\ln\left(\frac{y}{(1-\zeta)^2}\right)}{1-k^2(\zeta)}$$
$$\left[\frac{dz}{d\zeta}(r(\zeta)+r_0)-\frac{dr}{d\zeta}(z(\zeta)-z_0)-\frac{2}{k^2(\zeta)}\frac{dz}{d\zeta}r_0\right]d\zeta$$
$$-8\int_0^1 \frac{r(\zeta)}{G^3(\zeta)}\frac{1}{k^2(\zeta)}\frac{dz}{d\zeta}r_0\left[P(y)-Q(y)\ln\left(\frac{y}{(1-\zeta)^2}\right)\right]d\zeta$$

$$-8\int_0^1 \frac{r(1+\eta)}{G^3(1+\eta)}\frac{S(1+\eta)\ln\eta}{1-k^2(1+\eta)}$$
$$\left[\begin{array}{l}\frac{dz}{d\zeta}\left(r(1+\eta)+r_0\right)-\frac{dr}{d\zeta}\left(z(1+\eta)-z_0\right)\\ -\frac{2}{k^2(1+\eta)}\frac{dz}{d\zeta}r_0\end{array}\right]d\eta$$
$$-16\int_0^1 \frac{r(1+\eta)}{G^3(1+\eta)}\frac{1}{k^2(1+\eta)}\frac{dz}{d\zeta}r_0 Q\left(y(1+\eta)\right)\ln\eta d\eta\,. \quad (2.2.2.14)$$

In (2.2.2.10), (2.2.2.11), (2.2.2.13) and (2.2.2.14) the first integrals involve no singularity, therefore can be integrated by applying the standard Gauss Legendre quadrature. The remaining integral include an explicit singularity of log type which can be integrated by applying the quadrature scheme tabulated by Stroud and Secrest [122] for the integral:

$$\int_0^1 f(x)\ln\left(\frac{1}{x}\right)dx\,. \quad (2.2.5.18)$$

Chapter 3

BUBBLE DYNAMICS IN A COMPRESSIBLE LIDUID

In this chapter, a bubble initiated near a rigid boundary is modelled using the weakly compressible theory coupled with the boundary integral method. The wall effects are modelled using the method of the image. The numerical instabilities caused by the near contact of the bubble surface with the boundary are handled by removing a thin layer of water between them and joining the bubble surface with its image to the boundary. Our computations correlate well with experiments for both the first- and second-cycles of oscillation. Some mechanisms of cavitation damage are discussed.

3.1 Weakly compressible theory

Consider the dynamics of a gas bubble near a rigid flat boundary in an inviscid and compressible liquid. A Cartesian-coordinate system is set as illustrated in figure 3.1. The *x*-axis is on the rigid boundary, and the *z*-axis is along the axis of symmetry for the configuration.

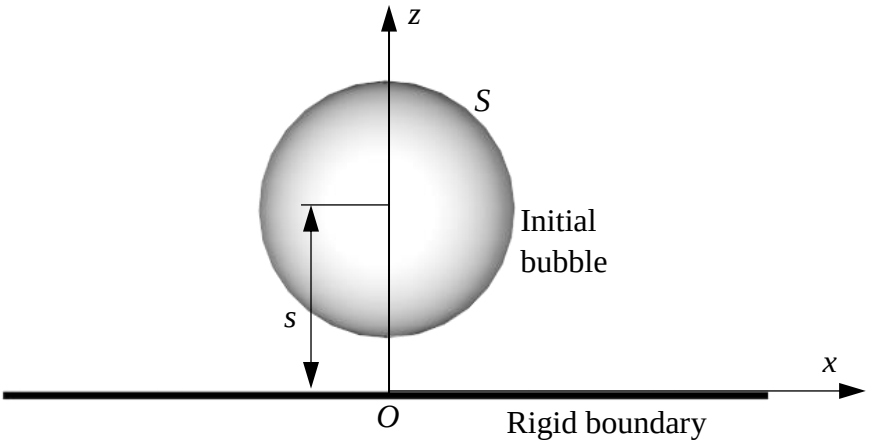

Figure 3.1. Sketch of a bubble motion near a rigid boundary and the coordinates used. The standoff distance between the centre of the initial bubble and the rigid boundary is *s*, and *S* is the bubble surface.

The liquid flow is described by the continuity equation

$$\frac{\partial \rho}{\partial t} + \nabla \cdot (\rho \mathbf{u}) = 0, \tag{3.1.1}$$

and the Euler equation

$$\frac{\partial \boldsymbol{u}}{\partial t} + \boldsymbol{u} \cdot \nabla \boldsymbol{u} = -\frac{1}{\rho} \nabla p. \tag{3.1.2}$$

In bubble dynamics liquid compressibility usually important when the high-speed motion occurred. We can assume that the thermal effects in the fluid are unimportant. The speed of sound *c* and the enthalpy *h* of the fluid are as follows:

$$c^2 = \frac{dp}{d\rho}, \qquad h = \int_{p_\infty}^{p} \frac{dp}{\rho} \tag{3.1.3, 3.1.4}$$

p_∞ is the ambient pressure in the undisturbed fluid.

As the flow is irrotational, the flow velocity can be expressed regarding the velocity potential φ using $\boldsymbol{u} = \nabla\varphi$. Substitute it into equation (3.1.1) we get the conservation of mass regarding the velocity potential as follows:

$$\frac{1}{\rho}\frac{D\rho}{Dt} + \nabla^2\varphi = 0, . \tag{3.1.5}$$

where *D/Dt* is the material derivative.

By integrating (3.1.2) we obtain the Bernoulli equation

$$\frac{\partial\varphi}{\partial t} + \frac{1}{2}|\nabla\varphi|^2 + h = 0. \tag{3.1.6}$$

Using (3.1.3) and (3.1.4), we can express the first term in (3.1.5) as follows:

$$\begin{aligned}\frac{1}{\rho}\frac{D\rho}{Dt} &= \frac{1}{\rho}\left(\frac{\partial\rho}{\partial t} + \nabla\varphi\cdot\nabla\rho\right) = \left(\frac{\partial \ln\rho}{\partial t} + \nabla\varphi\cdot\nabla\ln\rho\right) \\ &= \frac{\partial}{\partial t}\left(\int\frac{1}{\rho}d\rho\right) + \nabla\varphi\cdot\nabla\left(\int\frac{1}{\rho}d\rho\right) = \frac{1}{c^2}\left(\frac{\partial h}{\partial t} + \nabla\varphi\cdot\nabla h\right)\end{aligned}. \tag{3.1.7a}$$

As such the continuity equation (3.1.5) becomes

$$\nabla^2\varphi + \frac{1}{c^2}\left(\frac{\partial h}{\partial t} + \nabla\varphi\cdot\nabla h\right) = 0. \tag{3.1.7b}$$

In order to find the formula to express the speed of sound *c* and the enthalpy *h*, we introduce the Tait model for the relationship between pressure and density as follows:

$$\left(\frac{\rho}{\rho_\infty}\right)^n = \frac{p + B}{p_\infty + B}. \tag{3.1.8}$$

By rearranging the Tait model, the pressure p can be expressed by p_∞, B, ρ_∞ and ρ. We

substitute this expression of p into equation (3.1.3) and rearrange it to get the expression of the speed of sound c as follows:

$$\begin{aligned} c^2 = \frac{dp}{d\rho} &= \frac{d}{d\rho}\left[B + (p_\infty + B)\left(\frac{\rho}{\rho_\infty}\right)^n \right] \\ &= (p_\infty + B) n \left(\frac{\rho}{\rho_\infty}\right)^{n-1} \frac{1}{\rho_\infty} \\ &= \frac{n}{\rho_\infty}(p_\infty + B)\left(\frac{\rho}{\rho_\infty}\right)^{n-1} \\ &= \frac{n}{\rho_\infty}(p_\infty + B)\left(\frac{p+B}{p_\infty + B}\right)\left(\frac{p_\infty + B}{p+B}\right)^{\frac{1}{n}} \\ &= \frac{n}{\rho_\infty}(p_\infty + B)^{\frac{1}{n}}(p+B)^{\frac{n-1}{n}} \end{aligned} \quad . \qquad (3.1.9)$$

By rearranging the Tait model, the pressure ρ can be expressed by p_∞, B, ρ_∞ and p. We substitute this expression of ρ into equation (3.1.3) and rearrange it to get the expression of sound as follows:

$$\begin{aligned} h = \int_{p_\infty}^{p} \frac{dp}{\rho} &= \int_{p_\infty}^{p} \frac{1}{\rho_\infty}\left(\frac{p_\infty + B}{p+B}\right)^{\frac{1}{n}} dp \\ &= \frac{1}{\rho_\infty}\int_{p_\infty}^{p}\left(\frac{p_\infty + B}{p+B}\right)^{\frac{1}{n}} dp = \frac{1}{\rho_\infty}(p_\infty + B)^{\frac{1}{n}}\int_{p_\infty}^{p}\left(\frac{1}{p+B}\right)^{\frac{1}{n}} dp \\ &= \frac{1}{\rho_\infty}(p_\infty + B)^{\frac{1}{n}}\left(\left.\frac{(p+B)^{\frac{-1}{n}+1}}{\frac{-1}{n}+1}\right|_{p_\infty}^{p} \right) \\ &= \frac{n}{\rho_\infty}(p_\infty + B)^{\frac{1}{n}}\left(\left.\frac{(p+B)^{\frac{n-1}{n}}}{n-1}\right|_{p_\infty}^{p} \right) \\ &= \frac{c_\infty^2}{n-1}\left(\left(\frac{p+B}{p_\infty + B}\right)^{\frac{n-1}{n}} - 1 \right) \end{aligned} \quad . \qquad (3.1.10)$$

where c_∞ is the speed of the sound in the undisturbed fluid as. When the pressure of fluid doesn't have a significant difference with p_∞, we can use the Taylor expansion to express $1/\rho$ around p_∞ then integrate with respect to p as follows [85]:

$$\begin{aligned} h &= \int_{p_\infty}^{p} \frac{1}{\rho} dp = \int_{p_\infty}^{p} \left[\frac{1}{\rho_\infty} - \frac{d}{d\rho}\left(\frac{1}{\rho}\right)\frac{d\rho}{dp}\left(p - p_\infty\right) \right] dp \\ &= \frac{p - p_\infty}{\rho_\infty} - \frac{1}{2c_\infty^2}\left(\frac{p - p_\infty}{\rho_\infty}\right)^2 + \cdots \end{aligned}, \tag{3.1.11}$$

similarly we have

$$\frac{1}{c^2} = \frac{1}{c_\infty^2} - (n-1)\frac{p - p_\infty}{c_\infty^4 \rho_\infty} + \cdots. \tag{3.1.12}$$

We choose maximum bubble radius R_m as the reference length, the density of the liquid ρ_∞ in the undisturbed liquid as the reference density. The pressure reference is chosen as $\Delta p = p_\infty - p_v$, where p_v is the partial pressure of vapour of the bubble. The reference velocity is thus obtained as $U = \sqrt{\Delta p / \rho_\infty}$. The reference time is obtained as $T = R_m / U = R_m \sqrt{\rho_\infty / \Delta p}$. The time reference obtained provides the scale of the oscillation period of a bubble. As an example, the collapsing time required for a cavity collapsing from $R = R_m$ to $R = 0$, obtained by Rayleigh [87], is $T_{\text{Rayleigh}} = 0.915 R_m \sqrt{\rho_\infty / \Delta p}$.

We perform non-dimensionalization to the problem using the reference parameters and denote dimensionless quantities by subscripts "*" as follows:

$$\varphi_* = \frac{\varphi}{R_m U}, \quad t_* = \frac{U}{R_m} t, \quad r_* = \frac{r}{R_m}, \tag{3.1.13a, b, c}$$

$$h = U^2 h_*, \quad c = c_\infty c_*, \quad p = \frac{p - p_\infty}{\Delta p}, \tag{3.1.13d, e}$$

where the speed of sound c is normalized by its value in the undisturbed liquid c_∞.

The compressibility of the liquid flow can be measured by the Mach number defined in terms of the reference flow velocity U and the speed of sound c_∞ in the undisturbed liquid as follows:

$$\varepsilon = \frac{U}{c_\infty}. \tag{3.1.14}$$

We assume that the Mach number ε is small, because the speed of sound in water is about 1500 m s^{-1}, whereas the velocity of the bubble jet is slower than 200 m s^{-1} at normal ambient pressure [39, 66, 89, 95-96, 68, 82, 79, 46 and 109].

Expressing the equation (3.1.6, 3.1.7) in dimensionless variables as following:

$$\frac{\partial \varphi_*}{\partial t_*} + \frac{1}{2}\left|\nabla_* \varphi_*\right|^2 + h_* = 0, \tag{3.1.15}$$

$$\nabla_*{}^2 \varphi_* + \frac{\varepsilon^2}{c_*^2}\left(\frac{\partial h_*}{\partial t_*} + \nabla_* \varphi_* \cdot \nabla_* h_*\right) = 0. \tag{3.1.16}$$

By substituting the dimensionless variables into the equation (3.1.9, 3.1.10) we obtain the dimensionless enthalpy and sound speed in the liquid as follows:

$$U^2 h_* = \frac{c_\infty^2 c_*^2 - c_\infty^2}{n-1},$$

$$\varepsilon h_* (n-1) + 1 = c_*^2. \tag{3.1.17}$$

Similarly, we have

$$h_* U^2 = \frac{c_\infty^2}{n-1}\left(\left(\frac{p+B}{p_\infty+B}\right)^{\frac{n-1}{n}} - 1\right), \tag{3.1.18a}$$

$$h_* = \frac{1}{\varepsilon^2}\frac{1}{n-1}\left(\left(\frac{p+B}{p_\infty+B}\right)^{\frac{n-1}{n}} - 1\right). \tag{3.1.18b}$$

By substituting non-dimensionless variables into equations (3.1.11, 3.1.12), we obtain the speed of sound and the enthalpy in the dimensionless form. The steps show details of non-dimensionalization are as following:

$$U^2 h_* = U^2 p_* - \frac{1}{2c_\infty^2}\left(U^2 p_*\right)^2,$$

$$h_* = p_* - \frac{1}{2}\varepsilon^2 p_*^2 + o\left(\varepsilon^2\right), \tag{3.1.19}$$

$$\frac{1}{c^2} = \frac{1}{c_\infty^2} - (n-1)\frac{p-p_\infty}{c_\infty^4 \rho_\infty},$$

$$\frac{1}{c_*^2} = 1-(n-1)\frac{p_\infty p_*}{c_\infty^2 \rho_\infty} = 1-(n-1)\frac{p_* U^2}{c_\infty^2} = 1-(n-1)\varepsilon^2 p_*. \tag{3.1.20}$$

We divide the fluid domain into two asymptotic regions: the inner region near the bubble where $(x, y, z) = O(R_\mathrm{m})$ and the outer region far away from the bubble where $(x, y, z) = O(\lambda)$, with $\lambda = c_\infty R_\mathrm{m}/U$ being the wavelength of acoustic waves.

We define the dimensionless inner region variable as $r_* = (x_*, y_*, z_*) = O(1)$ and the outer

region variable as $\tilde{r} = (\tilde{x}, \tilde{y}, \tilde{z}) = r/c_\infty T = \frac{R_m}{c_\infty T}(x_*, y_*, z_*) = \varepsilon r_*$ where we choose the T as the time scale for a change of order of the bubble radius R_m. The outer expansions are as follows:

$$\varphi_*(r_*, t_*) = \phi(\tilde{r}, t_*) = \phi_0(\tilde{r}, t_*) + \varepsilon\phi_1(\tilde{r}, t_*) + \varepsilon^2\phi_2(\tilde{r}, t_*) + \cdots, \tag{3.1.21}$$

$$p_*(r_*, t_*) = P(\tilde{r}, t_*) = P_0(\tilde{r}, t_*) + \varepsilon P_1(\tilde{r}, t_*) + \varepsilon^2 P_2(\tilde{r}, t_*) + \cdots. \tag{3.1.22}$$

By using the outer variable, equation (3.1.15) and (3.1.16) become

$$\frac{\partial \varphi_*}{\partial t_*} + \frac{1}{2}\varepsilon^2 \left|\tilde{\nabla}\varphi_*\right|^2 + p_* = 0, \tag{3.1.23}$$

$$\tilde{\nabla}^2 \varphi_* + \frac{\partial p_*}{\partial t_*} + \varepsilon^2 \left(\nabla_* \varphi_* \cdot \nabla_* h_* - (\mathrm{n}\text{-}1) p_* \frac{\partial p_*}{\partial t_*} \right) + O(\varepsilon^4) = 0. \tag{3.1.24}$$

Substituting the outer expansion into above equations, we obtain:

$$\tilde{\nabla}^2 \phi_* - \frac{\partial^2 \phi_i}{\partial t_*^2} = 0, \quad \text{for} \quad i = 0,1. \tag{3.1.25}$$

We obtain the first order outer solution by using the far field condition. The general solution for ϕ_1 is the d'Alembert solution. We can obtain the outer solution for the first and second as follows:

$$\phi_0 = 0, \qquad \phi_1 = \frac{F_1(t_* - \tilde{r})}{\tilde{r}}, \tag{3.1.26}$$

where F_1 needs to be decided by matching between the inner and outer solutions. The inner limits of the second order outer expansion are obtained by using the Taylor series expansion as follows:

$$(\phi_1) = \frac{F_1(t_* - \tilde{r})}{\tilde{r}} = \frac{F_1(t_* - \varepsilon r_*)}{\varepsilon r_*} = \frac{F_1(t_*)}{\varepsilon r_*} - \dot{F}_1(t_*) + O(\varepsilon).$$

Hence the inner limit of the outer expansion for the first two orders can be found as flowing:

$$(\phi)^i = \frac{F_1(t_*)}{r_*} - \varepsilon \dot{F}_1(t_*) + O(\varepsilon^2). \tag{3.1.27}$$

We define the inner expansion in terms of the inner variable as the follows:

$$\varphi_*(r_*, t_*) = \varphi_0(r_*, t_*) + \varepsilon\varphi_1(r_*, t_*) + \varepsilon^2\varphi_2(r_*, t_*)\cdots, \tag{3.1.28}$$

$$p_*(r_*, t_*) = p_0(r_*, t_*) + \varepsilon p_1(r_*, t_*) + \varepsilon^2 p_2(r_*, t_*)\cdots. \tag{3.1.29}$$

By substituting the inner expansions into equations (3.1.15) and (3.1.16), we find the equations for first three terms in inner expansions as following:

$$\nabla_*^2\varphi_0 = 0, \tag{3.1.30a}$$

$$\nabla_*^2\varphi_1 = 0, \tag{3.1.30b}$$

$$\nabla_*^2\varphi_2 = -\left(\frac{\partial p_0}{\partial t_*} + \nabla_*\varphi_0 \cdot \nabla_* p_0\right), \tag{3.1.30c}$$

$$\frac{\partial\varphi_0}{\partial t_*} + \frac{1}{2}\left|\nabla_*\varphi_0\right|^2 + p_0 = 0, \tag{3.1.30d}$$

$$\frac{\partial\varphi_1}{\partial t_*} + \nabla_*\varphi_0 \cdot \nabla_*\varphi_1 + p_1 = 0, \tag{3.1.30e}$$

$$\frac{\partial\varphi_2}{\partial t_*} + \nabla_*\varphi_0 \cdot \nabla_*\varphi_2 + p_2 = -\frac{1}{2}\left|\nabla_*\varphi_1\right|^2. \tag{3.1.30f}$$

The problem can be solved by finding the solutions for φ_0, φ_1 and φ_2 The solutions for the order $O(1)$ and $O(\varepsilon)$ of the potential satisfy Laplace's equation. The third order solution $O(\varepsilon^2)$ for potential satisfies the Poisson equation. Since the first two order solutions satisfy Laplace's equations, we can give the general solution as follows:

$$\phi_i(\boldsymbol{r}_*,t_*) = f_i(t_*) + \frac{1}{4\pi}\int_S \frac{\partial\phi(\boldsymbol{q},t_*)}{\partial n} G(r_*,\boldsymbol{q}) - \phi(\boldsymbol{q},t_*)\frac{\partial G(\boldsymbol{r}_*,\boldsymbol{q})}{\partial n} dS(\boldsymbol{q}),$$

for i = 0, 1 (3.1.31)

where we define S as the bubble surface, $\boldsymbol{n}$ is the normal unit vector on bubble surface, $\boldsymbol{q}$ is the integral variable on the bubble surface, and the Green's function is given as follows:

$$G(r_*,\boldsymbol{q}) = \frac{1}{|r_* - \boldsymbol{q}|}. \quad (3.1.32a)$$

When the bubble is near a flat rigid boundary, the Green function is given as follows:

$$G(r_*,\boldsymbol{q}) = \frac{1}{|r_* - \boldsymbol{q}|} + \frac{1}{|r_* - \boldsymbol{q}_{image}|}, \quad (3.1.32b)$$

where $\boldsymbol{q}_{image}$ is the reflection point of $\boldsymbol{q}$ to the rigid wall.

By using the outer variable and the Taylor expansion we can obtain the following estimations:

$$G(r_*,\mathbf{q}) = \frac{1}{|r_* - \mathbf{q}|} + \frac{1}{|r_* - \mathbf{q}_{image}|} = \frac{1}{|\tilde{\mathbf{r}}/\varepsilon - \mathbf{q}|} + \frac{1}{|\tilde{\mathbf{r}}/\varepsilon - \mathbf{q}_{image}|} = 2\left(\frac{\varepsilon}{\tilde{r}} + \varepsilon^2\frac{\tilde{\mathbf{r}}\cdot\mathbf{q}}{\tilde{r}^3}\right) + \cdots$$
,(3.1.33a)

$$\nabla_q G(r_*,\mathbf{q}) = \frac{1}{|r_* - \mathbf{q}|^3} + \frac{1}{|r_* - \mathbf{q}_{image}|^3} = 2\frac{\varepsilon^2\tilde{\mathbf{r}} - \varepsilon^3\mathbf{q}}{|\tilde{\mathbf{r}} - \varepsilon\mathbf{q}|^3} = 2\left(\varepsilon^2\frac{\tilde{\mathbf{r}}}{\tilde{r}^3}\right) + \cdots \quad . \quad (3.1.33b)$$

Substituting (3.1.33) into (3.1.31) we find the first two order outer limits of the inner solutions as following:

$$\begin{aligned}(\phi_i)^o &= f_i(t_*) + \frac{1}{2\pi}\int_S \left(\frac{\partial\phi_i(\boldsymbol{q})}{\partial n}\left(\frac{\varepsilon}{\tilde{r}} + \varepsilon^2\frac{\tilde{r}\cdot\boldsymbol{q}}{\tilde{r}^3}\right) - \phi_i(\boldsymbol{q})\left(\varepsilon^2\frac{\tilde{r}}{\tilde{r}^3}\right)\right) dS(\boldsymbol{q}) + O(\varepsilon^3) \\ &= f_i(t_*) + \varepsilon\frac{1}{2\pi}\frac{m_i(t_*)}{\tilde{r}} + O(\varepsilon^2).\end{aligned} \quad , (3.1.34)$$

$V_i(t_*)$ are obtained as follows:

$$V_i(t_*) = \int_S \frac{\partial \varphi_i(\boldsymbol{q}, t_*)}{\partial n} dS(\boldsymbol{q}) \quad \text{for} \quad i = 0,1. \tag{3.1.35}$$

Hence the outer limit of the inner expansion is given as follows:

$$(\varphi_*)^o = f_0(t_*) + \frac{1}{2\pi}\frac{m_0(t_*)}{t_*} + \varepsilon f_1(t_*) + O(\varepsilon^2). \tag{3.1.36}$$

Matching the outer limit of the inner solution (3.1.34) with the inner limit of the outer solution (3.1.27), we obtain all the functions as follows:

$$f_0(t_*) = 0, \quad f_1(t_*) = -\frac{V_0'(t_*)}{2\pi}, \quad F_1(t_*) = \frac{V_0(t_*)}{2\pi}. \tag{3.1.37}$$

Using the method of matched asymptotic expansions, the outer solution of the velocity potential φ_{outer} to second order has been shown to satisfy the wave equation and obtained analytically as follows [100-101]:

$$\varphi_{outer} = -\frac{V_*'(t_* - \varepsilon r_*)}{2\pi r_*} + O(\varepsilon^2), \tag{3.1.38}$$

where the overdot denotes the derivative in time. The outer solution is due to the acoustic radiation associated with the volume oscillation of the bubble.

The inner solution of the velocity potential φ to second order satisfies Laplace's equation in the flow field and the kinematic and dynamic boundary conditions on the bubble surface S are as follows:

$$\nabla_*^2 \varphi_* = O(\varepsilon^2), \tag{3.1.39a}$$

$$\frac{d\mathbf{r}_*}{dt_*} = \nabla_* \varphi_* + O(\varepsilon^2) \quad \text{on } S, \tag{3.1.39b}$$

$$\frac{d\varphi_*}{dt_*} = 1 + \frac{1}{2}\left|\nabla_*\varphi_*\right|^2 - p_{L^*} + O\left(\varepsilon^2\right) \text{ on } S. \tag{3.1.39c}$$

The far-field boundary condition of the inner solution is obtained by matching with the outer solution as follows [105]:

$$\varphi_* \to \frac{1}{2\pi}\left(\varepsilon V_*''(t_*) - \frac{V_*'(t_*)}{r_*}\right) + O\left(\varepsilon^2\right) \text{ as } r_* \to \infty, \tag{3. 1.39d}$$

The initial condition on the bubble surface is given as

$$\varphi_{n*}\big|_{t_*=0} = -R_{t*}\big|_{t_*=0} \quad \text{on } r_* = R_{0*}, \tag{3. 1.39e}$$

where R_{0*} is the initial radius of the bubble.

Here p_{L*} is the liquid pressure on the bubble surface, which is given as,

$$p_{L^*} = p_{B^*} - \sigma_*\nabla\cdot\mathbf{n} \quad \text{on } S, \tag{3.1.40a}$$

$$p_{B^*} = p_{v^*} + p_{g0^*}\left(\frac{V_{0^*}}{V_*}\right)^{\kappa}, \tag{3. 1.40b}$$

where p_{g0} and $p_{g0*} = p_{g0}/\Delta p$ are the dimensional and dimensionless initial partial pressure of the non-condensable gases of the bubble; V_{0*} is the initial bubble volume, and κ is the ratio of the specific heats of the gases; $\boldsymbol{n}$ is the normal vector of the bubble surface, $\nabla\cdot\boldsymbol{n}$ provides the surface curvature and $\sigma_* = \sigma/(R_m\Delta p)$ is the surface tension coefficient.

We assumed in (3.1.39b) that the pressure inside the bubble is uniform since the density of gases is usually three orders of magnitude smaller than that of liquids. We also assume that the expansion and contraction of the bubble gases are adiabatic. Additionally, although there will

be heat and mass transfer between bubble and liquid from bubble surface [93], we will not consider it in this thesis.

Examining the initial and boundary problem of (3.1.39), one can see that the compressible effects appear only in the far field condition (3.1.39d) to the second order approximation. As the basic equation is Laplace's equation, this problem can be modelled using the BIM. The details on the numerical model using the BIM for the problem can be found in [40, 106-107].

Bubble dynamics near a flat rigid boundary are modelled using the method of the image [108]. When the bubble surface is nearly in contact with the rigid boundary, simulations using the BIM are often associated with numerical instabilities. To avoid the numerical instabilities, we remove the thin layer of liquid between the bubble surface and the boundary, join the bubble surface with its image to the boundary and simulate "the combined bubble" [30]. In the simulations performed in this paper, the join takes place when the minimum distance δ_{min} between bubble surface and the boundary is in the range of 0.01 to 0.04.

A composite solution $\varphi_c(\boldsymbol{r}_*, \boldsymbol{t}_*)$ of the inner and outer solutions for the entire domain can be given as follows:

$$\varphi_c(\mathbf{r}_*, t_*) = \varphi_*(\mathbf{r}_*, t_*) - \frac{1}{2\pi}\left(\frac{V_*'(t_* - \varepsilon r_*)}{2\pi r_*} - \frac{V_*'(t_*)}{r_*} + \varepsilon V_*''(t_*)\right) + O(\varepsilon^2). \tag{3.1.41}$$

The mechanical energy of a bubble system consists of the potential energy and the kinetic energy of the bubble system. The potential energy E_P is given as follows [22]:

$$E_{P*} = \frac{p_{g0*}V_{0*}}{\kappa - 1}\left(\frac{V_{0*}}{V_*}\right)^{\kappa-1} + \sigma_* A_* + V_*, \tag{3.1.42}$$

where A^* is the area of the bubble surface. The reference energy is chosen as $R_m^3 \Delta p$.

For a bubble system in a compressible liquid, we introduce the local kinetic energy E_{LK} of the liquid flow in the inner asymptotic region Ω_L near the bubble. Ω_L is bounded by the bubble surface S and a large sphere S_∞ (figure 3.2), with its centre at the centre of the initial bubble surface and with a radius being large compared to the bubble radius and small compared to the wavelength λ of the acoustic wave. Since the flow in the inner region satisfies Laplace's equation to second order, the local kinetic energy E_{LK} is given as follows, by using Gauss's divergence theorem and the outer limit of the inner solution (3. 1.36) [105]:

$$E_{Lk^*} = \frac{1}{2}\int_{\Omega_L} \rho_* \left|\nabla_* \varphi_*\right|^2 dV = \frac{1}{2}\oint_{S+S_\infty} \varphi_* \frac{\partial \varphi_*}{\partial n}\, dS + O\left(\varepsilon^2\right) = \frac{1}{2}\oint_S \varphi_* \varphi_{n^*}\, dS + O\left(\varepsilon\right). \qquad (3.1.43)$$

The kinetic energy of the bubble gases is negligible since the density of gases is usually three orders of magnitude smaller than liquids.

The local energy of a bubble system in a compressible liquid consists of the potential energy E_P and the local kinetic energy E_{LK} as follows [101-102]:

$$E_{L^*} = E_{P^*} + E_{LK^*} = \frac{p_{g0^*} V_{0^*}}{\kappa - 1}\left(\frac{V_{0^*}}{V_*}\right)^{\kappa-1} + \sigma_* S_* + V_* + \frac{1}{2}\oint_S \varphi_* \varphi_{n^*} dS\,. \qquad (3.1.44)$$

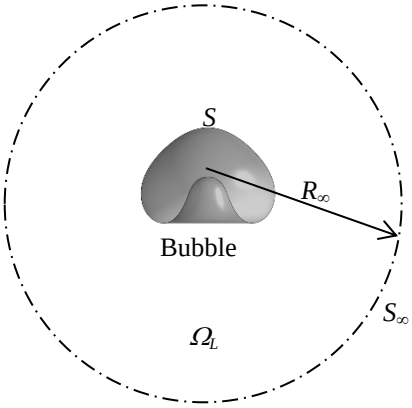

Figure 3.2. Illustration of the local liquid domain Ω_L bounded by the bubble surface S and a large sphere S_∞, with its centre at the centre of the initial bubble surface and with a radius R_∞.

3.2 Numerical analyses

The numerical model is based on the BIM. In the beginning, we have all information of bubble surface and the potential distribution φ on the bubble surface. For the rest of each time steps, we use this data to calculate the tangential velocity on the bubble surface. After having tangential velocity, we use the boundary integral method to obtain the normal velocity on bubble surface. The detail BIM model is referenced to Wang et al. [106, 107].

The calculations are carried out for dynamics of a laser generated gas bubble at the maximum radius R_m = 1.45 mm near a rigid boundary at the dimensionless standoff distance $\gamma = s/R_m$ = 0.9, 0.6 and 0.3 respectively, to compare with the experimental data by [82]. Other computational parameters are chosen as $\kappa = 1.4$, $\varepsilon = 0.013$, $\sigma_* = 0.00051$, $R_*(0) = 0.1$, $R_{t*}(0) = 31$ and $p_{g0*} = 127$. The corresponding dimensional parameters are $\rho = 1000$ kgm^{-3}, $\sigma = 0.07$ Nm^{-1}, $p_\infty = 98.1$ kPa, $p_v = 2.98$ kPa, $R(0) = 1.45$ mm, $R_t(0) = 307$ ms^{-1}, $p_{g0} = 12.1$ MPa.

Figure 3.3 shows the bubble shapes at $\gamma = 0.9$ at various typical times. The bubble expands spherically, but its lower surface is flattened by the rigid boundary towards the end of the expansion (figure 3.3a). During collapse (figure 3.3b), water cannot flow from directly below into the collapsing volume, and the bubble remains in contact with the boundary subsequently. Near the end of the collapse, a liquid jet forms on the distal side of the bubble surface directed towards the boundary. Once it penetrates through the bubble at $t_* = 2.15$ the jet impacts on the boundary immediately, which is associated with higher damage potential as compared to a jet formed away from the wall. For the latter, the jet momentum reduces while it penetrates through the liquid before impact on the wall.

After the jet penetrates the bubble, a bubble rings forms. The jet pointing to the boundary is re-directed radially after it impacts on the boundary, which pushes the inner side of the bubble ring radially. As a result, the jet diameter increases causing a compression of the bubble volume from inside. In the meantime, the bubble ring collapses from other sides rapidly except the bottom, reaching its minimum volume in contact with the boundary at $t_* = 2.30$ (figures 3.3c), when the bubble reaches the maximum pressure and temperature. This is associated with a damage potential too. In addition, a shock wave is emitted at the minimum bubble volume with high-pressure amplitude [93], it impacts on the rigid boundary once it is emitted and has another clear damage potential.

The bubble ring subsequently rebounds mainly upwards and externally along the boundary (figure 3.3d). It next recollapses mainly from the top and the external side (figure 3.3e). The radius of the bubble ring at the end of recollapse is smaller than at the end of collapse. The bubble is kept in contact with the boundary during the second cycle of oscillation.

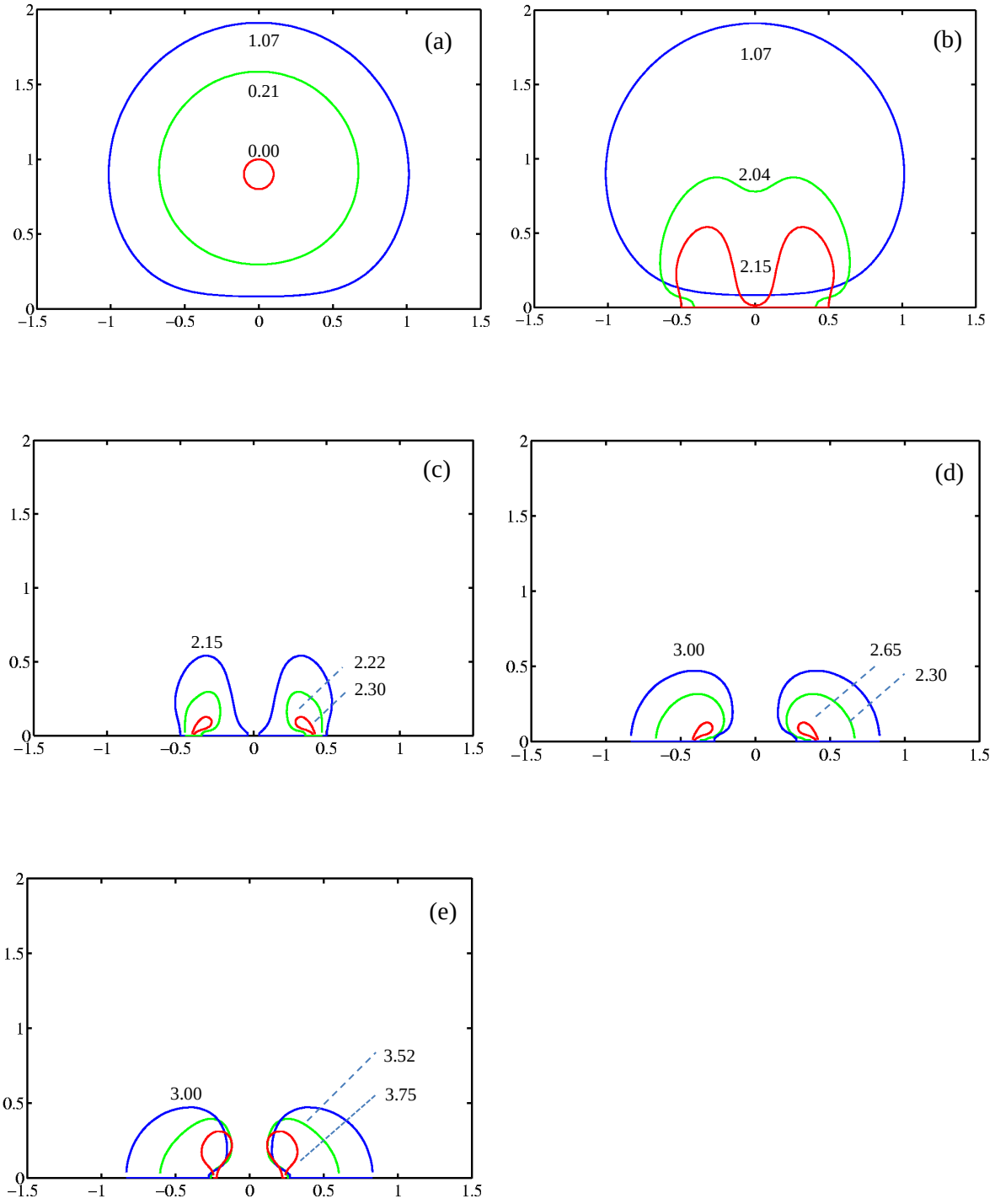

Figure 3.3. The motion of a bubble near a rigid boundary characterized by $\gamma = 0.9$, $\kappa = 1.4$, $\varepsilon = 0.013$, $\sigma_* = 0.00051$, $R_*(0) = 0.1$, $R_{t*}(0) = 31.0$ and $p_{g0*} = 127$. The bubble shapes are in (a) the first expansion phase, (b-c) the first collapsing phase in between singly- and doubly-connected form respectively, (d) during the second expansion phase, and (e) the second collapse phase. Both time and the bubble shape show in figures are in dimensionless.

Figures 3.4 and 3.5 show the bubble shapes at various times at $\gamma = 0.6$ and 0.3, respectively. As expected the lower part of the bubble surface starts being in contact with the boundary earlier than at $\gamma = 0.9$, at the middle and early stage of the expansion phase at $\gamma = 0.6$ and 0.3, as shown in figures 3.4a, 3.5a, respectively. In analogous to the case at $\gamma = 0.9$, the lower part of the bubble surface keeps in contact with the boundary subsequently, and the liquid jet impacts the boundary once it penetrates through the bubble (see figures 3.4b, 3.5b). Comparing figures 3.3b, 3.4b and 3.5b, one can see that the jet is sharper at a larger standoff distance and its width decreases with the standoff distance.

The jet is again redirected horizontally and pushes away the bubble from the inner side after it impacts on the boundary. The bubble ring collapses further from the all sides except for the part in contact with the boundary, reaching its minimum volume and maximum pressure and temperature in contact with the boundary $t_* = 2.32$, 2.34 respectively (figures 3.4c, 3.5c), when a shock wave is emitted and impinges on the boundary once it emits.

The bubble ring then further rebounds (figures 3.4d, 3.5d) and re-collapses (figures 3.4e, 3.5e), predominately from the top and parts external of the bubble surface. The radius of the bubble ring at the end of the second cycle of oscillation is again smaller than at the end of the first cycle. The maximum volume of the bubble during the second cycle increases as the bubble is initiated closer to the boundary.

Now we were considering how bubble behaved as the whole thing. In figure 3.6a we can see how the equivalent bubble radius $R_{eq*} = \sqrt[3]{\frac{3}{4\pi} V_*}$ to be different for those three at $\gamma = 0.9$, 0.6 and 0.3, respectively. The maximum radius reduces significantly from the first to second

cycles of oscillation, so does the oscillation period. The maximum bubble radius at the second-cycle are decreased to 0.57 R_m, 0.59 R_m, 0.65R_m at $\gamma = 0.9$, 0.6 and 0.3, respectively, increasing as the bubble initiated closer to the boundary.

Figure 3.6b shows the corresponding time histories of the bubble centroid z_{cen*}. The bubble migrates slightly away from the boundary during expansion but migrates to the boundary significantly during the collapse. The migration accelerates as the bubble is collapsing, reaching the maximum speed at the minimum volume. The migration towards the boundary is faster at a larger standoff distance during the first cycle of oscillation for the three cases at $\gamma <$ 1.0. This is contrary to the trend at $\gamma > 1.0$ [105], where the bubble migrates to the boundary faster at a smaller standoff distance. This is because the nearer part of the bubble surface is retarded by the boundary during the later stage of the expansion phase as $\gamma < 1.0$ and the retarding effects start earlier at a smaller standoff distance γ.

Figure 3.6c shows the histories of the local energy E_L of the bubble system for the cases. The local energy reduces significantly and rapidly at the inception of the bubble and at the end of the collapse, when shock waves are emitted. It is almost a constant during the rest of time when the compressible effects are approximately negligible. After the shock wave is emitted at inception, about 59%, 60%, 65% of the initial energy is left at $\gamma = 0.9$, 0.6 and 0.3, respectively [103-104]. After the shock wave is emitted at the end of the collapse, only about 14%, 22% and 23% of the initial energy is left with the bubble system at $\gamma = 0.9$, 0.6 and 0.3, respectively.

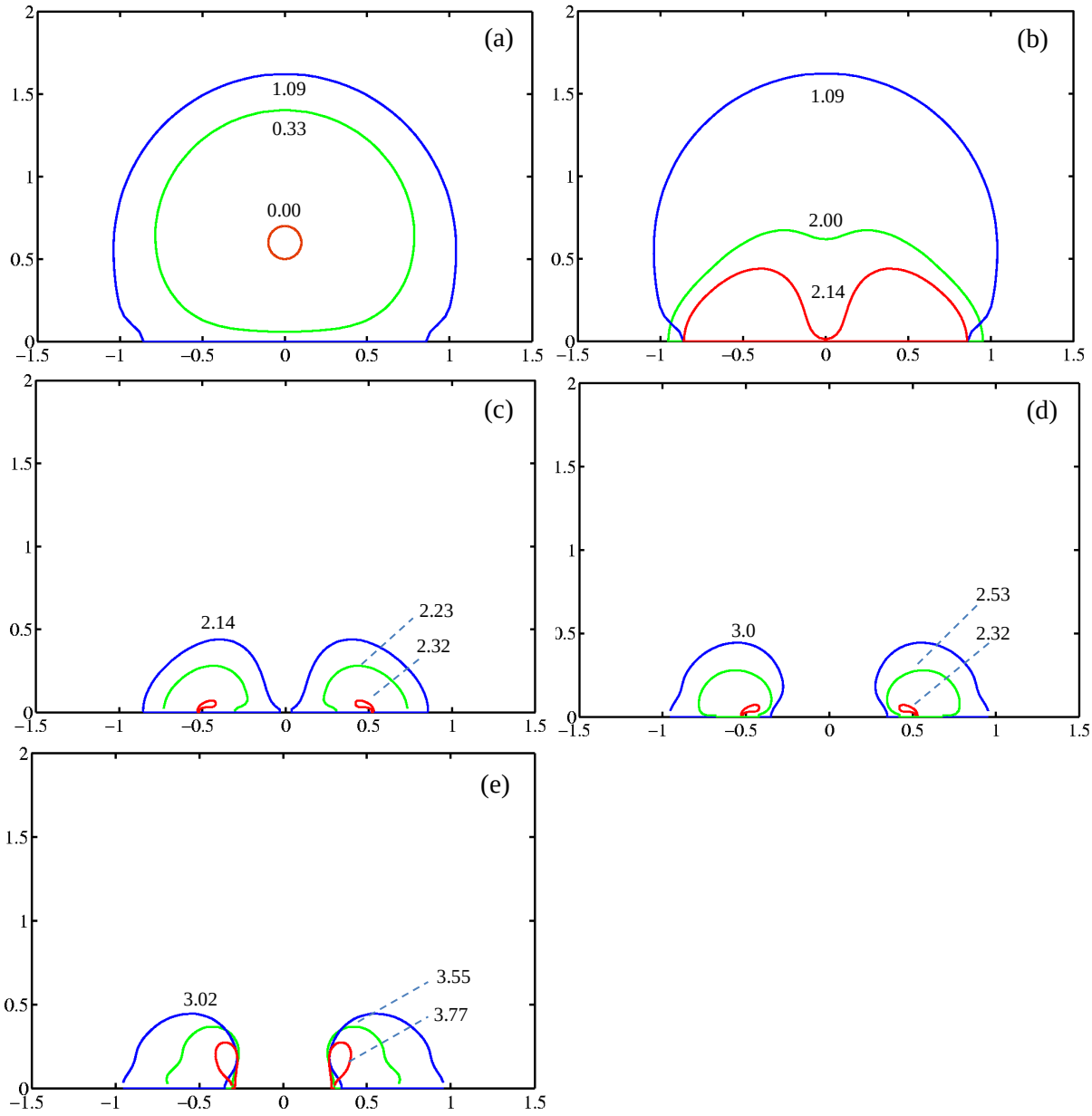

Figure 3.4. Bubble dynamics near a solid boundary at $\gamma = 0.6$, with the other parameters the same as in figure 3.3. Shows the bubble form are during (a) the 1st expansion phase, (b-c) the 1st bubble collapsing phase in a singly- and doubly-connected form respectively, (d) the 2nd expansion phase and (e) the 2nd collapse phase.

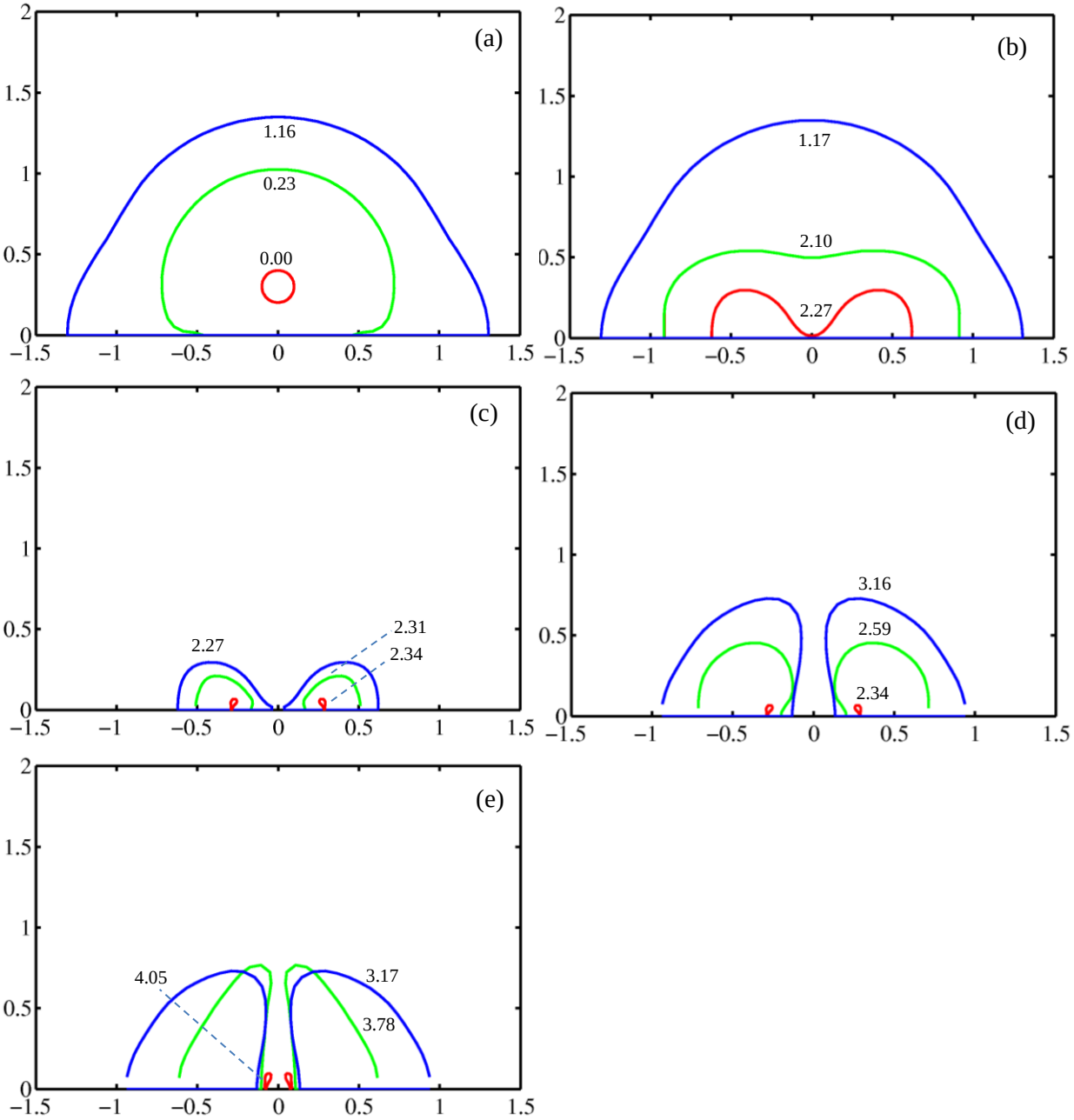

Figure 3.5. Bubble dynamics near a solid boundary at $\gamma = 0.3$, with the other parameters the same as in figure 3.3. The bubble appearances are during (a) the 1st expansion phase, (b-c) the 1st for collapsing phase in a singly- and doubly-connected form respectively, (d) the 2nd expansion phase and (e) the 2nd collapse phase.

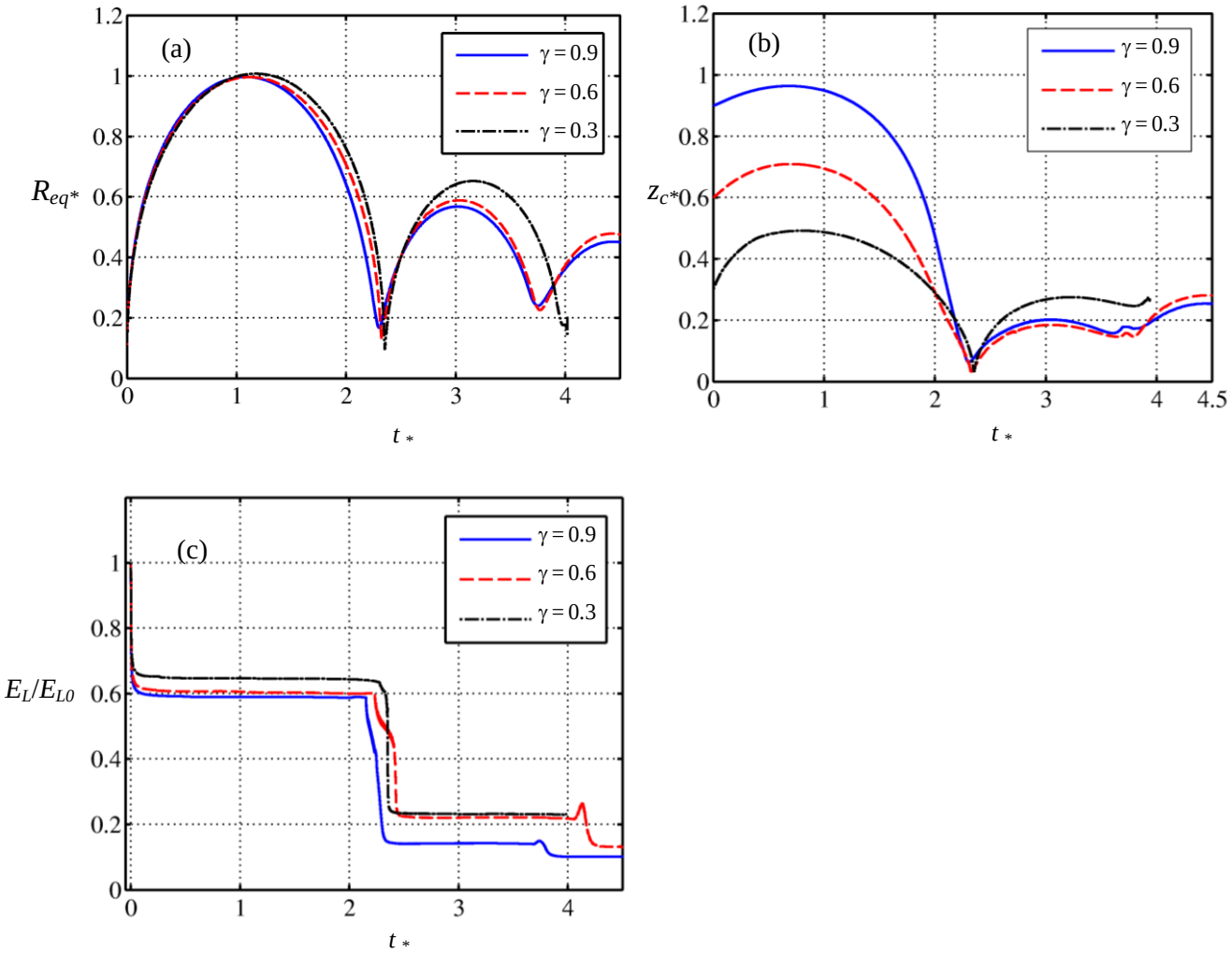

Figure 3.6. Time histories of (a) the equivalent bubble radius R_{eq*}, (b) z-component of the bubble centroid z_{c*}, and (c) local energy E_L/E_{L0} of the bubble system, for the cases in figures 3.3, 3.4 and 3.5, where E_{L0} is the initial local energy.

3.3 Comparison with experiments

Figure 3.7 shows the comparison of the bubble shapes obtained using the compressible BIM and the experiment [82], for cavitation gas bubble dynamics near a rigid boundary at R_m = 1.45 mm and γ = 0.9. The experimental and computational results are shown in the left and right columns, respectively. In addition, the computational results are added overlapped with

the experimental images for a direct comparison. The computation agrees very well with the experiment during the whole first cycle of oscillation (figure 3.7A). The expansion of the lower part of the bubble surface is retarded by the boundary at $t = 34$ μs. It approximately takes the shape of half of a sphere at its maximum volume at $t = 177$ μs, with the lower part of the bubble surface being flattened by the boundary. The upper part of the bubble surface then collapses down, assuming a cone shape at the middle stage of the collapse phase at $t = 296$ μs. The jet shown in the computational results is not visible in the experimental images due to the opaqueness of the bubble surface. Nevertheless, the outer profiles of the bubble obtained in the computation and experiment agree well. The bubble ring of the computation at the end of collapse at $t = 353$ μs agrees well with the experiment when the bubble reaches its minimum volume.

Figure 3.7B shows the comparison during the second cycle of oscillation. The bubble surface in the experiment is not clear due to physical instabilities occurred. Nevertheless, the bubble shapes calculated correlate with the experimental data regarding the outer profile at various times. Both results show that the bubble rebounds and recollapses in contact with the boundary. They agree in terms of the external radius and height of the bubble ring.

A thin circular layer of water exists between the flat boundary and the lower part of the bubble surface since the later stage of the expansion phase, as the bubble initiated with the standoff distance less than the maximum bubble radius. It becomes a thin annulus layer after the jet penetrates the bubble. The part of the bubble surface above the thin liquid layer is almost flat and the thickness of the liquid layer does not change significantly. This feature is shown in the images in figure 3.7 from $t = 177$ to 354 μs. It can be estimated that the vertical acceleration a_{z^*} is small in the thin layer,

$$a_{z*} = a_{z*}\big|_{z=0} + O(\varepsilon_{\min}) = O(\varepsilon_{\min}), \tag{3.3.1}$$

as $a_{z*} = 0$ on the rigid boundary. From the z-component of the Euler equation, we have

$$a_{z*} = -\partial p_* / \partial z_* . \tag{3.3.2}$$

The pressure in the gap can thus be estimated as follows:

$$p_* = p_{L*} + O(\varepsilon_{\min} a_z) = p_{B*} - \sigma_* \nabla \cdot \boldsymbol{n} + O(\varepsilon_{\min}^2) = p_{B*} + O(\varepsilon_{\min}^2) = p_{B*} + O(\varepsilon_{\min}^2), \tag{3.3.3}$$

where the surface tension term is neglected since the curvature radius $\nabla \cdot \boldsymbol{n}$ is small on the flat part of the bubble surface.

The pressure in the thin layer of liquid between the bubble and the boundary is approximately constant and equal to the pressure of the bubble gas. The flow velocity within the thin circular layer must be close to zero. The bubble side of the thin layer remains flattened due to surface tension effects.

A. First cycle of oscillation

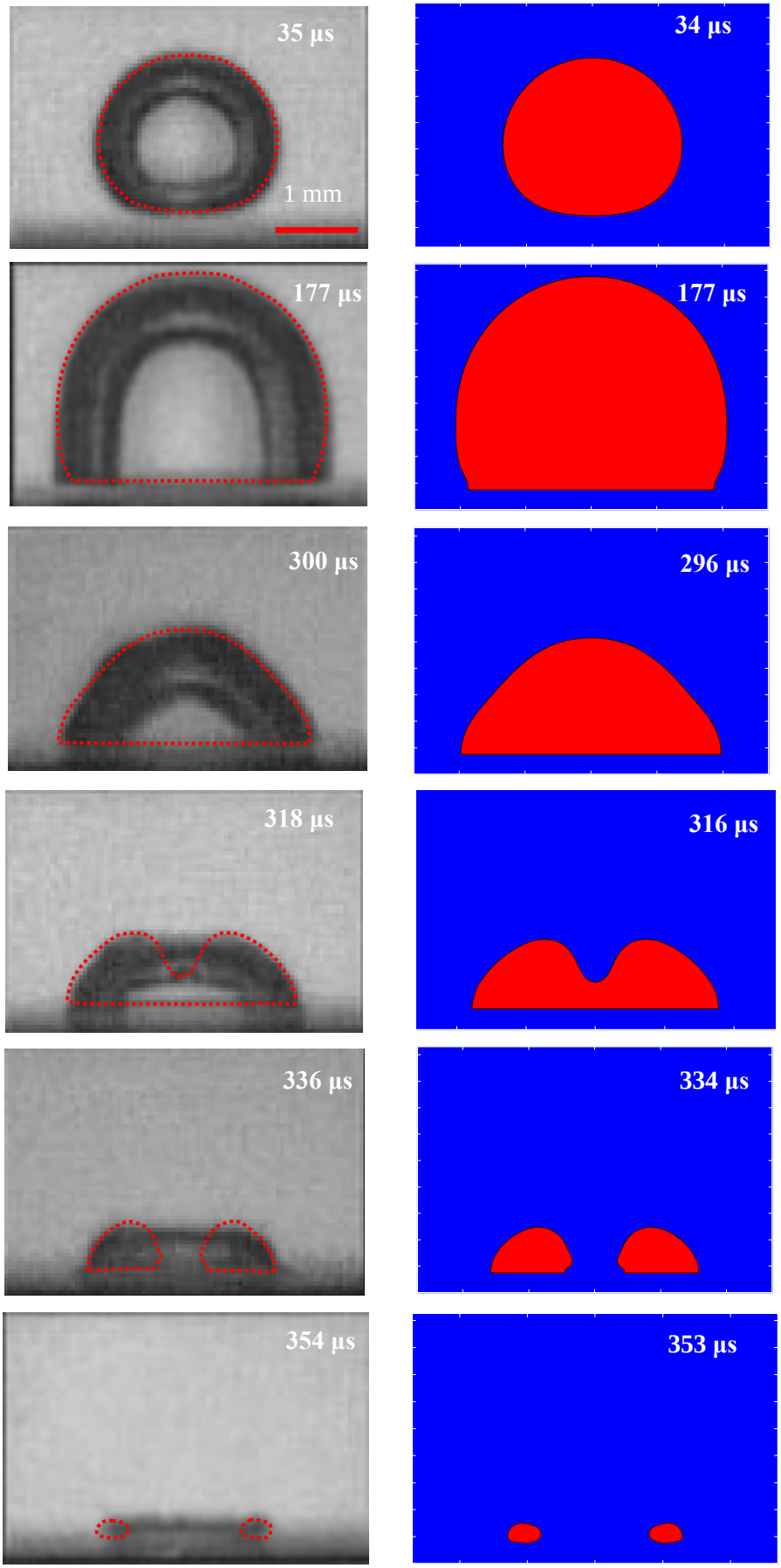

B. Second cycle of oscillation

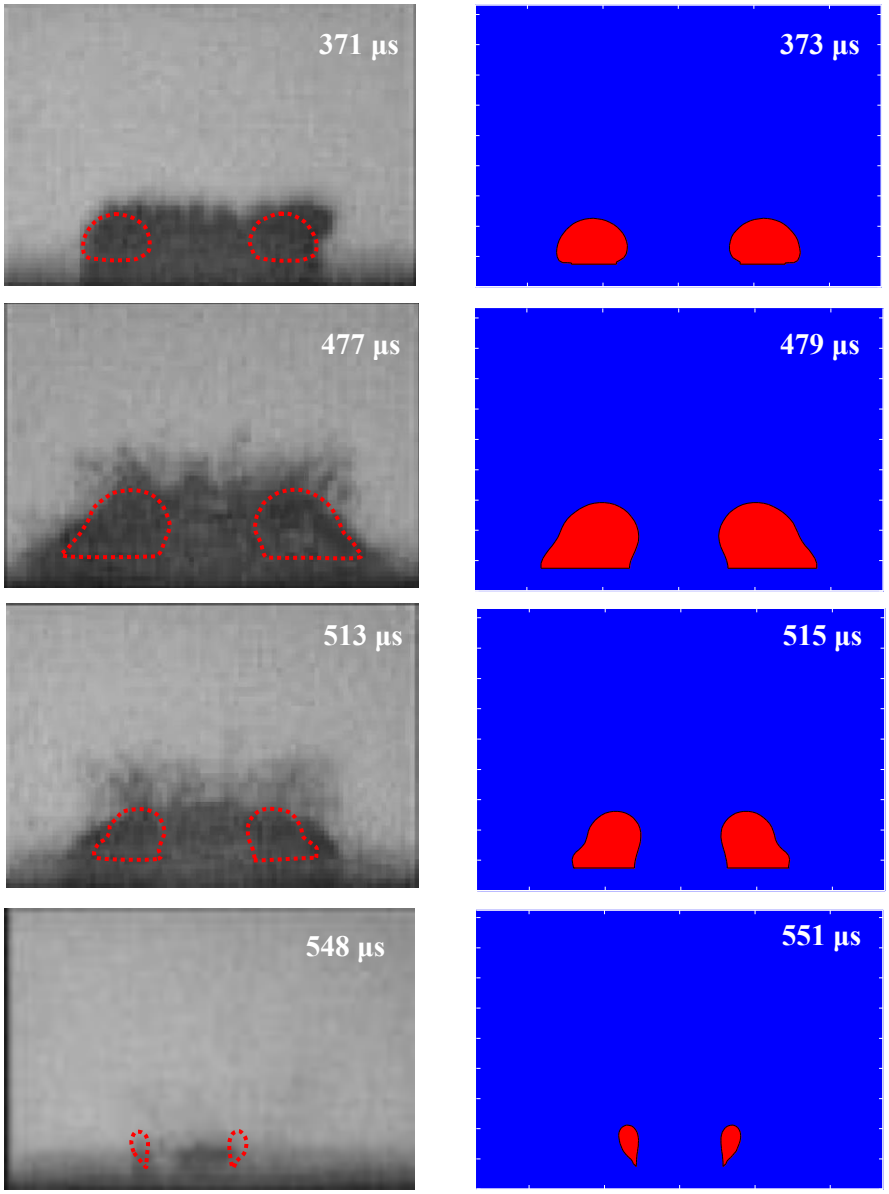

Figure 3.7. Comparison of the compressible BIM computation (in the right column) with the experiment (in the left column) (reproduced with permission from [82]) for the bubble shapes at various times for a cavitation bubble near a rigid boundary at $R_m = 1.45$ mm and $\gamma = 0.9$, the frame width is 3.9 mm for both the computational and experimental results: (A) during the first-cycle of oscillation and (B) during the second-cycle of oscillation. The reminder parameters are the same as in figure 3.7.

A. First collapse

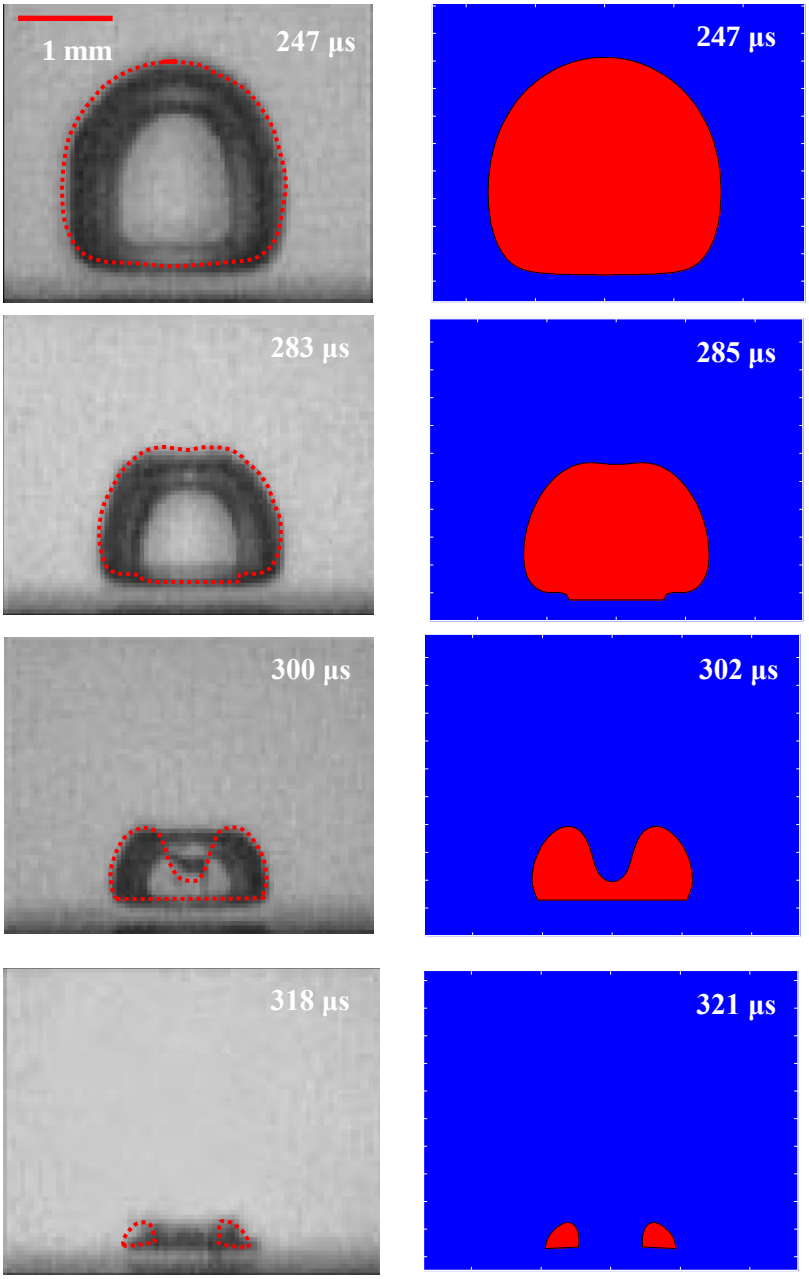

B. Second cycle of oscillation

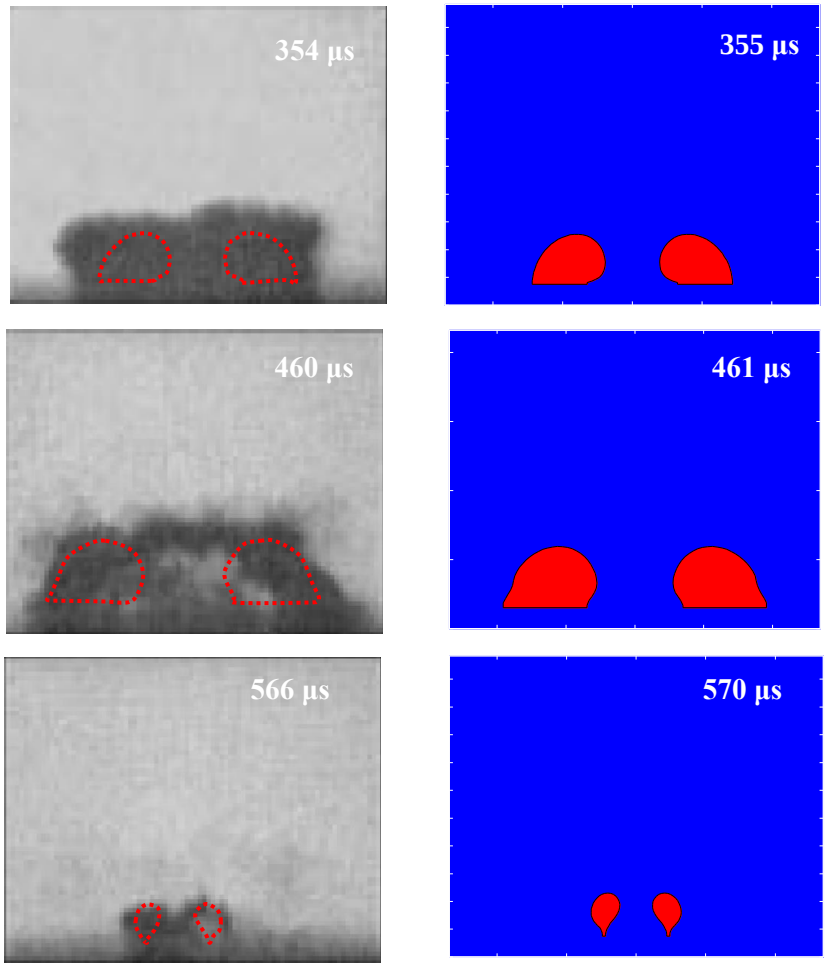

Figure 3.8. Comparison of the compressible BIM computation (in the right column) with the experiment (in the left column) [82] for the bubble shapes at $\gamma = 0.6$: (A) during the first-cycle of oscillation and (B) during the second-cycle of oscillation. The reminder parameters are the same as in figure 3.7.

Figures 3.8 shows the comparison between the computation and the experiment at $\gamma = 0.6$. The computation again agrees very well with the experiment during the whole first cycle of oscillation (figure 3.8A). The bubble takes the shape of a half of sphere with the lower part being flattened by the wall at the middle stage of collapse at $t = 247$ μs. A bubble jet starts at $t = 285$ μs and fully develops at $t = 302$ μs. The bubble ring at the minimum volume calculated

agrees well with the experiment at $t = 321$ μs. Figure 3.8B shows the comparison during the second cycle of oscillation. The bubble shapes calculated correlate with the experiment images. They agree well in terms of the radius of the bubble ring at the end of re-collapse and the period of the second cycle.

Figures 3.9 shows the comparison of the computation with the experiment for the bubble dynamics near a rigid boundary at $\gamma = 0.3$, starting from the late stage of collapse at $t = 280$ μs. The computation agrees very well with the experiment until the end of the collapse phase at $t = 354$ μs. The bubble ring calculated agrees well with the experiment during early rebounding phase to $t = 389$ μs.

A. First collapse

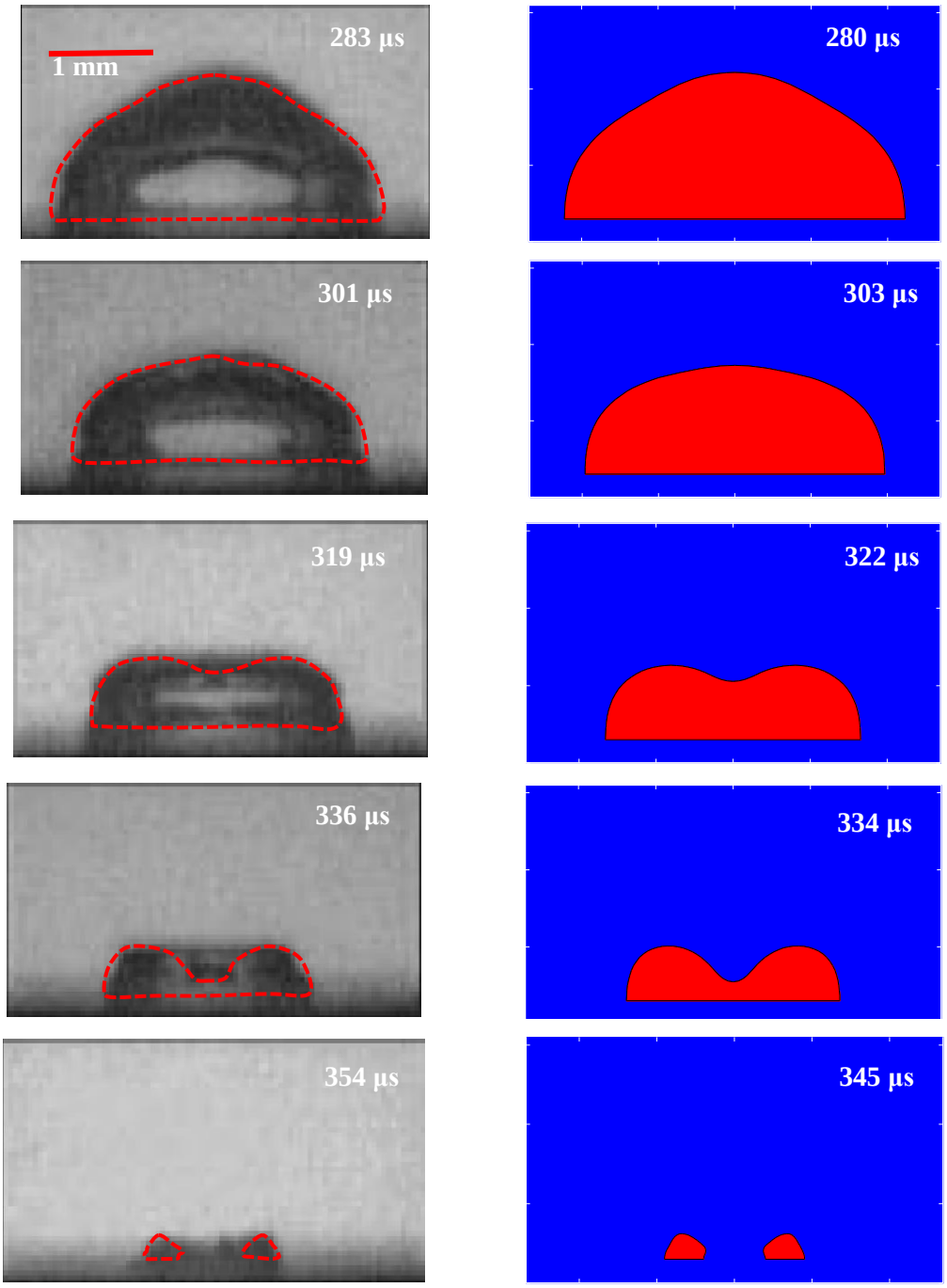

B Second expansion

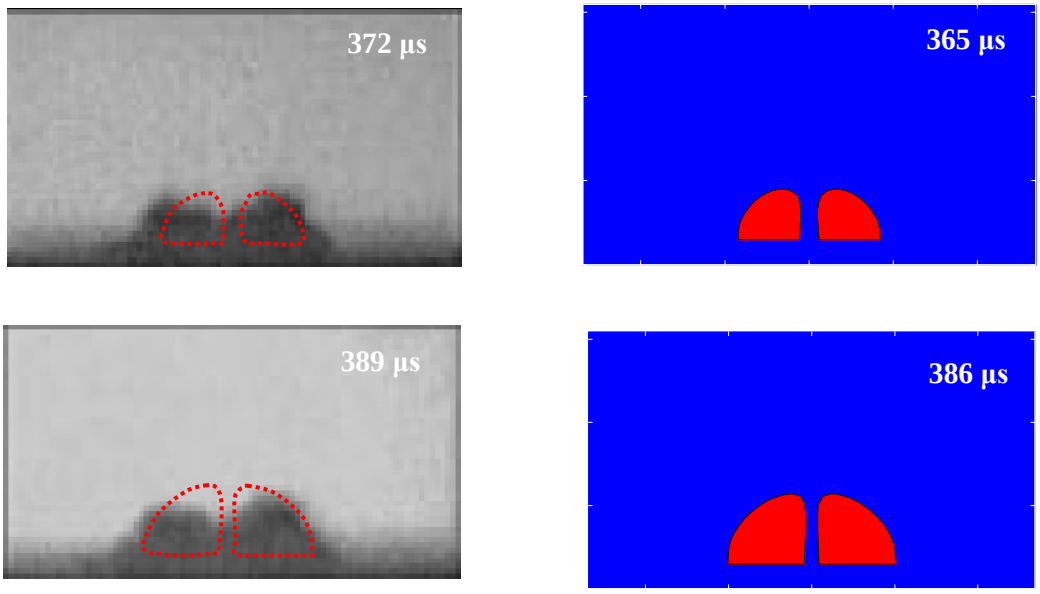

Figure 3.9. Comparison of the compressible BIM computation (in the right column) with the experiment (in the left column) [82] for the bubble shapes at $\gamma = 0.3$: (A) during the first cycle of oscillation and (B) during the second-cycle of oscillation. The reminder parameters are the same as in figure 3.7.

Chapter 4

MICROBUBBLE DYNAMICS WITH VISCOUS EFFECTS

This chapter mainly investigates the bubble dynamics by using the VBIM on the basis of the viscous potential flow theory. The viscous effects are collaborated into the model through including the normal viscous stress of the irrotational flow in the dynamic boundary condition at the bubble surface. The implementation of viscous correction pressure is used to resolve the discrepancy between the physical boundary condition of zero shear stress and the non-zero shear stress of the irrotational flow at a free surface. When a spherical bubble oscillates in a viscous liquid for several cycles of oscillation for Re = 10, the model is in good agreement with the Rayleigh-Plesset equation. It is also in conformity with the experimental data and the simulation results based on the Navier-Stokes equation for transient bubble dynamics near a rigid wall.

4.2 Mathematical model

The continuity equation and the Navier-Stokes equations for the liquid flow surrounding the bubble are as follows:

$$\nabla \cdot \boldsymbol{W} = 0, \tag{4.2.1}$$

$$\frac{\partial \boldsymbol{W}}{\partial t} + (\boldsymbol{W} \cdot \nabla)\boldsymbol{W} = -g\boldsymbol{k} - \frac{\nabla p}{\rho} + \nu \nabla^2 \boldsymbol{W} \,, \tag{4.2.2}$$

where $\boldsymbol{W}$ is the fluid velocity, t is time, P is pressure, ρ is the density of the liquid, g is body force and $\nu = \mu/\rho$ is the kinematic viscous coefficient.

The velocity field $\boldsymbol{W}$ can be expressed as the sum of the irrotational velocity field $\boldsymbol{w}$ and a rotational velocity field $\boldsymbol{v}$

$$\boldsymbol{W} = \boldsymbol{w} + \boldsymbol{v} = \nabla\varphi + \boldsymbol{v}\,, \tag{4.2.3}$$

where the irrotational velocity $\boldsymbol{w}$ can be expressed as the gradient of the velocity potential φ. Substituting the total velocity $\boldsymbol{W}$ into the Navier-Stokes equation, we can get

$$\frac{\partial}{\partial t}(\mathbf{u}+\mathbf{v}) + (\mathbf{u}+\mathbf{v}) \times [\nabla \times (\mathbf{u}+\mathbf{v})] + \frac{1}{2}\nabla|\mathbf{u}+\mathbf{v}|^2 = \mathbf{g} - \frac{\nabla P}{\rho} + \nu\nabla^2(\mathbf{u}+\mathbf{v}). \tag{4.2.4}$$

The viscous correction pressure can p_{vc} is introduced in [29] as below:

$$\frac{\partial \boldsymbol{v}}{\partial t} + \boldsymbol{v} \cdot \nabla\varphi - \boldsymbol{u} \times (\nabla \times \boldsymbol{v}) - \mu\nabla^2 \boldsymbol{v} = -\nabla p_{vc}\,. \tag{4.2.5}$$

Substituting p_{vc} into equation (4. 2.4), yields

$$\nabla\left[\frac{\partial\varphi}{\partial t} + \frac{1}{2}\nabla|\varphi|^2 + \boldsymbol{v}\cdot\nabla\phi + \frac{P - p_{vc}}{\rho} + gz\right] = 0\,. \tag{4.2.6}$$

After integrating (4.2.6) we obtain the modified Bernoulli equation with the viscous correction pressure as follows:

$$\frac{\partial\varphi}{\partial t} + \frac{1}{2}\nabla|\varphi|^2 + \boldsymbol{v}\cdot\nabla\phi + \frac{P - p_{vc}}{\rho} + gz = \frac{P_\infty(t)}{\rho}\,, \tag{4.2.7}$$

where p_∞ is the ambient pressure.

The kinematic condition of the bubble surface is

$$\frac{d\mathbf{r}}{dt} = \nabla\varphi, \tag{4.2.8}$$

the boundary conditions at infinity is

$$\nabla\varphi \to 0. \tag{4.2.9}$$

The dynamic boundary condition on the bubble surface is the balance of the normal stress as follows

$$p_L + \sigma\kappa = p_b + \tau_n, \tag{4.2.10}$$

where p_b the pressure of the bubble gas, p_L is the pressure of the liquid at the bubble surface, τ_n is the normal viscous stress of the irrotational flow, κ is the local mean curvature of the bubble surface, and σ is the surface tension coefficient.

Substituting equation (4.2.10) into equation (4.2.7) we obtain the dynamic condition on the bubble surface as follow:

$$\frac{D\varphi}{Dt} = \frac{1}{2}\left|\nabla\varphi\right|^2 - 2\upsilon\frac{\partial^2\varphi}{\partial n^2} + \frac{\sigma\kappa}{\rho} - \frac{p_b - p_{vc} - P_\infty(t)}{\rho} - gz. \tag{4.2.11}$$

We chose the density ρ_∞ in the undisturbed liquid as the reference density and the maximum bubble radius R_m as the reference length. The reference velocity is thus obtained as $U = \sqrt{\Delta p/\rho_\infty}$. The reference pressure is $\Delta p = p_\infty - p_v$. Where p_v is the partial pressure of vapour of the bubble and p_∞ is the hydrostatic pressure in the undisturbed liquid. We introduce dimensionless quantities indicated by asterisks as follows,

$$\boldsymbol{r}_* = \frac{\boldsymbol{r}}{R_m}, \quad t_* = \frac{t}{R_m}\sqrt{\frac{\Delta \mathrm{p}}{\rho}}, \quad \varphi_* = \frac{\varphi}{R_m}\sqrt{\frac{\rho}{\Delta p}}, \tag{4. 2.12a, b, c}$$

$$\sigma_* = \frac{\sigma}{R_m \Delta p}, \quad k_* = R_m k, \quad p_{vc*} = \frac{p_{vc}}{\Delta p}, \quad z_* = \frac{z}{R_m}, \tag{4.2.12d, e, f, g}$$

where $\boldsymbol{r}$ is the position vector, φ is the velocity potential of the liquid, t is the time, and p is the pressure.

The dimensionless dynamic condition on the bubble surface is obtained as follows. Substituting (4.2.12) into (4.2.11) yields,

$$\frac{\rho}{\Delta p}\frac{D\varphi_*}{Dt_*} = \frac{1}{2}\left|\nabla\varphi_*\right|^2 \frac{\rho}{\Delta p} - 2\upsilon\frac{\partial^2\varphi_*}{\partial n^2}R_m\sqrt{\frac{\Delta p}{\rho}} + \frac{\sigma_*\kappa_* R_m \Delta p}{\rho R_m} - gz_* R_m - \frac{p_b - p_{vc} - P_\infty(t)}{\rho}. \tag{4.2.13}$$

Substituting (3. 1.40b) into (4.2.11) yields, expressing bubble pressure as the following:

$$\frac{\rho}{\Delta p}\frac{D\varphi_*}{Dt_*} = \frac{1}{2}\left|\nabla\varphi_*\right|^2 \frac{\rho}{\Delta p} - 2\upsilon\frac{\partial^2\varphi_*}{\partial n^2}R_m\sqrt{\frac{\Delta p}{\rho}} + \frac{\sigma_*\kappa_* R_m \Delta p}{\rho R_m} - gz_* R_m - \frac{p_v + p_{g0}\left(\frac{V_0}{V}\right)^\kappa - P_\infty(t)}{\rho} + \frac{p_{vc}}{\rho} \tag{4.2.14}$$

Substituting the viscous correct pressure from (4.2.20) into the above equation, we get:

$$\frac{\rho}{\Delta p}\frac{D\varphi_*}{Dt_*} = \frac{1}{2}\left|\nabla\varphi_*\right|^2 \frac{\rho}{\Delta p} - 2\upsilon\frac{\partial^2\varphi_*}{\partial n^2}R_m\sqrt{\frac{\Delta p}{\rho}} + \frac{\sigma_*\kappa_* \Delta p}{\rho} - gz_* R_m - \frac{p_v + p_{g0}\left(\frac{V_0}{V}\right)^\kappa - P_\infty(t)}{\rho} + \frac{p_{vc}}{\rho}. \tag{4.2.15}$$

Dividing by the factor $\rho/\Delta p$ yields

$$\frac{D\varphi_*}{Dt_*} = \frac{1}{2}\left|\nabla\varphi_*\right|^2 - 2\upsilon\frac{\partial^2\varphi_*}{\partial n^2}R_m\sqrt{\frac{\Delta p}{\rho}} + \sigma_*\kappa_* - \frac{z_*}{Fr^2} - \frac{p_v - P_\infty(t)}{\Delta p} - p_{g0*}\left(\frac{V_0}{V}\right)^\kappa + p_{vc*} \tag{4.2.16}$$

or

$$\frac{D\varphi_*}{Dt_*} = \frac{1}{2}\left|\nabla\varphi_*\right|^2 - \frac{2}{Re}\upsilon\frac{\partial^2\varphi_*}{\partial n^2} + \sigma_*\kappa_* - \frac{z_*}{Fr^2} + 1 - p_{g0*}\left(\frac{V_0}{V}\right)^\kappa + p_{vc*}, \tag{4.2.17}$$

where $p_{g0*} = p_0/\Delta p$ is the strength parameter, $Re = \left(R_m\sqrt{\frac{\Delta p}{\rho}}\right)\Big/\upsilon$ is the Reynolds number, $Fr = \sqrt{\frac{\Delta p}{\rho g R_m}}$ is the Froude number.

As the relatively low viscosity of the gas inside the bubble, the tangential stress of the liquid flow at the bubble surface should be negligible. However, there is shear stress on the bubble surface because the irrotational velocity is not zero. In order to deal with this difference, a viscous pressure correction is proposed at the free surface. Joseph and Wang [29] introduced a viscous pressure correction that performs the same energy from the liquid to the gas as that by the shear stress of the irrotational flow. The energy to be used for the viscous pressure correction P_{vc} on each surface element dS is $\boldsymbol{dW} = -\boldsymbol{v}_n P_{\mathrm{vc}}\boldsymbol{dS}$ and the work produced by the liquid to the gas by the shear stress of the irrotational flow is $\boldsymbol{dW} = \boldsymbol{v}_\tau \cdot \boldsymbol{\tau}_s \boldsymbol{dS}$. Thus, we have,

$$-u_n P_{\mathrm{vc}} = \boldsymbol{u}_\tau \cdot \boldsymbol{\tau}_s . \tag{4.2.18}$$

The pressure correction thus satisfies the following relation on the bubble surface

$$\int_S u_n(-p_{\mathrm{vc}})dS = \int_S \boldsymbol{u}_\tau \cdot \boldsymbol{\tau}_s \, dS . \tag{4.2.19}$$

This model is termed as the viscous correction of VPF model (VCVPF) [29].

To avoid singularity at $u_n = 0$, we make the following change to (4.2.18)

$$P_{vc} = \begin{cases} -\dfrac{u_\tau \tau_s}{u_n} & \text{for } |u_n| \geq 0.01 \\ 0 & \text{for } |u_n| < 0.01 \end{cases}. \tag{4.2.20}$$

According to Boulton & Blake [115] τ_s is given as follows:

$$\tau_s = 2\mu \boldsymbol{n} \cdot \nabla \boldsymbol{u} \cdot \tau = 2\mu \tau \cdot \nabla \boldsymbol{u} \cdot \boldsymbol{n} = 2\mu \left(\frac{\partial u_n}{\partial s} + \kappa_1 u_\tau \right), \tag{4.2.21}$$

where $\kappa_1 = 1/R_1$ is planar curvature, and R_1 is principal radii of curvature. The term $\dfrac{\partial u_n}{\partial n}$ needed in (4.2.18) can be calculated as following

$$\frac{\partial u_n}{\partial n} = \frac{\partial^2 \varphi}{\partial n^2} = \begin{cases} -\dfrac{\partial^2 \varphi}{\partial s^2} + \kappa \dfrac{\partial \varphi}{\partial n} - \dfrac{n_z}{r} \dfrac{\partial \varphi}{\partial s} = -\dfrac{\partial u_\tau}{\partial s} + \kappa u_n - \dfrac{n_z}{r} u_\tau & \text{for } r > 0 \\ -2\dfrac{\partial^2 \varphi}{\partial s^2} + \kappa \dfrac{\partial \varphi}{\partial n} = -2\dfrac{\partial u_\tau}{\partial s} + \kappa u_n & \text{for } r = 0 \end{cases}. \tag{4.2.22}$$

Following Boulton & Blake [115] τ_n is given as follows:

$$\tau_n \approx 2\mu \frac{\partial^2 \varphi}{\partial n^2}. \tag{4.2.23}$$

After obtaining τ_s using (4.2.21) and $\dfrac{\partial u_n}{\partial n}$ from (4.2.22), we then obtain the viscous correction pressure from (4.1.20).

4.2 Validating the numerical model and comparing with experiment

4.2.1 Comparison with the Keller-Miksis equation

We first compare the viscous BIM model with that of the Keller-Miksis equation (KME) by considering a spherical bubble oscillating in an infinite fluid. The parameters used are $R_0 = 4.5$ μm, $p_0 = 101.3$ kPa, $\rho = 1000$ kg/m^3, $\varepsilon = 100$, $\sigma = 0.073$ N/m, $\kappa = 1.67$ and $p_{a*} = 0$. The Reynolds number for the case is $Re = 45$. Figure 4.2 shows the comparison of the bubble radius histories calculated using the viscous BIM model and the Keller equation. From the figure, we can see that the viscous BIM model agrees well with the KME for the six cycles of bubble oscillation. The maximum bubble radius decreases and the minimum radius increases with the cycle of oscillation. The amplitude and period reduce significantly with the cycle of oscillation due to the viscous effects. For microbubble dynamics, the viscous effects are significant for multiple cycles of oscillation.

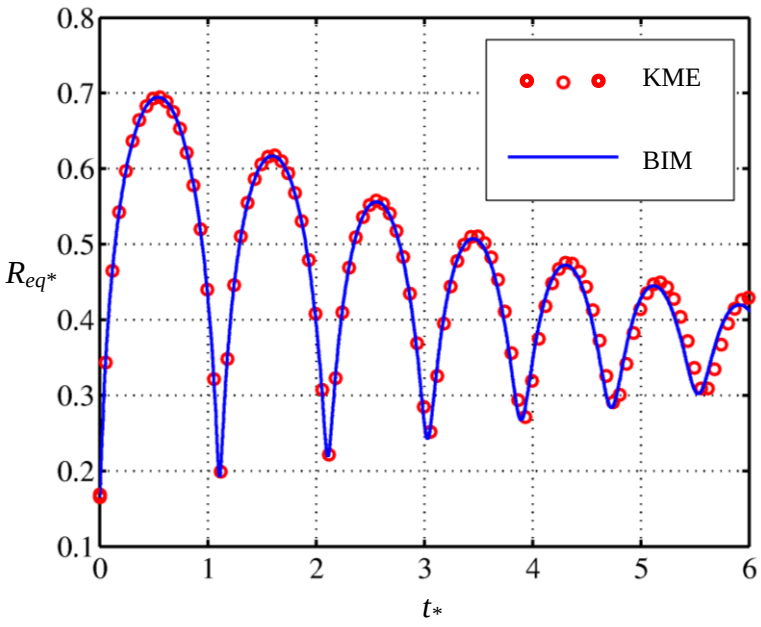

Figure 4.2. Comparison of the time histories of the bubble radius calculated from the viscous BIM model and the Keller-Miksis equation (KME). The parameters are used $R_0 = 4.5$ μm, $\varepsilon = 100$, $\kappa = 1.67$, $p_0 = 101.1$ kPa, $\rho = 1000$ kg/m^3, $p_{a*} = 0$, $\sigma = 0.073$ N/m and $Re = 45$.

4.2.2 Comparison with the experiment

Ohl et al. [11] carried out an experiment for cavitation gas bubbles generated by a laser beam near a rigid boundary for the dimensionless standoff distance of the bubble from the wall γ = 1 and the maximum bubble radius $R_{max} = 1$ mm. All the details of this experiment were well controlled and recorded by a high-speed camera. Another computational result used for comparison was provided using an axisymmetric model based on the Navier-Stokes equations [28]. The parameters for the case are $p_{g0} = 42$ bar, $R_0 = 0.2$ mm, $T_{amb} = 300$ K and $T_{c0} = 1998$ K, in which T_{c0} is the difference between the temperature at the centre of the bubble and the ambient temperature and T_{amb} is the ambient temperature in the liquid fluid. We will compare our results obtained from the viscous BIM model with the results from both the experiments [11] and the numerical model based on the Navier-Stokes equation [28].

Although we chose the same initial pressure with [28] in the viscous BIM model, we used a slightly bigger initial radius $R_0 = 0.224$ mm to make sure that bubble radius to reach 1 mm at the first maximum. This is because the Navier-Stokes model [28] considers the effects of heat transfer, which is neglected in the viscous BIM model. Following Best and Kucera's [40], the ratio of specific heat is chosen $\kappa = 1.4$, and other parameters are $\rho = 1000$ kg·m^{-1}, $p_0 = 101.3$ kpa and $\mu_{water} = 0.001$ kg·m^{-1} s^{-1}.

Both the visous BIM model and Navier-Stoke model agree well with the experiments in terms of bubble expansion and collapse and jet formation, as shown in figure 4.3. The rigid boundary is allocated at the bottom of the picture. During the first expansion, most part of the bubble surface keeps spherical except for the bottom of it is flattened by the rigid boundary when it gets close to the boundary (figure 4.3a). After reaching the maximum radius, it collapses with the bubble surface keeping approximately spherical, except for the bottom part

has no significant movement (figure 4.3b). At the end of collapsing, a liquid jet develops rapidly from the top of the bubble surface towards the rigid boundary (figure 4.3c). Although we can see both computation models providing good agreements with the experiment, the time sequence and the jet shape obtained from the viscous BIM model agrees better with the experiment.

a. Expansion phase

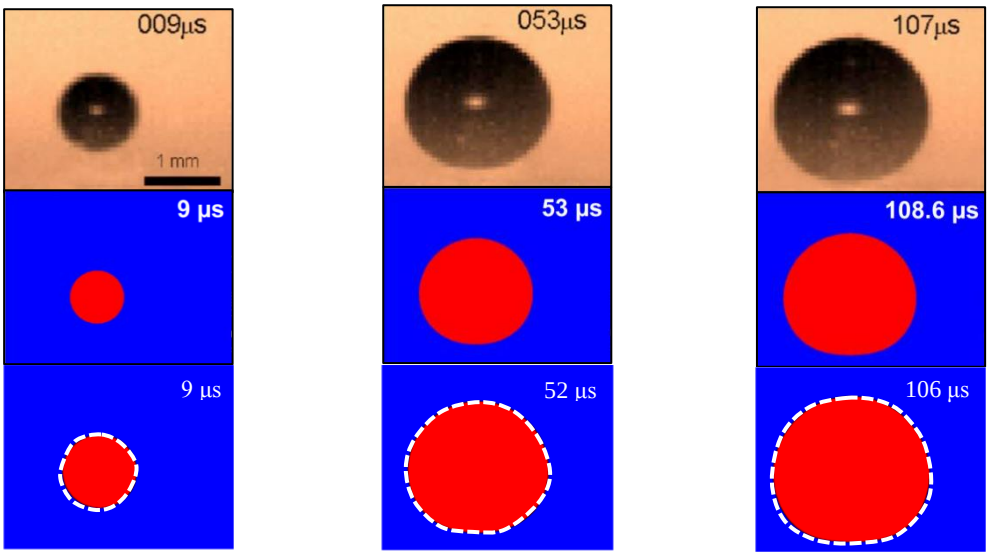

b. Collapse phase

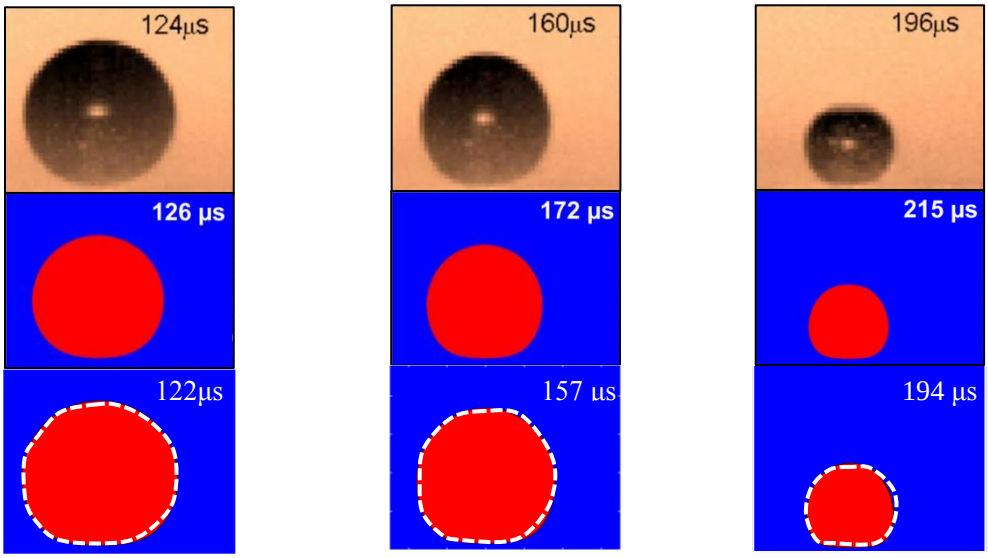

c. Collapse phase: jet formation

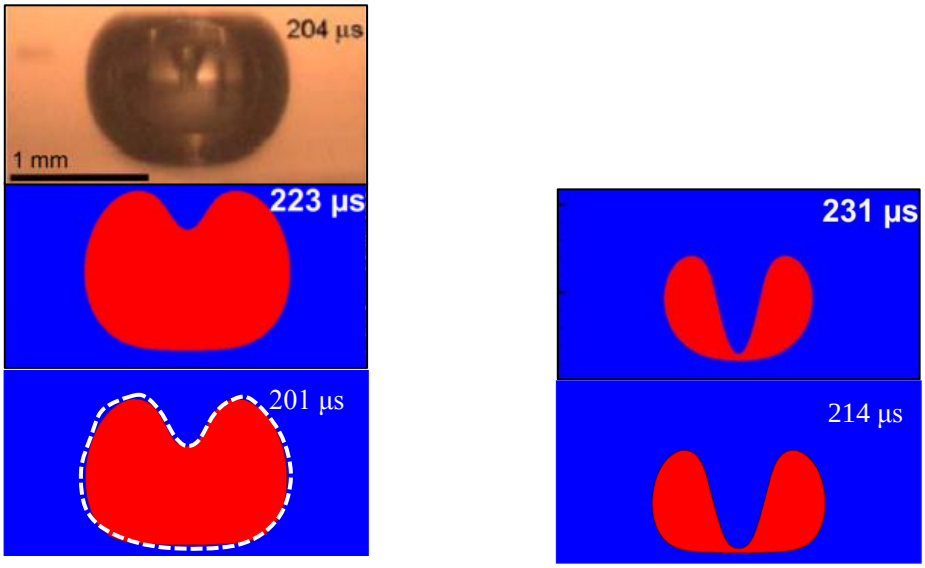

Figure 4.3. Comparison of the bubble shapes as obtained from the experiment ([11] in the first row of each phase), a computational model based on the Navier-Stokes equation ([28], in the second row) and the visous BIM (in the third-row together with dash line bubble shape from experiment). The bubble shapes are shown during (a) the expansion phase, (b) the collapse phase and (c) the jet formation. The rigid boundary is located at the lower borders of frames. The parameters in the BIM model are chosen as $R_0 = 0.224$ mm, $p_{g0} = 42$ bar, $\gamma = 1.0$, $\mu_{water} = 0.001$ kg·(m s)$^{-1}$, $p_\infty = 101.3$ Kpa, $\rho = 998$ kg·m^{-1}, and $\kappa = 1.4$.

Chapter 5

BUBBLE DYNAMICS IN A COMPRESSIBLE LIQUID WITH VISCOUS EFFECTS

This chapter considers bubble dynamics in a compressible and viscous liquid. The viscous effects are modelled using the viscous potential flow theory. The compressible effects are modelled using the weakly compressible theory. The numerical results are shown in good agreement with the Keller-Miksis equation, experiments and computations based on the Navier-Stokes equations.

5.1 Physical and mathematical model

Consider the dynamics of a gas bubble near a rigid flat boundary in a viscous and compressible liquid. A Cartesian-coordinate system is set, with the *x*-axis at the rigid boundary and the *z*-axis along the axis of symmetry for the configuration, as illustrated in figure 1. It is assumed that it is a potential flow in the bulk volume of the fluid except for a thin viscous boundary layer at the bubble surface.

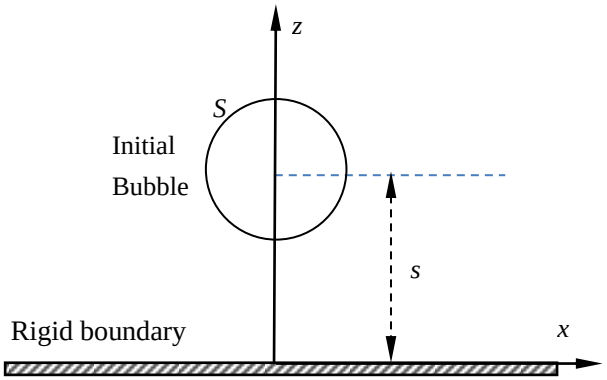

Figure 5.1. Illustration of a bubble near a rigid boundary, with a standoff distance, *s* from the centre of the initial bubble surface to the boundary, and the coordinates used.

The reference length, density and pressure are chosen as the maximum bubble radius R_{max}, the density of the liquid ρ_∞ in the undisturbed liquid, and $\Delta p = p_\infty - p_v$, respectively, where p_∞ and p_v are the ambient pressure and vapour pressure of the liquid, respectively. The reference velocity is therefore defined as $U = \sqrt{\Delta p / \rho_\infty}$. Dimensionless quantities are denoted by subscripts "*", as follows:

$$\boldsymbol{r}_* = \frac{\boldsymbol{r}}{R_{max}}, \quad t_* = \frac{U}{R_{max}} t, \quad \varphi_* = \frac{\varphi}{R_{max} U}, \quad p_* = \frac{p - p_\infty}{\Delta p}, \tag{5.1}$$

where $\boldsymbol{r} = (x, y, z)$, t is the time, φ the velocity potential and p the pressure of the liquid flow.

The highest speed of the liquid flow inducing by bubble dynamics is usually related with the velocity of the bubble jet, which is often lower than 200 m s^{-1} at normal ambient pressure, according to the observation of experiments Benjamin & Ellis [39], Brujan & Matsumoto [46], Lauterborn & Bolle [66], Lauterborn & Ohl [68], Lindau, & Lauterborn [79], Philipp & Lauterborn [82], Shima et al. [89], Tomita & Shima [95], Vogel et al. [96, 97], Yang et al. [109] and Zhang et al. [114].

The flow induced by the bubble dynamics is assumed to be associated with a low Mach number, ε, since the speed of sound in water is about 1500 m s^{-1}, defined as follows:

$$\varepsilon = \frac{U}{c} << 1, \tag{5.2}$$

where c is the speed of sound of liquid. A newly formed laser bubble's surface expands with an initial velocity of about 2450 ms^{-1} is observed by Lauterborn & Vogel [69], which reduces rapidly to about 250 ms^{-1} within 140 ns.

We divide the bulk fluid domain of the inviscid flow into two regions: the inner region near the bubble where $(x, y, z) = O(R_{max})$ and the outer region far away from the bubble where $(x, y, z) = O(\lambda)$, where $\lambda = cR_{max}/U$ is the wavelength of acoustic waves. Using the method of matched asymptotic expansions, the outer solution was shown to satisfy the linear wave equation to second order in terms of the Mach number and an analytical solution was obtained as follows Wang [105, 109]:

$$\varphi_* = -C_0 \frac{\dot{V}_*\left(t_* - \varepsilon r_*\right)}{r_*} + O\left(\varepsilon^2\right), \tag{5.3}$$

where V is the transient bubble volume and C_0 is a given constant with $1/(2\pi)$ for a bubble in an unbounded liquid and near a rigid boundary and a value of $1/(4\pi)$, respectively.

By following Wang & Blake [103, 104], the inner solution to second order satisfies Laplace's equation and the kinematic boundary condition on the bubble surface S, as following:

$$\nabla_*^2 \varphi_* = O\left(\varepsilon^2\right), \tag{5.4a}$$

$$\frac{D\mathbf{r}_*}{Dt_*} = \nabla_* \varphi_* + O\left(\varepsilon^2\right) \quad \text{on } S, \tag{5.4b}$$

The far-field boundary condition of the inner solution is obtained by matching with the outer solution as follows Wang [102]:

$$\varphi_* \to C_0\left(\varepsilon\ddot{V}_*(t_*) - \frac{\dot{V}_*(t_*)}{r_*}\right) + O\left(\varepsilon^2\right) \quad \text{as} \quad r_* \to \infty. \tag{5.4c}$$

The initial condition on the boundary is given as

$$\varphi_{n*}\big|_{t_*=0} = -R_{t0*} \quad \textbf{on} \;\; r_* = R_{0*}, \tag{5.4d}$$

where $\boldsymbol{n}$ is the unit normal at the bubble surface pointing to the gas side, R_{0*} and R_{t0*} are the initial radius of the bubble and its initial rate of change, respectively.

A thin viscous boundary layer exists at the bubble surface if the associated Reynolds number is $O(10)$ or larger Boulton-Stone & Blake [115]. In the viscous potential flow theory, the normal stress balance at the bubble surface and the surface tension is given as follows:

$$p_L + p_{\text{vc}} + \sigma\nabla\cdot\boldsymbol{n} - \tau_n = p_B, \;\; \tau_n = 2\mu\frac{\partial^2\varphi}{\partial^2 n}, \tag{5.5}$$

where p_L is the liquid pressure at the bubble surface, σ surface tension, τ_n the normal viscous stress, p_{vc} viscous pressure correction and μ is the viscosity of the liquid.

Due to the relatively low viscosity of the gas inside the bubble, the tangential stress at the bubble surface is supposed to be zero. However, the shear stress is non-zero because of potential flow. The viscous correction pressure carried out by Joseph and Wang [29] to resolve this discrepancy. A rational model for the viscous correction is unavailable in the case. We assume that the viscous correction pressure p_{vc} is proportional to the normal stress $p_{vc} = -C\tau_n$ Manmi & Wang [123]:

$$p_L + \sigma\nabla\cdot\boldsymbol{n} - 2\mu(1+C)\frac{\partial^2\varphi}{\partial n^2} = p_B. \tag{5.6}$$

The constant C is to be determined as follows. In order to satisfy energy conservation for the liquid flow, the viscous correction pressure is provided to fulfil the equal power done by the shear stress at the free surface, which is introduced by Joseph & Wang [29] and the relation is given by the follows,

$$\int_S u_n(-p_{\mathrm{vc}})\,dS = \int_S \boldsymbol{u}_\tau \cdot \boldsymbol{\tau}_s\,dS\,, \tag{5.7}$$

where $\boldsymbol{\tau}_s$ is the shear stress at the bubble surface.

Using the Bernoulli equation, the dynamic boundary condition at the bubble surface can be written as

$$\frac{D\varphi_*}{Dt_*} = 1 + \frac{1}{2}\left|\nabla_*\varphi_*\right|^2 - p_{g0^*}\left(\frac{V_{0^*}}{V_*}\right)^\kappa + \sigma_*\nabla\cdot\boldsymbol{n} - \delta^2 z_* + \varepsilon\frac{V_0''(t_*)}{2\pi} - \frac{2(1+C)}{Re}\frac{\partial^2\varphi_*}{\partial n^2} + O\left(\varepsilon^2\right) \quad \text{on } S, \tag{5.4e}$$

where , $\sigma_* = \sigma/(R_{max}\Delta p)$ the surface tension, $\delta = \sqrt{\rho g R_{max}/\Delta p}$ the buoyancy parameter, $p_{g0^*} = p_{g0}/\Delta p$ is the initial partial pressure of the bubble gases inside the bubble, κ the polytropic index of the bubble gas, V_{0^*} is the initial bubble volume and $Re = R_0\sqrt{\Delta p\,\rho}/\mu$ is the Reynolds number. The expanding and collapsing of the gases bubble is assumed adiabatic. The thermal effects related to this phenomenon will not be considered which may reference to Szeri et al. [93]. We assumed in (5.4e) that the expansion and contraction of the bubble gases are adiabatic. We do not consider the thermal effects associated with this phenomenon, which may reference to Szeri et al. [93].

Examining the initial and boundary value problem of (5.4), one can see that the compressible effects to second order appear only in the far field condition (5.4c), and the viscous effects appear in the dynamic boundary condition at the bubble surface (5.4e), since it is the modified

Laplace's equation, which can be simulated by using the boundary integral method (BIM). Curtiss et al. [54], Wang [105] and Wang et al. [106] developed the numerical model by using BIM for this problem.

The collapse of a non-spherical bubble is often resulting in the formation of a high-speed liquid jet. Subsequently, the jet impacts on the opposite bubble surface and thus penetrates the bubble, hence the liquid domain transformed from a singly connected to a doubly connected domain. There is a non-unique solution for a potential problem in a doubly connected domain. By using a vortex sheet by Zhang, Duncan & Chahine [111] and Zhang & Duncan [112] or a branch cut by Best [40] the doubly connected domain can be transferred to singly connected domain.

A bubble torus has been modelled with a vortex ring inside. A vortex ring initially locates in the cross-section of the bubble. Pedley [124] and Lundgren & Mansour [125] described this method. Based on the earlier ideas to simulate the transformation of singly connected bubble to a toroidal bubble Wang, et al. [107, 108] developed a vortex ring model to handle this problem. By using the vortex ring model once the liquid jet penetrates through the bubble a vortex ring will insert to the toroidal bubble. The jump of the potential φ_* across the contact point at the time of jet impact is equal to the circulation of the vortex ring as follows:

$$\Gamma_* = \oint_C \nabla_* \varphi_* \cdot d\boldsymbol{r} = \varphi_{N*} - \varphi_{S*}, \tag{5.8}$$

where φ_{S*} and φ_{N*} are potentials at the impact point. The assumption is the liquid jet impact on a single point on the bubble surface. Here we assume jet impact occurs at a single point.

The potential φ_* is then broke down into two parts as follows:

$$\varphi_* = \varphi_{vr} + \phi\,, \tag{5.9}$$

where φ_{vr} is the potential of the vortex ring, which can be got by using the Biot-Savart law Wang et al. [107, 108]. Since in the flow field the remnant potential ϕ is continuous which can be solved by using the BIM model. By using (5.9) the potential jump due to the jet impact is accounted by the potential of the vortex ring.

The mechanical energy of a bubble system consists of the potential energy and the kinetic energy of the bubble system. The potential energy E_P is given as follows Wang & Manmi [105]

$$E_{P*} = \frac{p_{g0*}V_{0*}}{\kappa - 1}\left(\frac{V_{0*}}{V_*}\right)^{\kappa-1} + \sigma_* A_* + V_*\,, \tag{5.10}$$

where A* is the area of the bubble surface. The reference energy is chose as $R_{max}^3 \Delta p$.

The kinetic energy in the bubble gases is negligible since the density of gases is usually three orders of magnitude smaller than liquids. Wang [102] introduced the local kinetic energy E_{LK} of the liquid flow in the inner asymptotic region Ω_L near the bubble. Ω_L is bounded by the bubble surface S and a large sphere S_∞, with its centre at the centre of the initial bubble surface and with a radius being large compared to the bubble radius and small compared to the wavelength λ of the acoustic wave. The local kinetic energy E_{LK} is given as follows Wang [102]:

$$E_{Lk*} = \frac{1}{2}\int_{\Omega_L} \rho_* \left|\nabla_* \varphi_*\right|^2 dV = \frac{1}{2}\oint_{S+S_\infty} \varphi_* \frac{\partial \varphi_*}{\partial n}\, dS + O\left(\varepsilon^2\right) = \frac{1}{2}\oint_S \varphi_* \varphi_{n*}\, dS + O\left(\varepsilon\right). \tag{5.11}$$

The local energy of a bubble system in a compressible liquid consists of the potential energy E_P and the local kinetic energy E_{LK} as follows:

$$E_{L^*} = E_{P^*} + E_{LK^*} = \frac{p_{g0^*} V_{0^*}}{\kappa - 1}\left(\frac{V_{0^*}}{V_*}\right)^{\kappa-1} + \sigma_* A_* + V_* + \frac{1}{2}\oint_S \varphi_* \varphi_{n^*} dS \,. \tag{5.12}$$

5.2 Validations of numerical model

5.2.1 Comparison with the Keller Miksis equation

Figure 5.2 shows the comparison between the viscous compressible BIM (VCBIM) and the Keller Miksis equation (KME) by simulating a spherical bubble damping in an infinite liquid. The parameters in calculations are $R_m = 6.0$ μm, $\kappa = 1.667$, $\varepsilon = 100$, $p_0 = 101.1$ kPa, $\rho = 1000$ kg/m^3, $p_{a^*} = 0$, $\sigma = 0.073$ N/m and $R_e = 60$. As shown in figure 5.2, the viscous compressible BIM has the good agreement with the Keller Miksis equation during the five cycles of bubble oscillations. Due to the compressible and viscous effects, the bubble undergoes a damped oscillation, with the maximum radius decreasing with time and the minimum radius increases with time. For the microbubble dynamics and inertial collapse bubble, both viscous and compressible effects are essential.

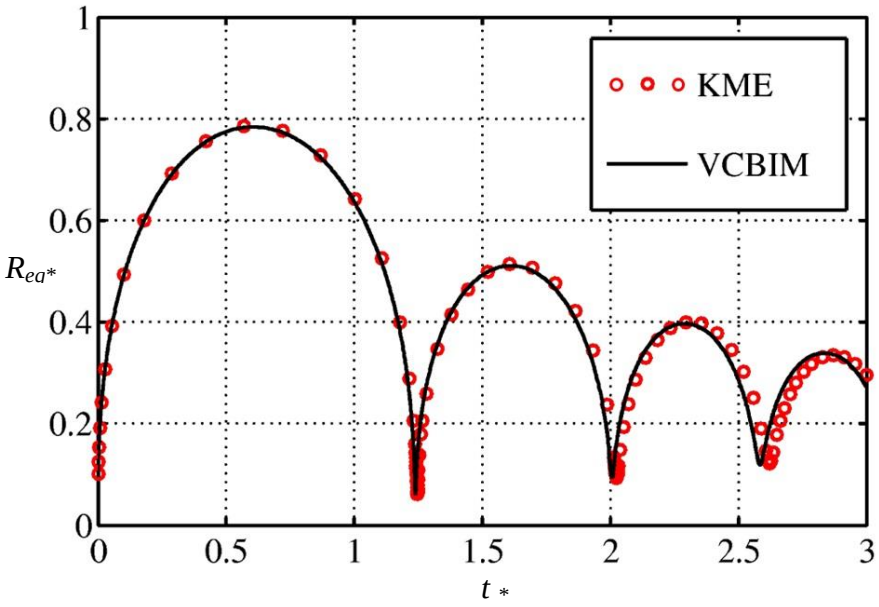

Figure 5.2. Comparison of the CVBIM and Keller-Miksis equation (KME) for the time histories of the radius R_* for a bubble oscillating in an infinite fluid for $R_{max} = 6.0$ μm, $\kappa = 1.667$, $\varepsilon = 100$, $p_0 = 101.1$ kPa, $\rho = 1000$ kg/m^3, $p_{a*} = 0$, $\sigma = 0.073$ N/m and $Re = 60$.

5.2.2 Comparison with the numerical model based on the Navier-Stokes equation

We now compare the computational results of the VCBIM and a numerical model based on the Navier-Stokes equation Minsier et al. [28]. The case considered is for a bubble collapsing near a rigid boundary with the dimensionless standoff distance $\gamma = s/R_m = 0.9$, in oil with viscosity $\mu = 0.05$ kg/(m s). The Reynolds number for the case is $Re = 224$. Figure 5.3 and 5.4 show the bubble shapes in the collapse phase at typical times, which are noted at the upper-left and upper-right corners of each frame for the numerical model based on the Navier-Stock equation and the VCBIM, respectively. The two models agree well in terms of the bubble shape during the whole cycle of oscillation. A large part of the bubble surface is flattened against the rigid boundary at the maximum volume (see frame 1) and is kept in

contact with the boundary subsequently. The top part of the surface collapses down and a jet forms subsequently.

Figure 5.3 shows the bubble shapes in the collapse phase at typical times in water while figure 5.4 shows that in oil. The two models agree well in terms of the bubble shape during the whole cycle of oscillation in both liquids.

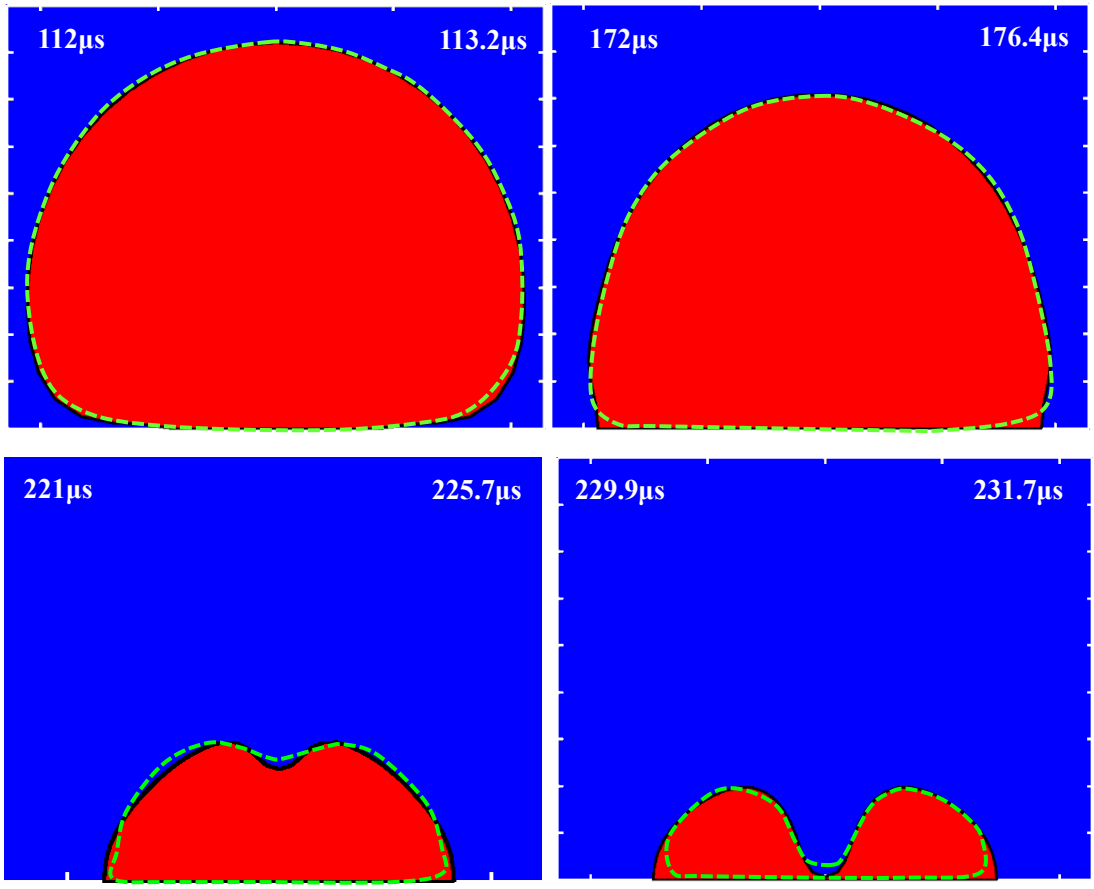

Figure 5.3. The comparison of the bubble shapes near a rigid boundary at $\gamma = 0.6$ calculated using the VCBIM and the numerical model based on the Navier-Stock equation [83] (dash line), in the liquid with viscosity $\mu_{\text{water}} = 0.001$ kg(m·s)$^{-1}$. The rigid boundary is located at the bottoms of the frames. Other parameters used are $R_m = 1.45$ mm, $\kappa = 1.4$, $\varepsilon = 0.013$, $\sigma_* = 0.00051$, $R_*(0) = 0.1$, $R_{t*}(0) = 31.0$ and $p_{g0*} = 127$.

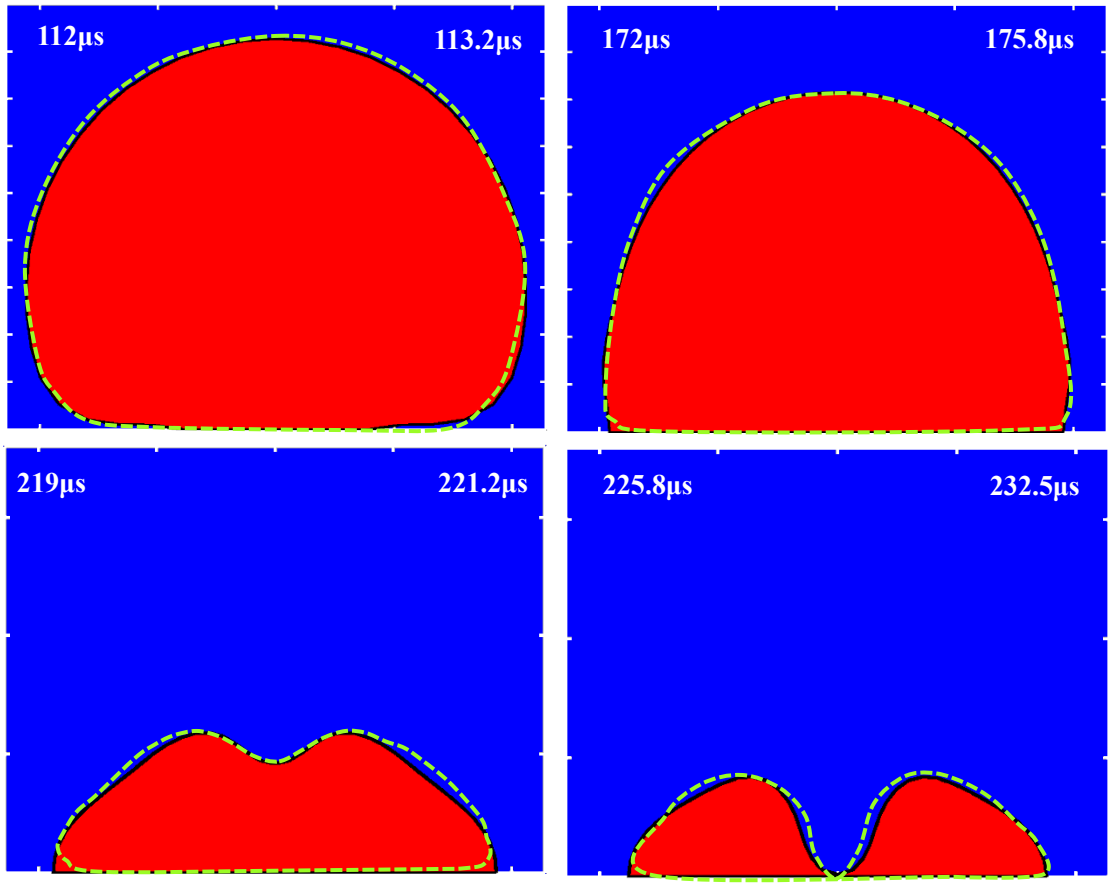

Figure 5.4. The comparison of the bubble shapes near a rigid boundary at $\gamma = 0.6$ calculated using VCBIM and numerical model based on the Navier-Stock equation [83] (dash line), in the liquid with viscosity $\mu_{oil} = 0.05$ kg(m s)$^{-1}$. The rigid boundary is located at the bottoms of the frames. The other remaining parameters the same as in figure 5.3.

5.2.3 Comparison with experiment results

The numerical simulations using the VCBIM are carried out for the dynamics of a laser generated gas bubble at the maximum radius $R_m = 1.45$ mm near a rigid boundary at the dimensionless standoff distance $\gamma = s/R_m = 0.9$, 0.6 and 0.3 respectively, to compare with the experimental data [82]. Other computational parameters are chosen as $\sigma_* = 0.00051$, $\kappa = 1.4$, $R_{t^*}(0) = 31$, $\varepsilon = 0.013$, $p_{g0^*} = 127$, and $R_*(0) = 0.1$. The corresponding dimensional parameters

are p_∞ = 98.1 kPa, $p_v = 2.98$ kPa, $\rho = 1000$ kg·m^{-3}, $\sigma = 0.07$ N·m^{-1}, $R(0) = 1.45$ mm, $R_t(0) = 307$ m·s^{-1} and $p_{g0} = 12.1$ MPa.

Figure 5.5 shows the comparison of the bubble shapes obtained using the VCBIM and the experiments [82], for cavitation gas bubble dynamics near a rigid boundary at $R_m = 1.45$ mm and $\gamma = 0.9$. The experimental and computational results are shown on the left and right columns, respectively. In addition, the computational results are added overlapped with the experimental images for a direct comparison. The computation agrees very well with the experiments during the whole first cycle of oscillation (figure 5.5A). The expansion of the lower part of the bubble surface is retarded by the boundary at $t = 34$ μs. It approximately takes the shape of half of a sphere at its maximum volume at $t = 177$ μs, with the lower part of the bubble surface being flattened by the boundary. The upper part of the bubble surface then collapses down, assuming a cone shape at the middle stage of the collapse phase at $t = 296$ μs. The jet shown in the computational results is not visible in the experimental images due to the opaqueness of the bubble surface. Nevertheless, the outer profiles of the bubble obtained in the computation and experiment agree well. The bubble ring of the computation at the end of collapse at $t = 353$ μs agrees well with the experiment when the bubble reaches its minimum volume.

The computational results for $\gamma = 0.6$ and 0.3 are shown in good agreement with the experimental images in figures 5.6 and 5.7. The results of the VCBIM shown in figures 5.5, 5.6 and 5.7 are very similar to that of the compressible BIM shown in figures 3.7, 3.8 and 3.9.

The viscous effects are insignificant in this case since the Reynolds number associated, $Re = 1450$, is large.

A. First cycle of oscillation

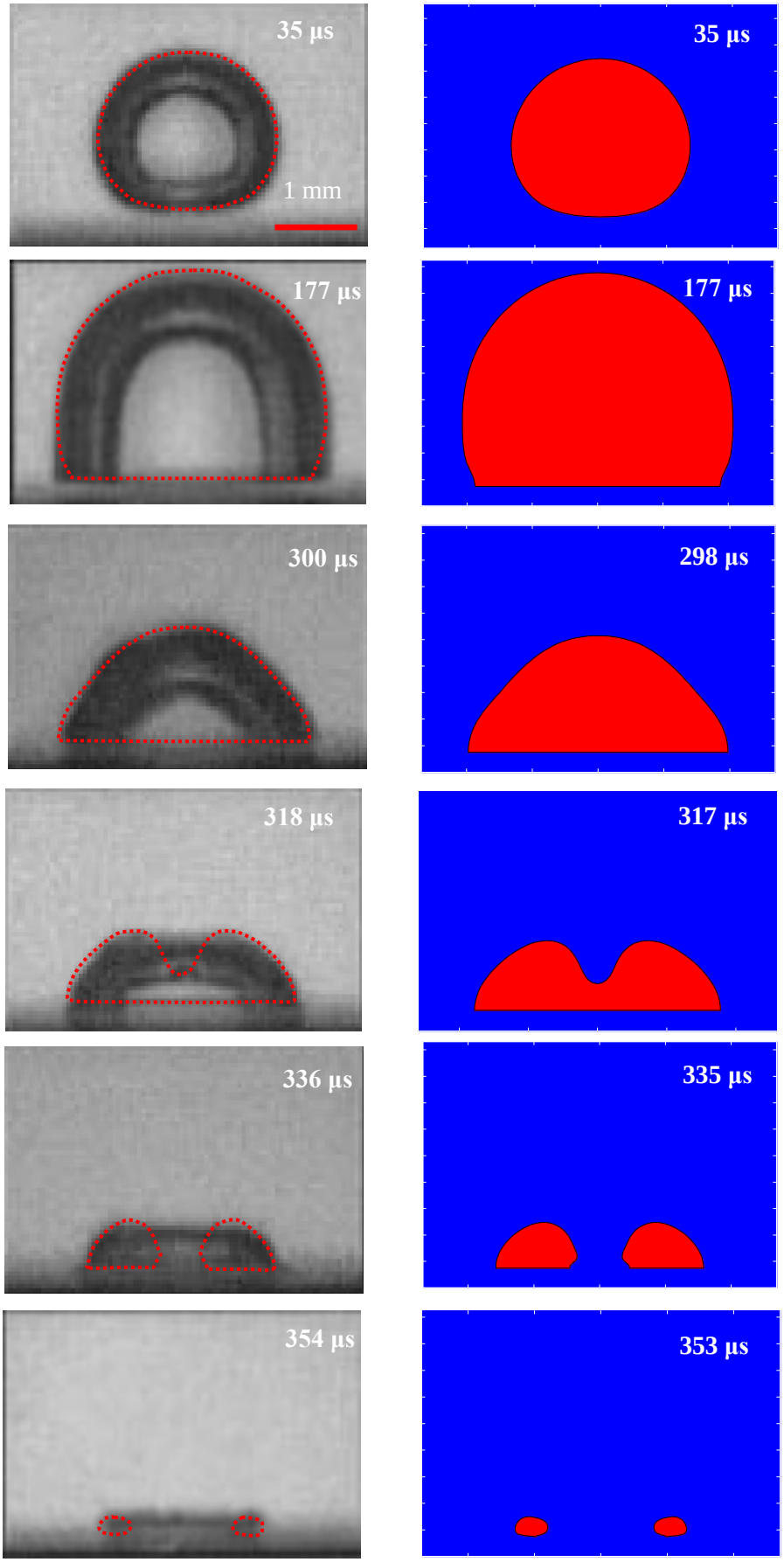

B. Second cycle of oscillation

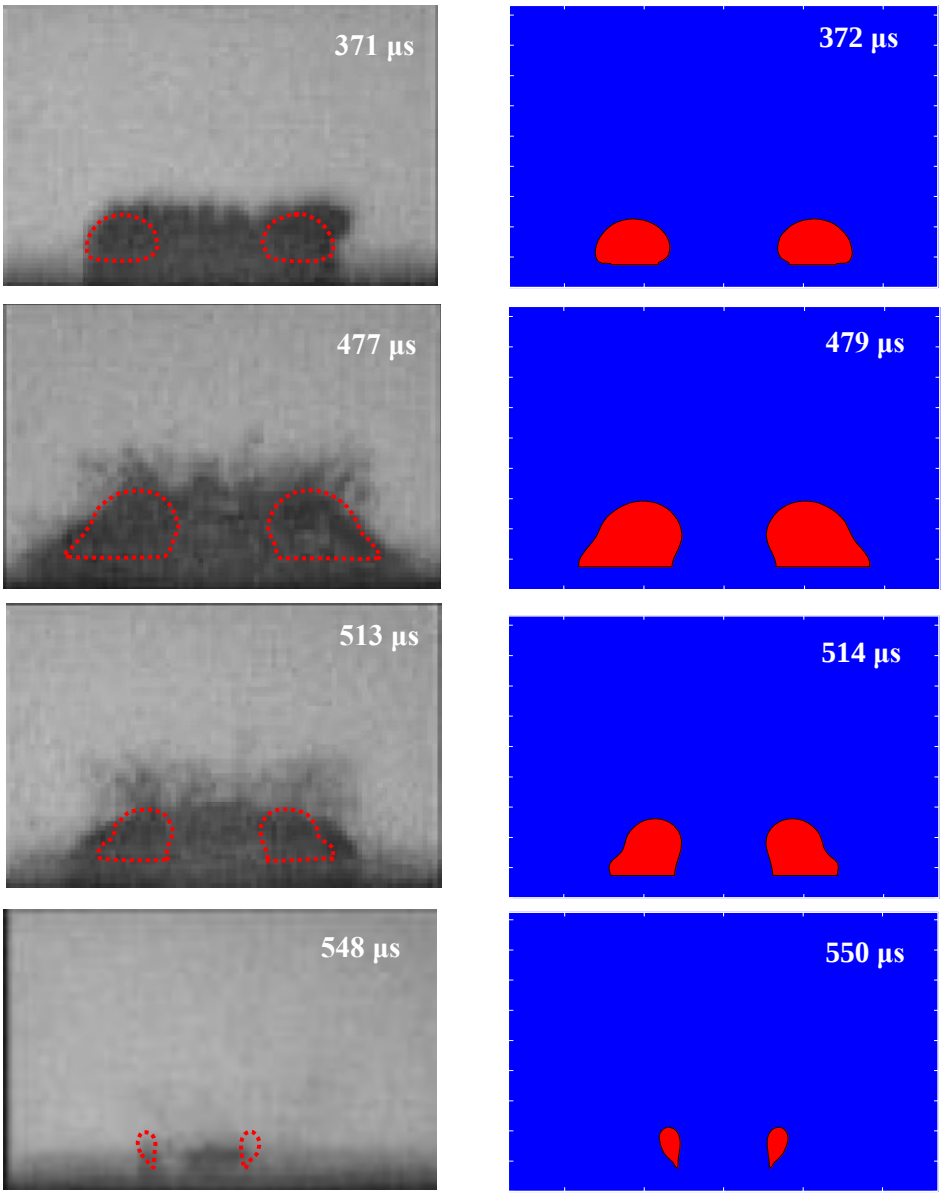

Figure 5.5. Comparison of the viscosity compressible BIM computation (in the right column) with the experiment (in the left column) (reproduced with permission from [82]) for the bubble shapes at various times for a cavitation bubble near a rigid boundary at $R_m = 1.45$ mm and $\gamma = 0.9$, the frame width is 3.9 mm for both the computational and experimental results: (A) during the first-cycle of oscillation and (B) during the second-cycle of oscillation. The motion of a bubble near a rigid boundary characterized by $\gamma = 0.9$, $\kappa = 1.4$, $\varepsilon = 0.013$, $\sigma_* = 0.00051$, $R_*(0) = 0.1$, $R_{t*}(0) = 31.0$ and $p_{g0*} = 127$.

A. First collapse

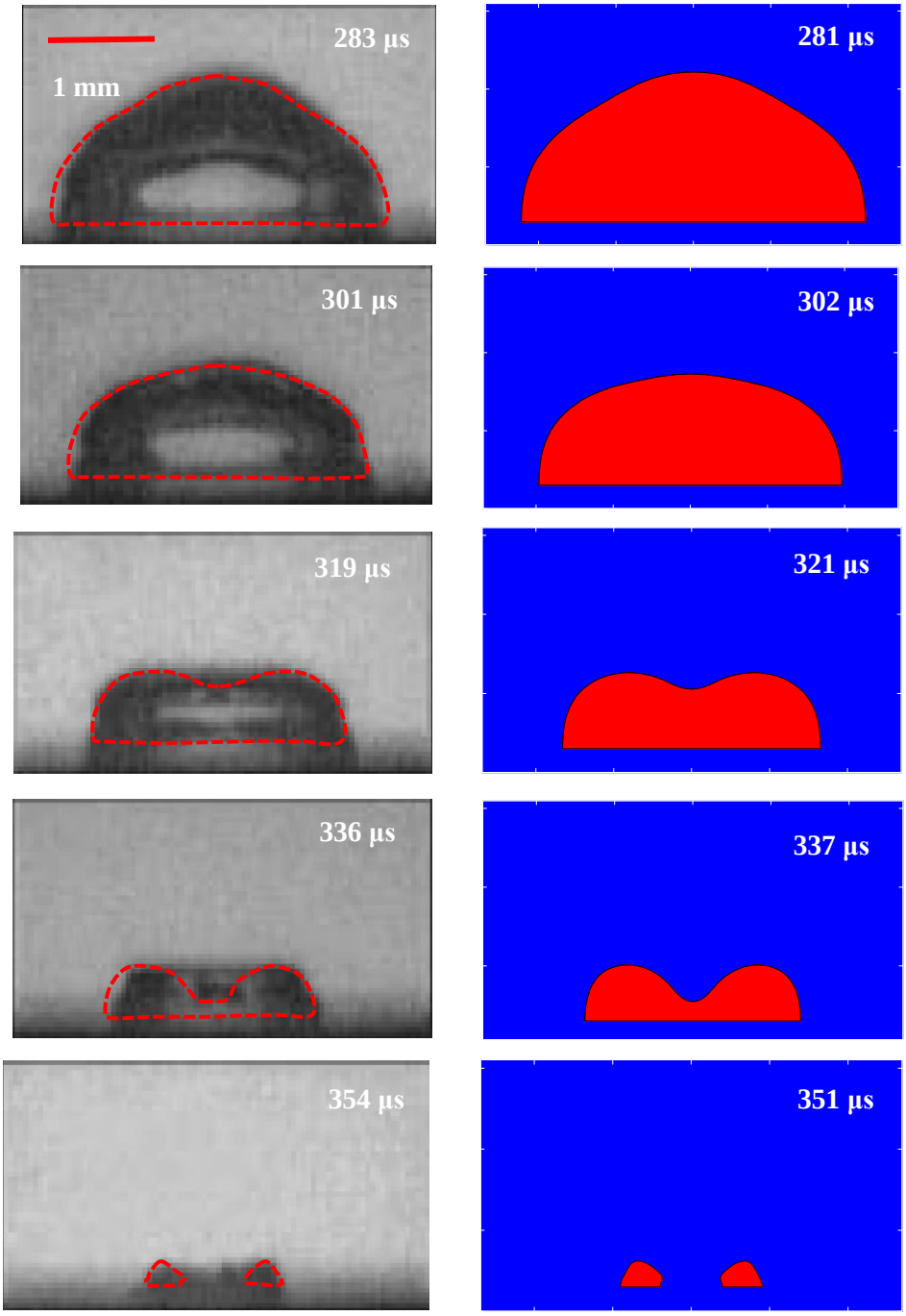

B Second expansion

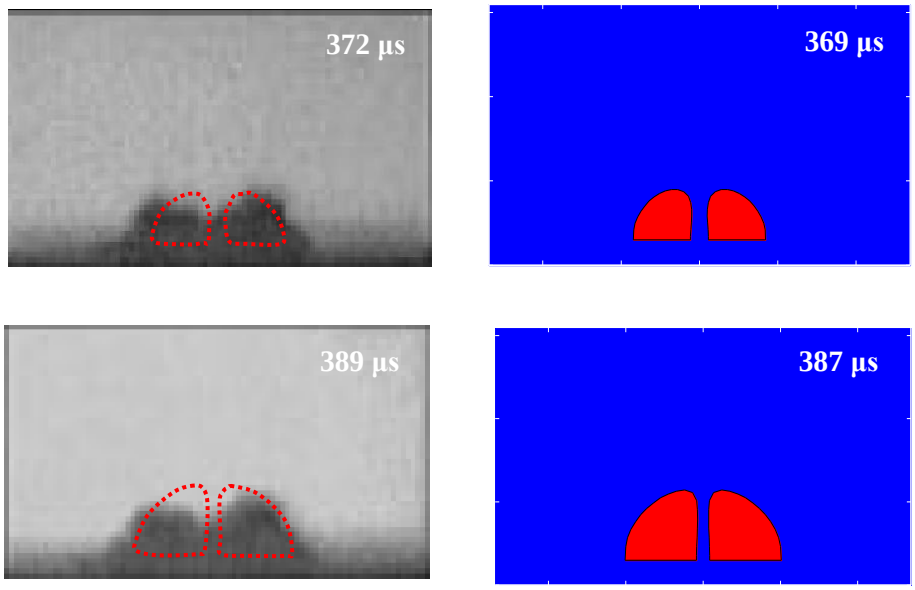

Figure 5.6. Comparison of the viscous compressible BIM computation (in the right column) with the experiment (in the left column) [82] for the bubble shapes at $\gamma = 0.6$: (A) during the first-cycle of oscillation and (B) during the second-cycle of oscillation. The remaining parameters are the same as in figure 5.5.

A. First collapse

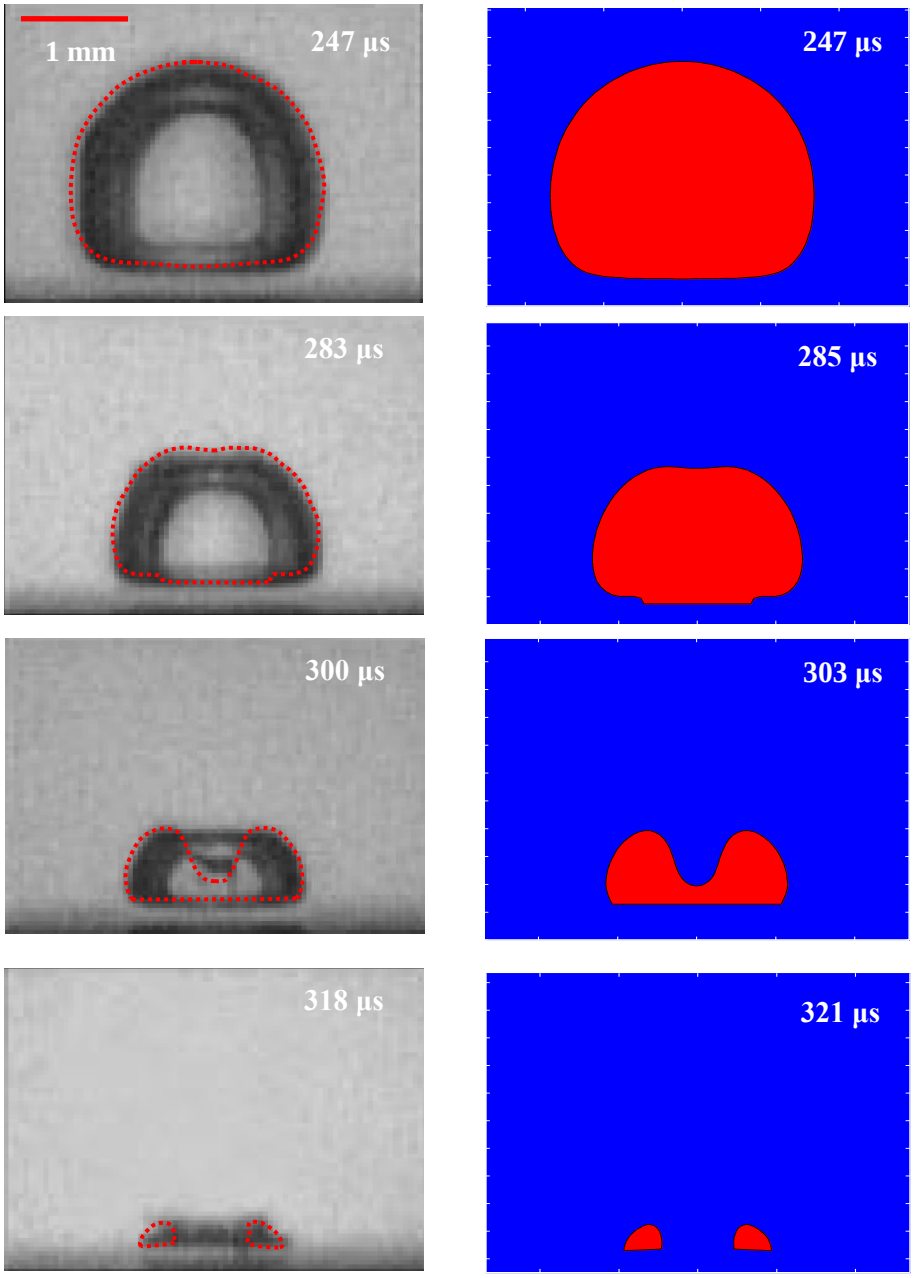

B. Second cycle of oscillation

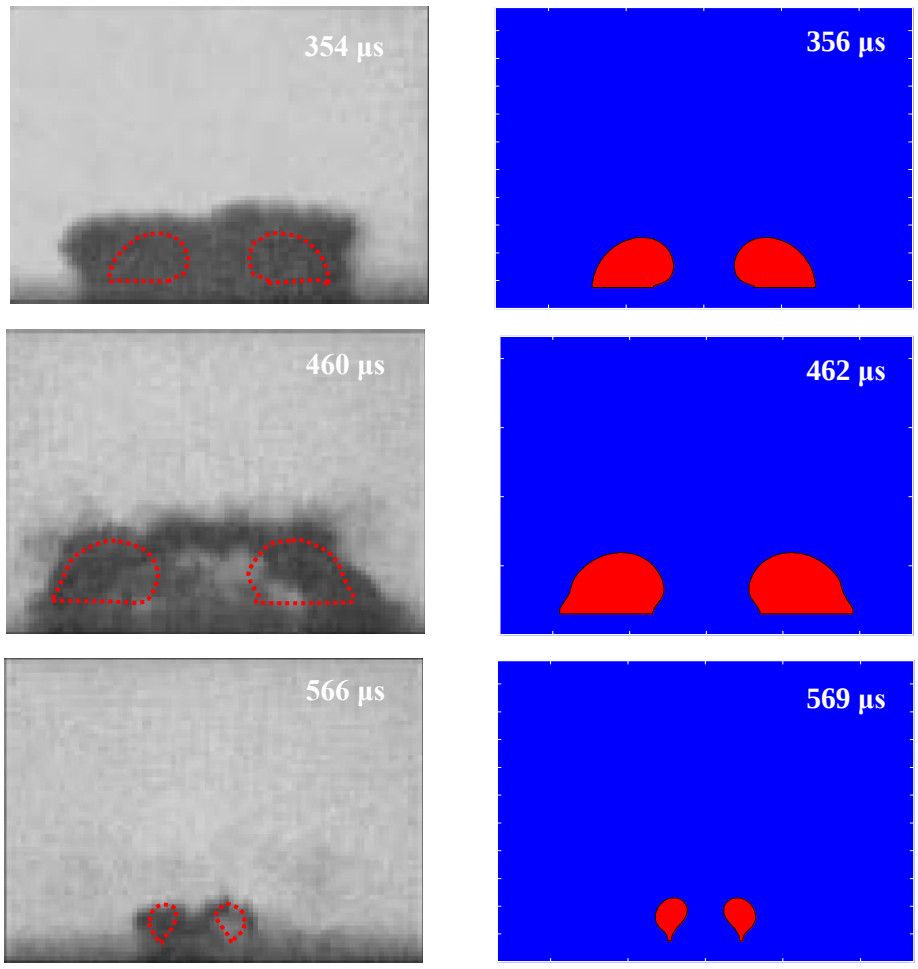

Figure 5.7. Comparison of the viscous compressible BIM computation (in the right column) with the experiment (in the left column) [82] for the bubble shapes at $\gamma = 0.3$: (A) during the first cycle of oscillation and (B) during the second-cycle of oscillation. The remaining parameters are the same as in figure 5.5.

5.3 Numerical analyses

Figure 5.8 shows the bubble shapes for $\gamma = 0.9$ at various typical times. The bubble expands spherically while its lower surface is flattened by the rigid boundary at the end of the expansion (figure 5.8a). As figure 5.8b shows, water cannot penetrate through the rigid boundary so that the lower part of the bubble surface remains on the boundary subsequently during the collapse. During the later stage of collapse, a liquid jet forms on the distal side of the bubble surface directing towards the rigid boundary. Once it penetrates though the bubble at time of $t_* = 2.11$, the jet impacts on the rigid boundary immediately. This is associated with higher damage potential as compared to the damage caused by a bubble jet formed away from the rigid boundary. For the latter case, the jet momentum reduces while it penetrates through the liquid before reaching the rigid boundary.

A bubble ring forms after the jet penetrating through the bubble. The jet pointing to the boundary re-directs radically after it impacting on the boundary, which forces the inner side of the bubble ring moving outwards. Consequently, the jet diameter increases which causing a compression of the bubble volume from inside to outside. Meanwhile, the bubble ring collapses from all sides rapidly except for the bottom. When it reaches its minimum volume at $t_* = 2.24$ (figure 5.8c), the bubble ring in contacting with the rigid boundary reaches the maximum pressure and temperature. This gives rise to another damage potential. In addition, a shock wave is emitted at the minimum bubble volume with high-pressure amplitude [93], it impinges on the rigid boundary once it is emitted and has clear damage potential.

Afterwards, the bubble ring rebounded upwards and outwards along the boundary (figure 5.8d). It then re-collapses from top to bottom and from the external to the internal. The radius

of the bubble ring at the end of re-collapse is smaller than that at the end of collapse. The bubble keeps in touch with the boundary during the second cycle of oscillation.

Figures 5.9 and 5.10 show the bubble shapes at various times for $\gamma = 0.6$ and 0.3, respectively. As expected, the lower part of the bubble surface starts to be on the boundary earlier than that for $\gamma = 0.9$ (as shown in figure 5.9a and 5.10a respectively), in the middle and early stage of expansion respectively. In analogous to the case for $\gamma = 0.9$, figures 5.9b and 5.10b show that the lower part of the bubble surface keeps in contact with the boundary afterwards and the liquid jet clashes on the boundary immediately after it penetrates through the bubble. Comparing figures 5.8b, 5.9b and 5.10b, it comes to a conclusion that the larger the standoff distance is, the sharper the jet becomes.

After impacting on the rigid boundary, the liquid jet again redirects horizontally and pushes away the bubble from the inner side. The bubble ring then collapses from all sides except for the part in contact with the boundary (figures 5.9c and 5.10c). The bubble ring takes its minimum volume, maximum pressure and maximum temperature at $t_* = 2.29$ and $t_* = 2.30$ for $\gamma = 0.6$, 0.3 respectively, when a shockwave is emitted and impacts on the boundary.

As figures, 5.9d, e and 5.10d, e present, the bubble ring further rebounds and recollapses, predominately from the top and external parts of the bubble surface. The radius of the bubble ring at the end of the second cycle of oscillation is again smaller than at the end of the first

cycle. The maximum volume of the bubble during the second cycle increases as the bubble is initiated closer to the boundary.

Now, how the bubble changed as a whole should be taken into consideration. Figure 5.10a presents how the time histories of the equivalent bubble radius $R_{eq^*} = \sqrt[3]{\frac{3}{4\pi}V_*}$ be different for $\gamma = 0.9$, 0.6 and 0.3, respectively. The maximum radius reduces significantly from the first to the second cycles of oscillation, so does the oscillation period. The maximum bubble radius at the second-cycle are decreased to 0.56 R_m, 0.58 R_m, 0.62R_m when $\gamma = 0.9$, 0.6 and 0.3, respectively, increasing as the bubble initiated closer to the boundary. By comparing figures 5.5a and 3.6a the maximum bubble radius in the second cycle of oscillation further reduced about 2%, 1% and 2% due to the viscous effects, with the bubble system for $\gamma = 0.9$, 0.6 and 0.3, respectively.

Figure 5.11b shows the time histories of the local energy E_L of the bubble system for the three cases. In the beginning of the first and second cycle of oscillation, when shock waves are emitted, the local energy reduces significantly and rapidly. While for the rest of time, it is almost a constant value, when the compressible effects are approximately negligible. After the shockwave is emitted at the inception of the bubble, about 56%, 58% and 62% of the initial energy remains with the bubble system for $\gamma = 0.9$, 0.6 and 0.3, respectively. After the shockwave is emitted at the end of the collapse, only around 13%, 15% and 18% of the initial energy is left with the bubble system for $\gamma = 0.9$, 0.6 and 0.3, respectively. By comparing figure 5.11b and 3.6c at the end of first collapsing, about 2%, 1% and 2% of more energy lost due to the viscous effects, with the bubble system for $\gamma = 0.9$, 0.6 and 0.3, respectively.

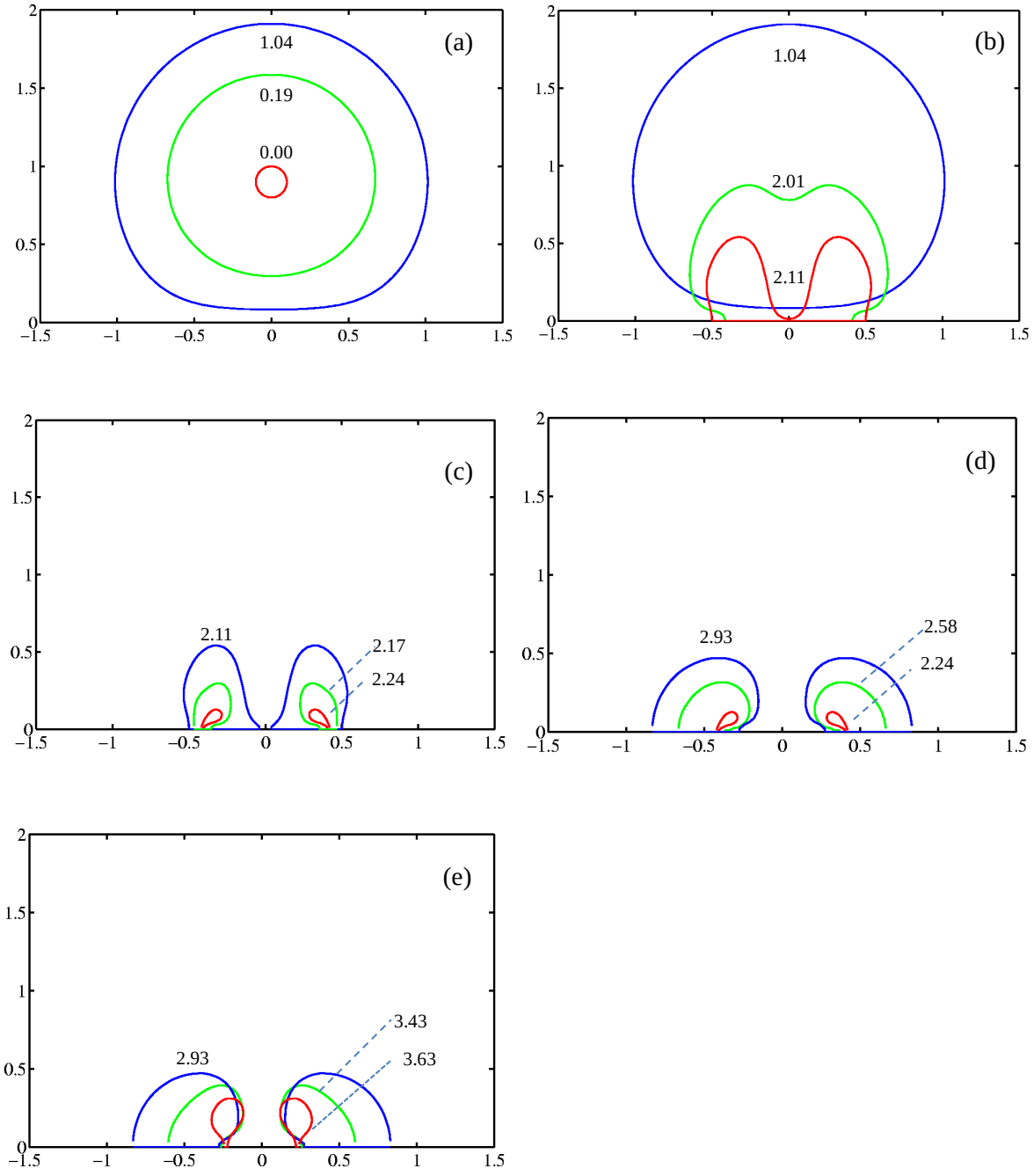

Figure 5.8. The motion of a bubble near a rigid boundary characterized by $R_*(0) = 0.1$, $\gamma = 0.9$, $\kappa = 1.4$, $\sigma_* = 0.00051$, $\varepsilon = 0.013$, $R_{t*}(0) = 31.0$, $Re = 1450$ and $p_{g0*} = 127$. The bubble shapes are in (a) the first expansion phase, (b-c) the first collapsing phase in between singly- and doubly-connected form respectively, (d) during the second expansion phase, and (e) the second collapse phase.

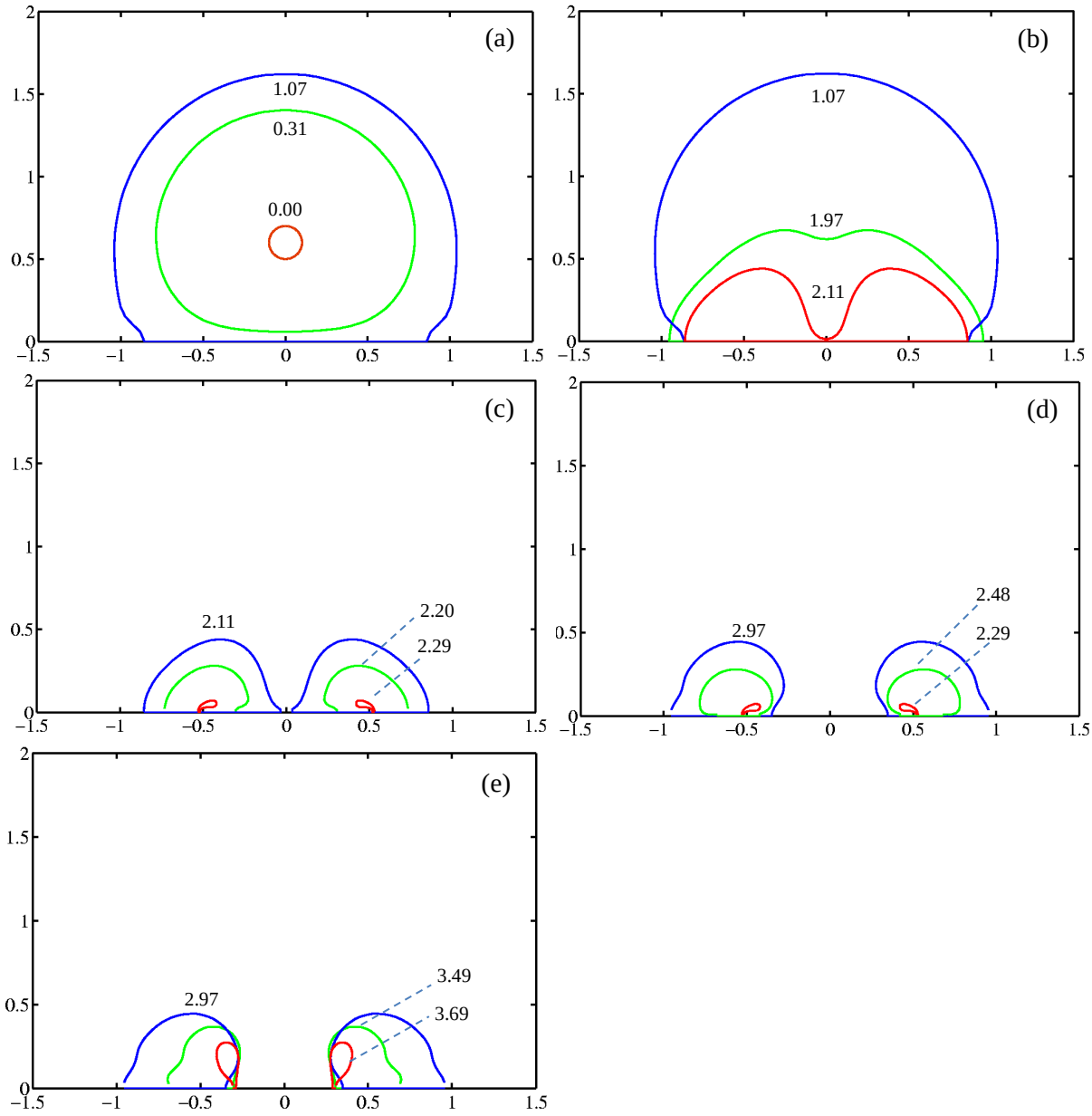

Figure 5.9. Bubble dynamics near a rigid boundary for $\gamma = 0.6$ and the parameters are the same as in figure 5.8. The bubble shapes are during (a) the 1st expansion phase, (b-c) the 1st bubble collapsing phase in a singly- and doubly-connected form respectively, (d) the 2nd expansion phase and (e) the 2nd collapse phase.

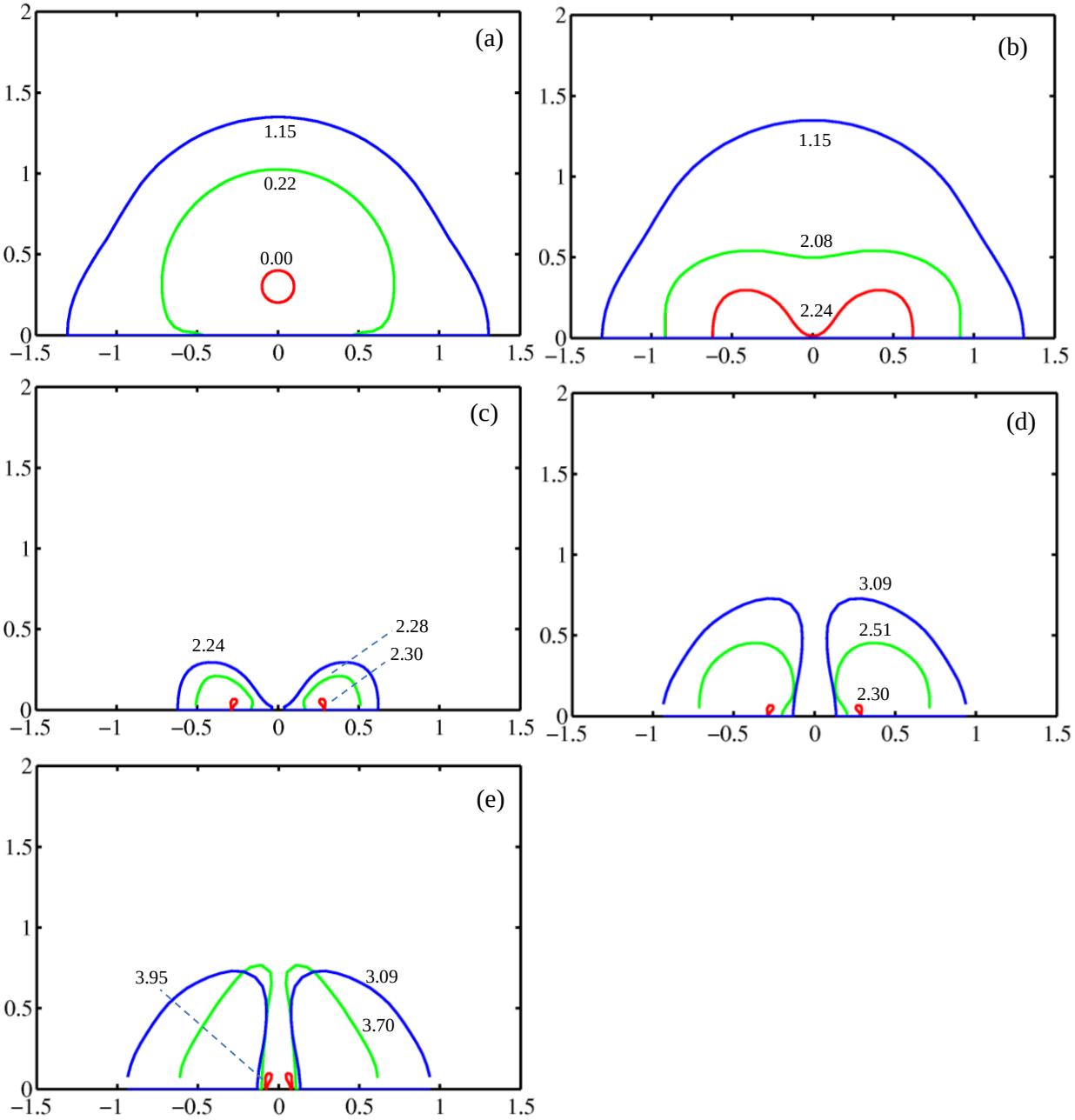

Figure 5.10. Bubble dynamics near a solid boundary at $\gamma = 0.3$, with the remaining parameters the same as in figure 5.8. The bubble shapes are during (a) the 1st expansion phase, (b-c) the 1st for collapsing phase in a singly- and doubly-connected form respectively, (d) the 2nd expansion phase and (e) the 2nd collapse phase.

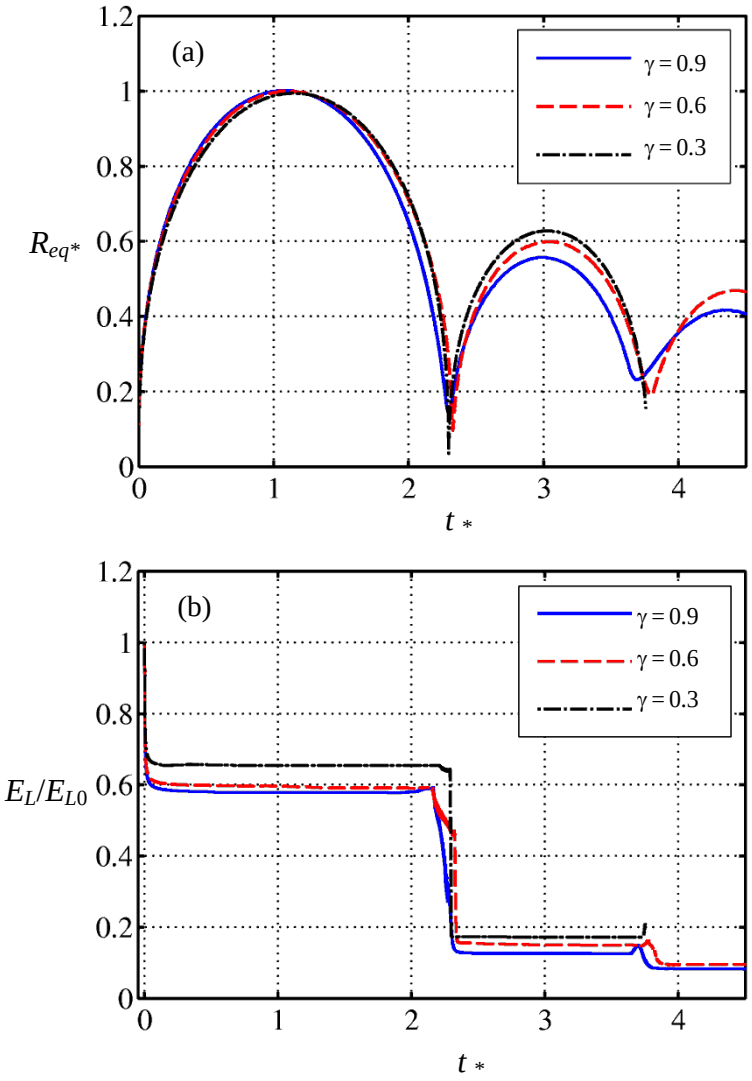

Figure 5.11. Comparison for time histories of (a) the equivalent bubble radius R_{eq*} and (b) local energy E_L/E_{L0} of the bubble system for a cavitation bubble near a rigid boundary for γ= 0.9, 0.6 and 0.3. Other parameters used are R_m = 1.45 mm, κ = 1.4, ε = 0.013, σ_* = 0.00051, $R_*(0)$ = 0.1, $R_{t*}(0)$ = 31.0 and p_{g0*} = 127.

There are small differences between the results obtained from the inviscid and viscous compressible BIM, i.e. ICBIM and VCBIM. Figure 5.12 illustrates the comparison of the results obtained from the ICBIM and VCBIM for the radius history and energy history. As

shown in figure 5.12a, the maximum radius during the second cycle for the VCBIM is slightly below that for the ICBIM, which is because a small amount of energy has been lost due to viscosity effects.

In figure 5.12b, the energy history of the ICBIM is almost the same as that of the VCBIM during the first cycle of bubble oscillation. However, during the second cycle the energy of the VCBIM is slightly below the ICBIM. The differences of the dimensionless energy of the two models are 0.01, 0.025 and 0.035 during the first, second and third cycle, respectively. This is because the longer time the bubble oscillate the more energy of the bubble system is lost due to viscous effects.

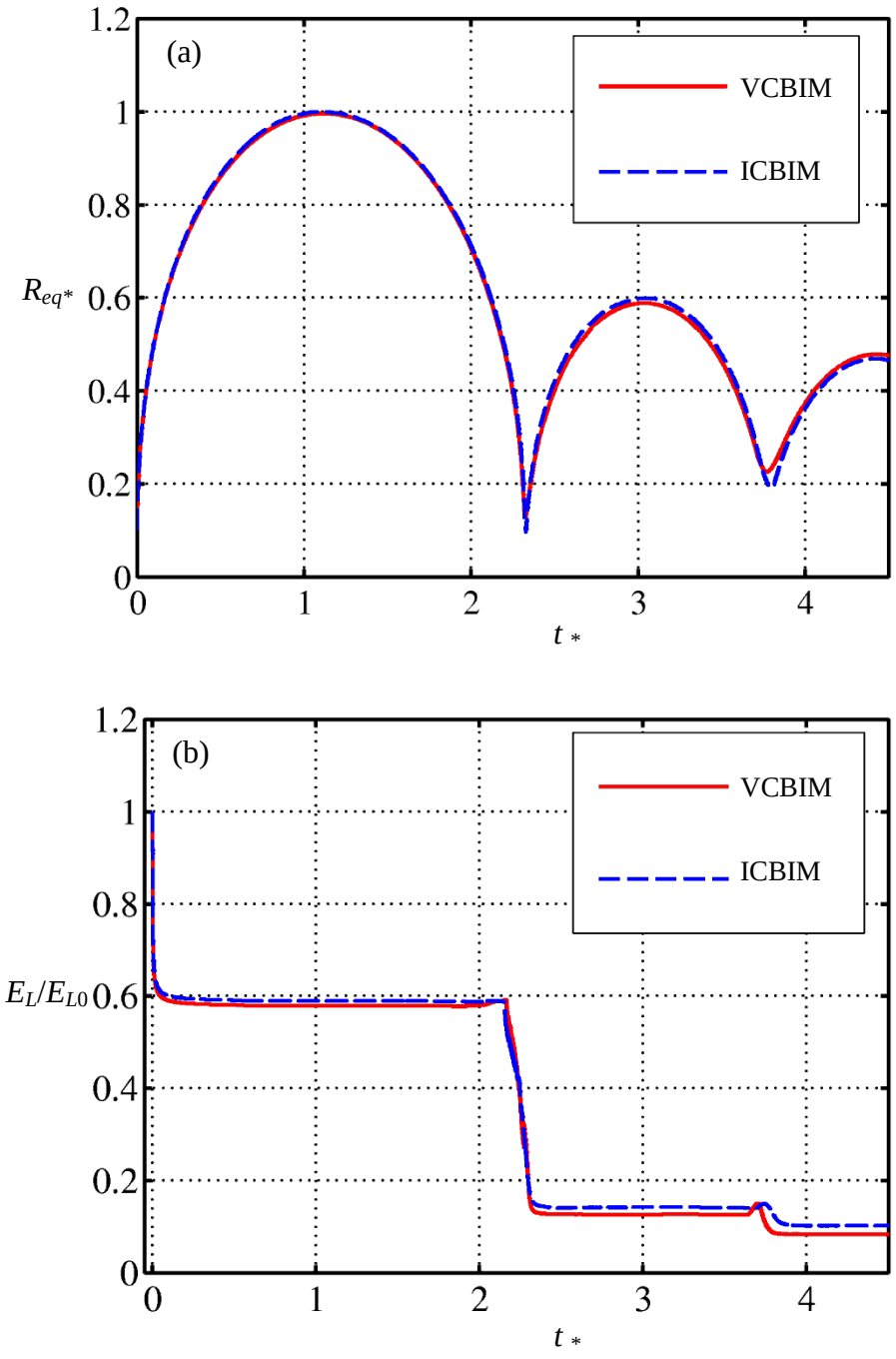

Figure 5.12. Comparison of the ICBIM and the VCBIM for time histories of (a) the equivalent bubble radius R_{eq*} and (b) local energy E_L/E_{L0} of the bubble system for a cavitation bubble near a rigid boundary for $R_m = 1.45$ mm, $\gamma = 0.6$, $\kappa = 1.4$, $\varepsilon = 0.013$, $\sigma_* = 0.00051$, $R_*(0) = 0.1$, $R_{t*}(0) = 31.0$ and $p_{g0*} = 127$.

In the above cases, the Reynolds number, $Re = 1450$, is large and viscous effects are negligible. To consider the viscous effects, we repeat the case in figure 5.8 with a smaller Reynolds number, $Re = 60$ (corresponding to a bubble for $R_m = 6.0$ μm). Figure 5.13 shows the bubble shapes at various times by using the VCBIM. The bubble dynamics for $Re = 60$ are similar to that for $Re = 1450$ as shown in figure 5.8. The bubble first expands spherically before it being flattened by the rigid boundary (figure 5.13a). The bubble surface kept on the boundary when the bubble subsequently collapses. At the end of the collapse, a liquid jet penetrated the bubble and impacted on the rigid boundary. It pushed the bubble ring moving outwards. Then the jet expanded on the horizontally. Afterwards, the bubble expanded again as a bubble ring and then re-collapsed.

However, the following viscous effects are observed. The dimensionless oscillation period decreases significantly for the smaller Reynolds number at $\gamma = 0.6$, jet impact happening at $t_* =$ 1.55, 2.11, reaching the minimum volume at $t_* = 1.69$, 2.29, and the second minimum volume at $t_* = 2.59$, 3.69, for $Re = 60$, 1450, respectively.

Figure 5.13b and 5.9b show while collapsing the bubble ring radius is narrower than the bubble with radius $R_m = 1.45$ mm. By comparing figure 5.13e with 5.9e, when it is reaching the minimum radius the bubble radius is larger than the bubble with $R_m = 1.45$ mm and the liquid jet is narrower than the bubble with $R_m = 1.45$ mm. Because of the large viscosity effects, the bubble with $R_m = 6.0$ μm lost more energy during first oscillation, during the second collapsing the minimum bubble volume is larger than the bubble with $R_m = 1.45$ mm.

Figure 5.14 and 5.8 illustrate the bubble shapes for a bubble oscillation near a rigid boundary when $\gamma = 0.9$ jet impact on the rigid boundary at $t_* = 1.67, 2.11$, attaining the minimum volume at $t_* = 1.69, 2.24$, and collapsing the second minimum volume at $t_* = 2.21, 3.63$, for $Re = 60, 1450$, respectively.

Figure 5.13b and 5.14b illustrate that the bubble with $\gamma = 0.9$ collapses longer with much wider jet than the bubble with $\gamma = 0.6$ during the first collapsing. Figure 5.13c and 5.14c show the bubble reaching the minimum volume at the same time for both two cases. By comparing figure 5.13e with 5.14e, the bubble with $\gamma = 0.9$ reaches it second minimum volume earlier than the case when $\gamma = 0.6$. Since the bubble with $\gamma = 0.9$ has a longer time to expand and collapse, the bubble collapses strongly in the first cycle of oscillation than the bubble with $\gamma = 0.6$. The bubble with $\gamma = 0.9$ loses more energy after the first collapse subsequently has weaker expansion and collapsing during the second cycle of oscillation.

As shown in figure 5.15 the equivalent bubble radius for $\gamma = 0.6$ and 0.9, the bubble $R_m = 6.0$ μm (blue dash line) always has less radius than the bubble with $R_m = 1.45$ mm (red solid line) in the whole two cycles of oscillation. The bubble oscillation period with $R_m = 6.0$ μm is much shorter than the bubble with $R_m = 1.45$ mm. The reason is that the viscous effects is not negligible for the smaller bubble. Due to the high viscosity, the bubble with $R_m = 6.0$ μm expands slower and weaker than the bubble with $R_m = 1.45$ mm.

Figure 5.16 illustrates the energy history of the bubble when standoff distance $\gamma = 0.6$ and 0.9. For the bubble, $R_m = 6.0$ μm (blue dash line) the continuous energy decreases during the first cycle of the oscillation, and at the end of the first collapsing reduced significantly. During the

second cycle of the oscillation, the energy history moves up and down a little bit for $\gamma = 0.6$, at the end of the second collapsing the small amount of energy released from the bubble. For the bubble with $R_m = 1.45$ mm (solid red line) the energy history almost stays the same during the first cycle of the oscillation. At the end of the first collapsing due to the liquid jet penetrates through the bubble significantly amounts of energy released from the bubble. During the second cycle of oscillation, the energy almost keeps constant except at the end of second of collapsing significantly go down a little bit.

For the standoff distance $\gamma = 0.9$ the bubble $R_m = 6.0$ μm (blue dash line) energy history almost maintains the same but slowly go down during the first cycle of oscillation. After the jet penetrates the bubble the energy history, remain coherent for the rest of the time. Because of the large standoff distanceγ, the first collapsing is strong, and during the second cycle of oscillation, the rest of the energy remained in the bubble may form a very weak jet. For the bubble with $R_m = 1.45$ mm (solid red line) the energy history behaves similarly to $\gamma = 0.6$.

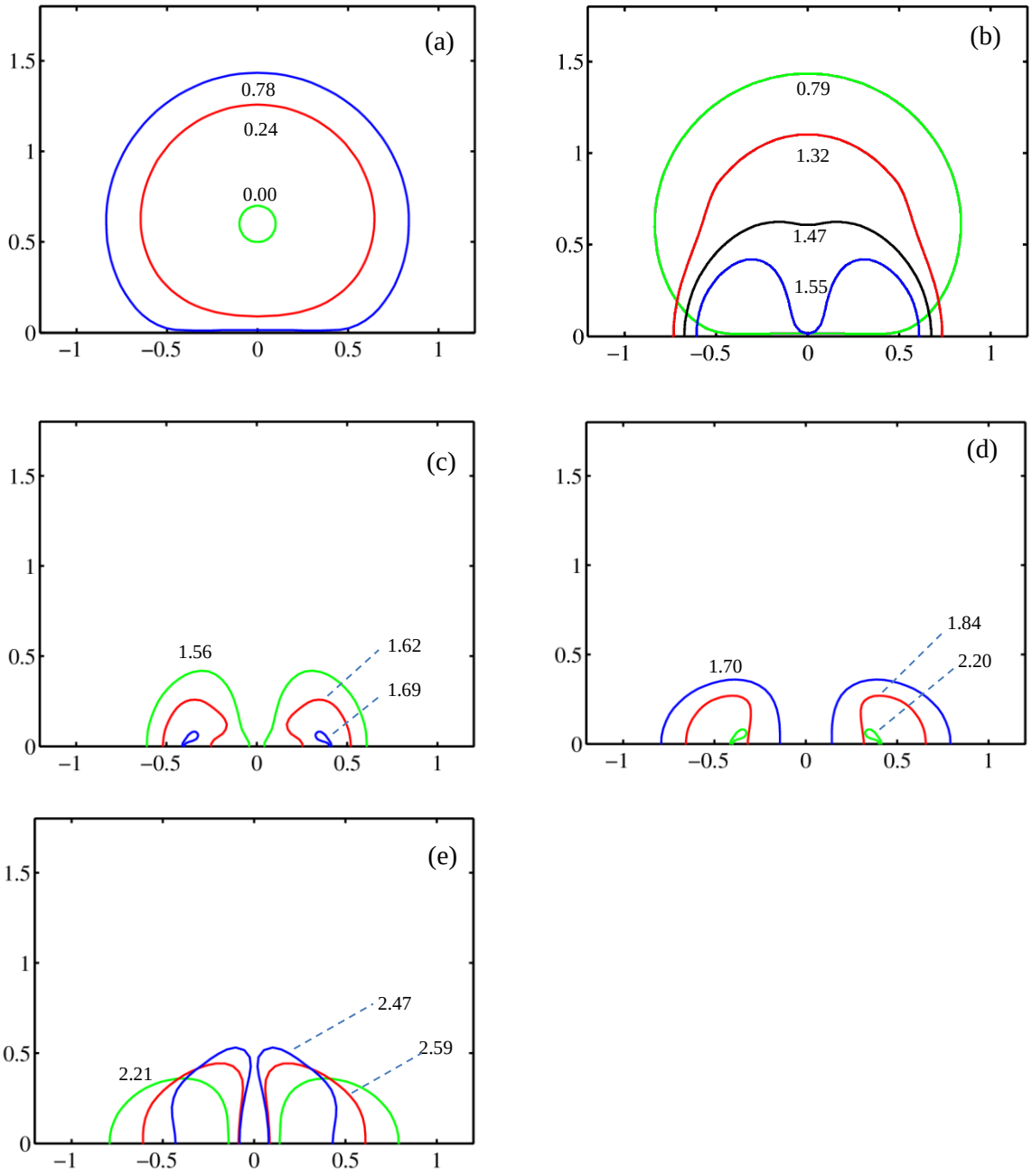

Figure 5.13. Bubble dynamics near a solid boundary at $\gamma = 0.6$, with the remaining parameters $R_m = 6.0$ μm, $\kappa = 1.4$, $\varepsilon = 0.013$, $\sigma_* = 0.00051$, $R_*(0) = 0.1$, $R_{t^*}(0) = 31.0$, $\rho = 1000$ kg/m^3, $p_{g0^*} = 127$, and $Re = 60$. The figures show the bubble shapes during (a) the 1st expansion phase, (b-c) the 1st bubble collapsing phase in a singly- and doubly-connected form respectively, (d) the 2nd expansion phase and (e) the 2nd collapse phase.

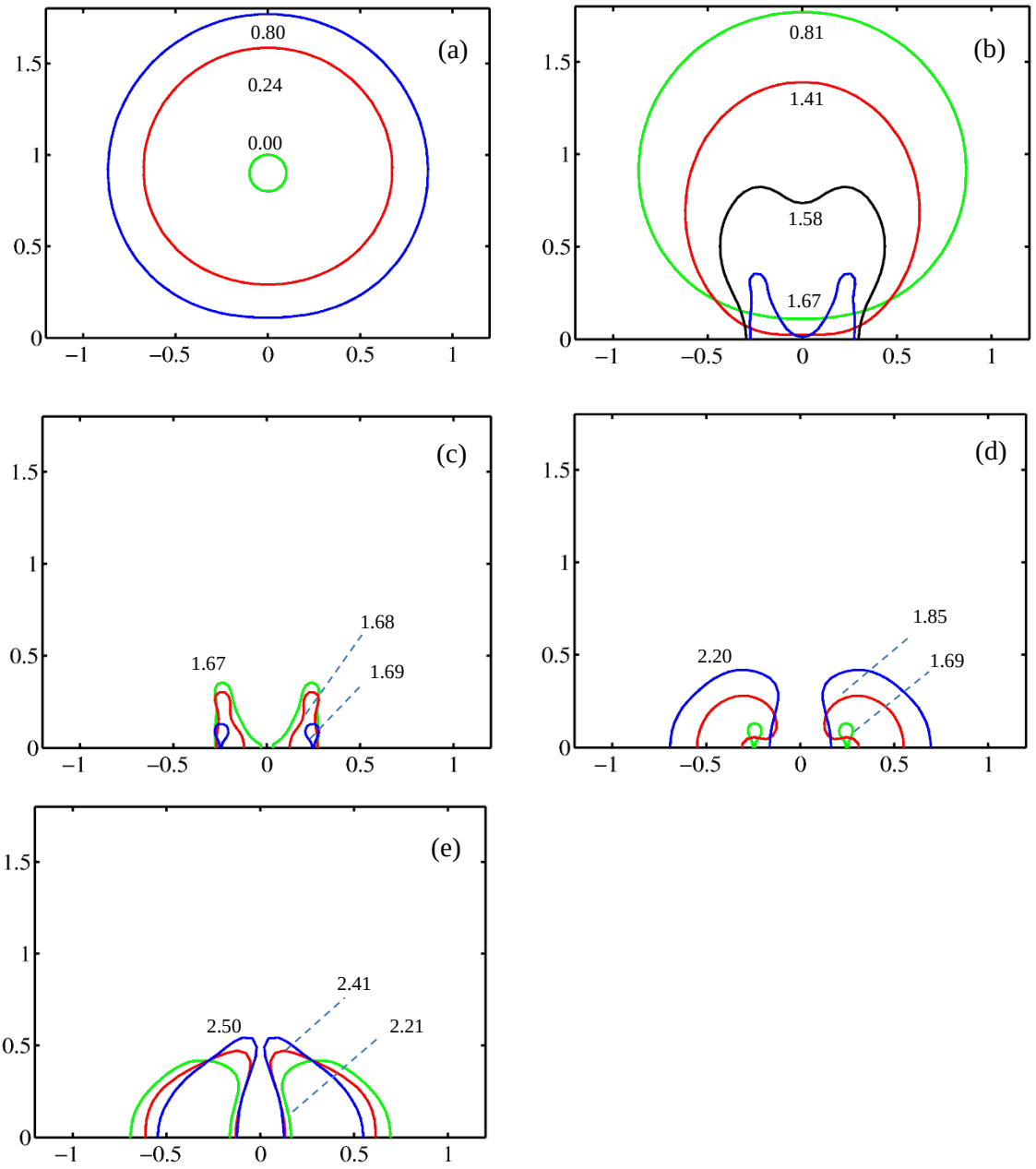

Figure 5.14. Bubble dynamics near a solid boundary at $\gamma = 0.9$, with the remaining parameters same as figure 5.13. The figures show the bubble shapes during (a) the 1st expansion phase, (b-c) the 1st bubble collapsing phase in a singly- and doubly-connected form respectively, (d) the 2nd expansion phase and (e) the 2nd collapse phase.

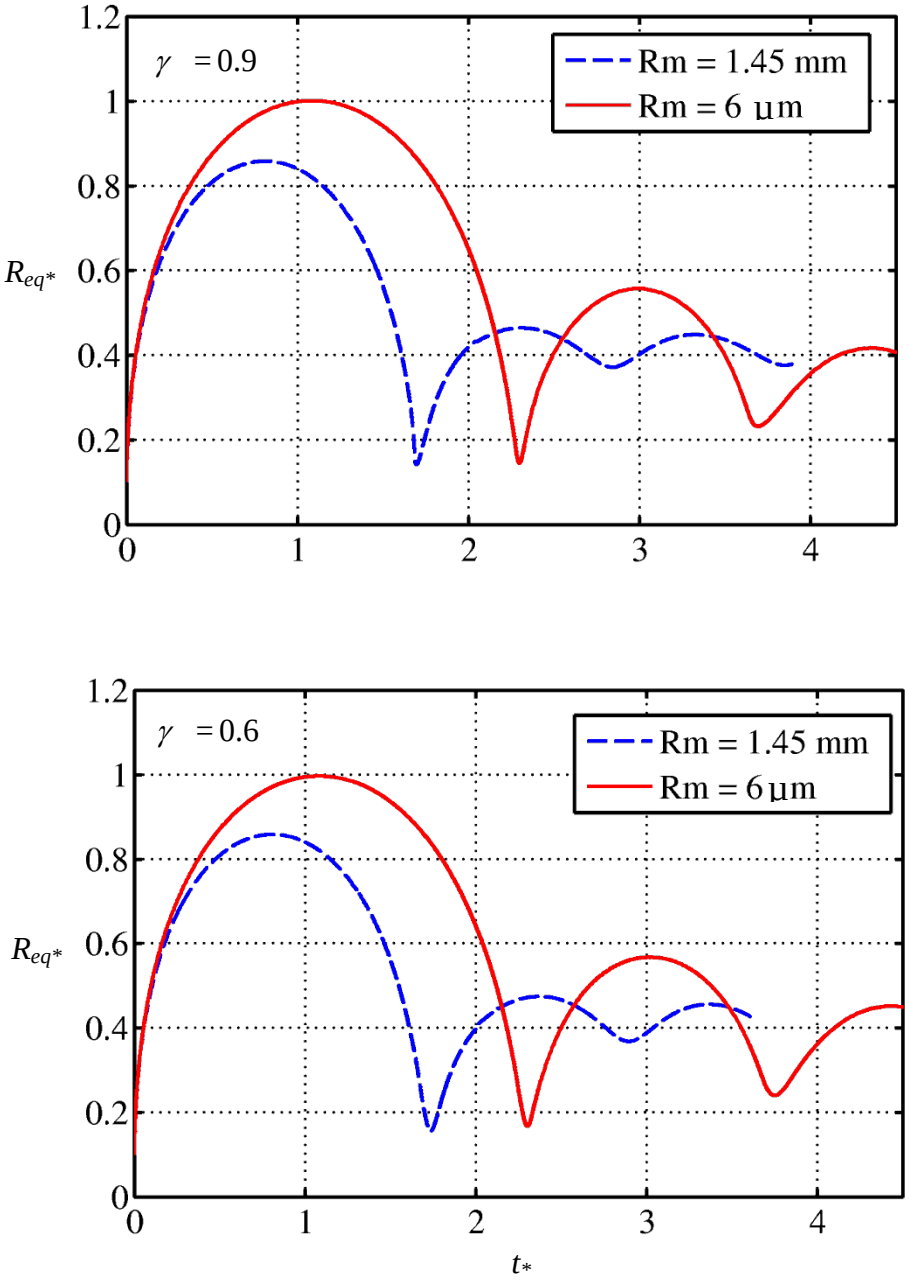

Figure 5.15. Comparison of the ICBIM and the VCBIM for time histories of the equivalent bubble radius R_{eq*} for a cavitation bubble near a rigid boundary for $\gamma = 0.6$ and $\gamma = 0.9$. The rest of the parameters are $R_m = 6$ µm, $\kappa = 1.4$, $\varepsilon = 0.013$, $\sigma_* = 0.00051$, $R_*(0) = 0.1$, $R_{t*}(0) = 31.0$, $Re = 60$ and $p_{g0*} = 127$.

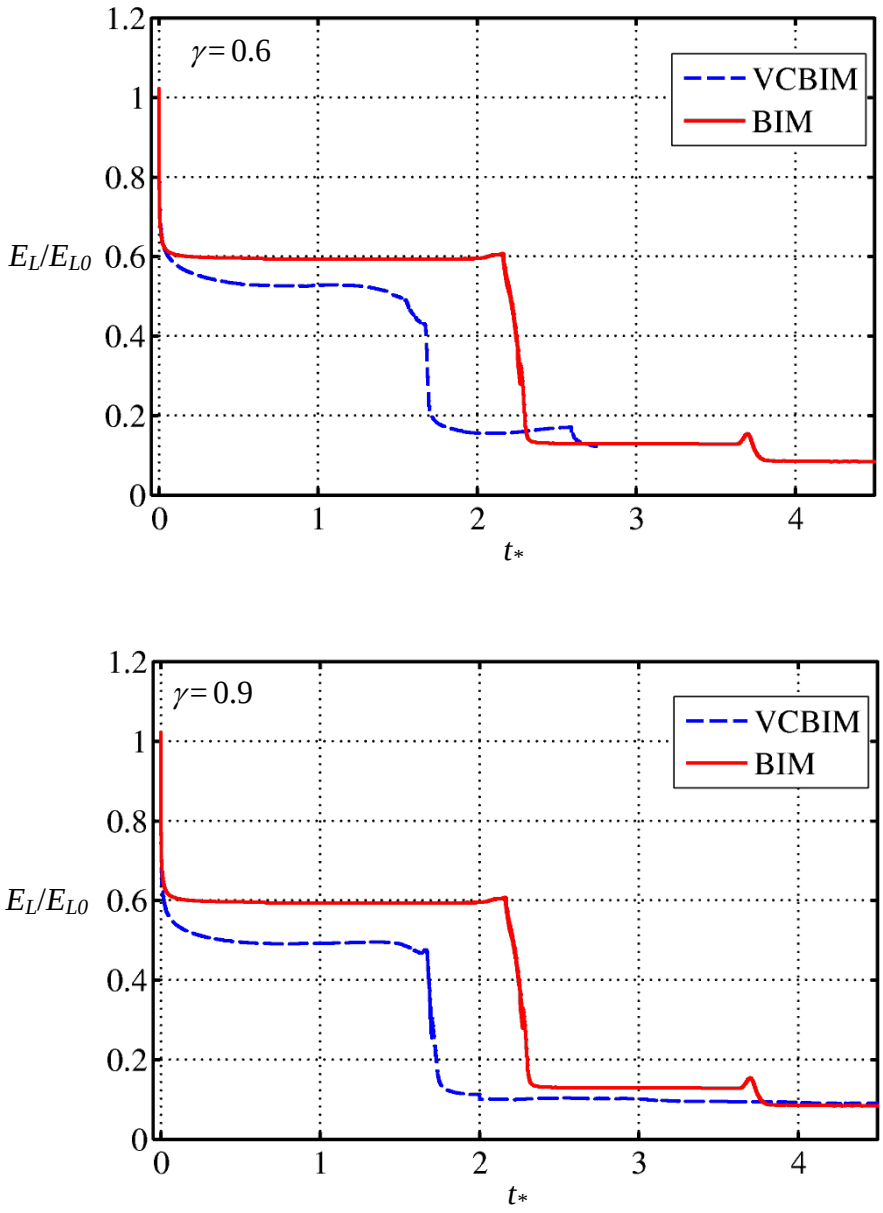

Figure 5.16. Comparison of the ICBIM and the VCBIM for time histories of local energy E_L/E_{L0} of the bubble system for a cavitation bubble near a rigid boundary for $\gamma = 0.6$ and $\gamma = 0.9$. The rest of parameters are $R_m = 6$ μm, $\gamma = 0.6$, $\kappa = 1.4$, $\varepsilon = 0.013$, $\sigma_* = 0.00051$, $R_*(0) = 0.1$, $Re = 60$, $R_{t*}(0) = 31.0$ and $p_{g0*} = 127$.

Chapter 6

MICROBUBBLE DYNAMICS IN AN ULTRASOUND FIELD

In this chapter, we study microbubble dynamics subject to an ultrasound acoustic wave. This phenomenon has important applications in sonochemistry, ultrasound cleaning and bioscience. We first describe the Keller-Miksis equation for spherical bubble dynamics subject to ultrasound. We then describe the physical and mathematical model for the dynamics of nonspherical microbubble dynamics, using the viscous potential flow theory, weakly compressible theory and BIM. The viscous compressible BIM is shown in good agreement with the Keller-Miksis equation for spherical bubble dynamics. The viscous compressible BIM is also shown in good agreement with the experiments for dynamics of non-spherical bubble subject to ultrasound.

6. 1 Spherical bubble theory

Rayleigh developed a theoretical model to describe the spherical oscillation of gas bubbles [87]. A bubble in a liquid is an oscillatory system. For a spherical bubble oscillation, the bubble size and the shape are defined as the bubble radius R and, which is depended on time t. The rest of parameters are used in the model described in figure 6.1. Those parameters are defined in previous chapters, which are liquid pressure p_L, and the internal bubble pressure p_B.

κ, ρ, μ and σ are the specific heat parameters of the bubble gas, density and dynamics viscosity of the liquid, and surface tension, respectively. The model was further developed as the Gilmore model, which combines sound radiation and the fluid field [25]. Keller and Miksis developed the model, which considers sound radiation in the fluid field with a slowed down time t-r/c in the equations. We will compare the viscous compressible BIM with the Keller-Miksis model.

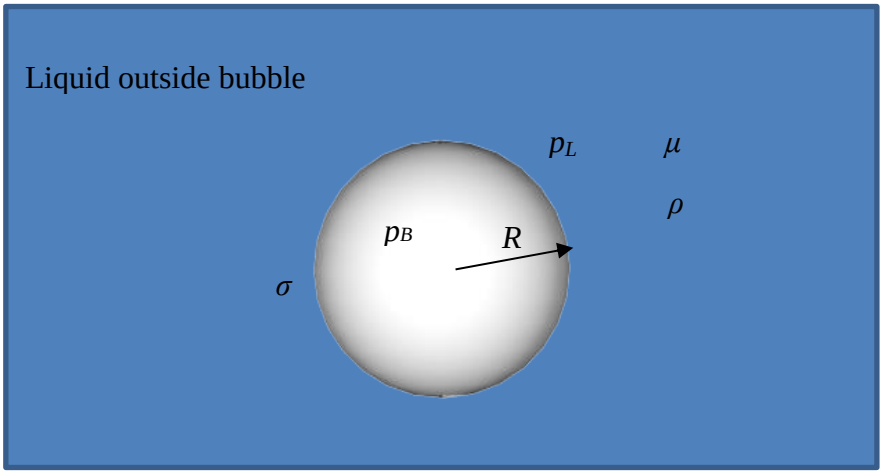

Figure 6.1. Sketching of a bubble in liquid and the parameters used in the calculation. The bubble radius is $R(t)$. The liquid pressure from outside liquid is p_L, and the pressure inside the bubble is p_B. The remaining parameters are specific heat parameter κ of the bubble gas, the density of liquid ρ and the dynamics viscosity μ of the liquid, and surface tension σ.

The Rayleigh-Plesset equation is described as following. The continuity equation for incompressible flow in spherical coordinates reads

$$\frac{1}{r^2}\frac{\partial}{\partial r}\left(r^2 u_r\right)=0\,, \tag{6.1.2}$$

integrating equation (6.1.2)

$$u_r = \frac{C(t)}{r^2}, \quad C(t) = R^2 R', \tag{6.1.3}$$

where "′" denotes derivative in *t*.

The Navier-Stokes equation reads

$$\frac{\partial u_r}{\partial t} + u_r \frac{\partial u_r}{\partial r} = -\frac{1}{\rho}\frac{\partial p_L}{\partial r} + \nu \frac{\partial}{\partial r}\left(r^2 \frac{d}{dr} r^2 u \right), \tag{6.1.4}$$

where $\nu = \mu/\rho$ is the kinematic viscosity. Substituting (6.1.3) into (4.14) yields

$$\frac{C'}{r^2} + 2\frac{C^2(t)}{r^5} = -\frac{1}{\rho}\frac{\partial p_L}{\partial r} + 0\,. \tag{6.1.5}$$

Integrating (6.1.5) concerning *r* from *R* to ∞ gives

$$\frac{C'}{R^2} - \frac{1}{2}\frac{C^2(t)}{R^4} = -\frac{p_\infty - p_L}{\rho}\,. \tag{6.1.6}$$

Substituting *C(t)* from equation (6.1.3) into equation (6.1.6) yields

$$R^2 R'' + \frac{3}{2} R'^2 = \frac{p_\infty - p_L}{\rho}\,. \tag{6.1.7}$$

The dynamic boundary condition on the bubble surface is

$$-\sigma_{rr} + \frac{2\sigma}{R} = p_B\,, \tag{6.1.8}$$

where $\sigma_{rr} = -p_L + 2\mu\frac{\partial u}{\partial r}$. Thus, we have

$$-p_L + 2\mu\frac{\partial u_r}{\partial r} - \frac{2\sigma}{R} = -p_B\,. \tag{6.1.9}$$

Substituting u_r form (6.1.3) into (6.1.9) gives

$$p_L = -4\mu\frac{R'}{R} - \frac{2\sigma}{R} + p_B\,. \tag{6.1.10}$$

Substituting (6.1.10) into (6.1.7) yields the Rayleigh-Plesset equation as following:

$$R^2 R'' + \frac{3}{2} R'^2 = -4\nu\frac{R'}{R} - \frac{2\sigma}{\rho R} + \frac{1}{\rho}(p_B - P_\infty) - p(t)\,. \tag{6.1.11}$$

Keller and Miksis developed the Rayleigh-Plesset equation to consider compressible effects, which resulted in the Keller and Miksis equation

$$\left(1-\frac{R'}{c}\right)RR''-\frac{3}{2}R'^{2}\left(1-\frac{R'}{c}\right)=\left(1-\frac{R'}{c}\right)\frac{p_l}{\rho}+\frac{R}{\rho}\frac{dp_L}{dt}, \tag{6.1.12}$$

where

$$p_L=p_{g0}\left(\frac{R_0}{R}\right)^{3\kappa}-\frac{4\mu R'}{R}-\frac{2\sigma}{R}-(p_\infty-p_v)-p_a(\mathbf{r}_i,t), \tag{6.1.13}$$

the reference length is chosen as the initial bubble radius $R_{0,}$ and the reference velocity is $U=\sqrt{\Delta/\rho}$, $\Delta=p_\infty-p_v$, we introduce the following asterisk to describe the dimensionless variables,

$$R=R_0R_*,\ t=Tt_*=\frac{R_0}{U}t_*, \tag{6.1.14a, b, c}$$

$$p_a=p_{a*}\Delta,\ p_{g0}=p_{g*}\Delta,\quad \varepsilon=\frac{U}{c}. \tag{6.1.15a, b, c}$$

Using the above dimensionless variables, we get the first and the second order of differentiation of the bubble radius with respect to time *t* in dimensionless variables, and the differentiation of the liquid pressure p_L as following;

$$R'=UR_*',\quad R''=\frac{U}{T}R_*''=\frac{U^2}{R_0}R_*'', \tag{6.1.16a, b}$$

$$p_L'=\frac{\Delta}{T}\frac{dp_{L*}}{dt_*}=\frac{U\Delta}{R_0}\frac{dp_{L*}}{dt_*}=\frac{p_0\Delta}{R_0}\frac{dp_{L*}}{dt_*}. \tag{6.1.17}$$

The dimensionless surface tension can be expressed as following;

$$\sigma_*=\frac{\sigma}{\rho R_0U^2}=\frac{\sigma}{R_0\Delta}. \tag{6.1.18}$$

By substituting the dimensionless variables from (6.1.14a, b, c) and (6.1.15a, b, c) into the

Keller equation, then replacing the differentiation of the radius and liquid pressure in dimensionless from (6.1.16) and (6.1.17), we get the Keller equation in dimensionless variables as following:

$$\left(1-\varepsilon R_*'\right)R_*R_*''+\frac{3}{2}R_*'^2\left(1-\frac{1}{3}\varepsilon\dot{R}_*'\right)=\left(1+\varepsilon R_*'\right)p_{l*}+R_*p_{L^*}', \tag{6.1.19}$$

with the dimensionless liquid pressure and initial partial pressure of the non-condensable gases of the bubble are given as follows:

$$p_{L^*}=p_{g0*}\left(\frac{R_0}{R}\right)^{3\kappa}-\frac{4R_*'}{R_e}-\frac{2\sigma_*}{R_*}-1-p_{a^*}, \tag{6.1.20}$$

$$p_{g0_*}=\begin{cases}1+\dfrac{2\sigma_*}{R_{0*}} & \text{for a bubble started at equilibrium state,}\\ p_{g0*} & \text{for a transient bubble.}\end{cases} \tag{6.1.21}$$

6.2 The viscous compressible BIM for acoustic bubbles

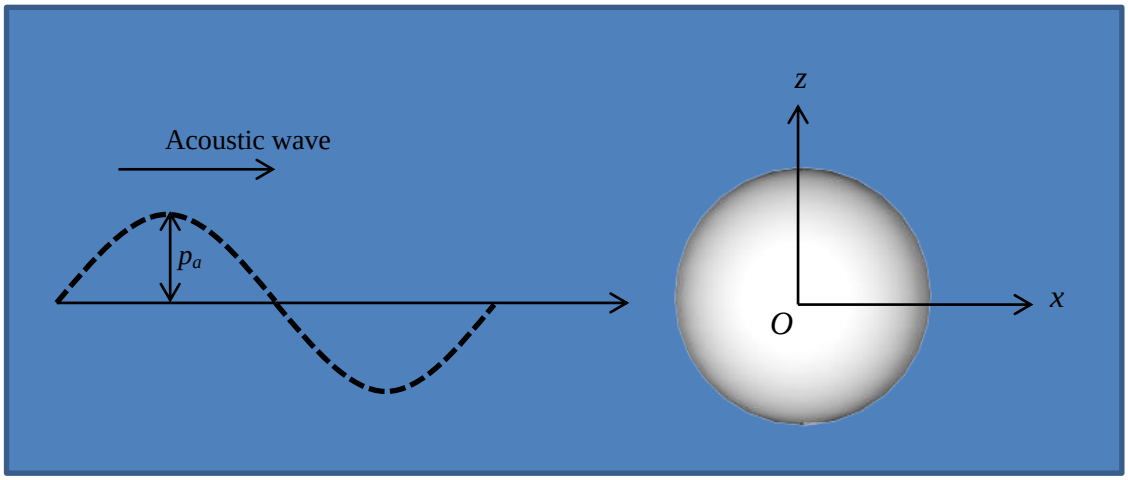

Figure 6.2. Sketch of a bubble motion in an infinite fluid subject to an ultrasound wave and the coordinates used.

Consider the dynamics of a microbubble in an infinite fluid subject to an ultrasound wave, as shown in figure 6.2. A Cartesian coordinate system *O*-*xz* is adapted to the origin at the centre of the initial spherical bubble; the *x*-axis is along the wave direction. The ultrasound wave is described as a plane harmonic acoustic wave as follows:

$$p_\infty(x,t) = p_0 + p_a \sin(kx - \omega t), \tag{6.2.1}$$

where p_0 is the hydrostatic pressure, t is time, and k, p_a and ω are the wave number, pressure amplitude and angular frequency of the acoustic wave, respectively.

We choose initial bubble radius R_0 as the reference length, and the density of the liquid ρ_∞ in the undisturbed liquid is chosen as the reference density. The pressure reference is chosen as $\Delta p = p_\infty - p_v$, where p_v is the partial pressure of vapour of the bubble. The reference velocity U

is $U=\sqrt{\Delta p/\rho_\infty}$.

By using (3.1.13a, b, c, d, e) and the following dimensionless parameters to perform non-dimensionalization to the problem: the dimensionless quantities denote by subscripts "*" as follows:

$$\sigma_* = \frac{\sigma}{R_0 \Delta p}, \quad \varepsilon = \frac{p_{g0}}{\Delta p}, \quad p = \frac{p - p_\infty}{\Delta p}, \tag{6.2.2a, b, c}$$

$$\omega_* = \omega R_0 \sqrt{\frac{\rho}{\Delta p}}, \quad p_{a^*} = \frac{p_a}{\Delta p}, \quad k_* = R_0 k, \tag{6.2.2d, e, f}$$

where ω_* and k_* are the dimensionless angular frequency and wave number.

The governing equations for the ultrasound wave driving a bubble in the compressible liquid are provided by Wang [103, 104]. The velocity potential φ satisfies the kinematic and dynamic conditions on the bubble surface S and Laplace's equation in the flow field as following:

$$\nabla_*^2 \varphi_* = O\left(\varepsilon^2\right), \tag{6.2.3a}$$

$$\frac{d\mathbf{r}_*}{dt_*} = \nabla_* \varphi_* + O\left(\varepsilon^2\right) \quad \text{on } S, \tag{6.2.3b}$$

$$\begin{aligned} \frac{d\varphi_*}{dt_*} = {} & \frac{1}{2}\left|\nabla_* \varphi_*\right|^2 - p_{L^*} - \frac{z_*}{Fr^2} - \frac{2}{\mathrm{Re}} \frac{\partial^2 \varphi_*}{\partial n^2} - p_{vc^*} + 1 \\ & + p_{a^*} \sin\left(k_* x_* - \omega_* t_*\right) + \varepsilon \frac{V_0''\left(t_*\right)}{2\pi} + O\left(\varepsilon^2\right) \text{ on } S, \end{aligned} \tag{6.2.3c}$$

here p_{L^*} is the liquid pressure on the bubble surface which is defined in equations (3.1.40a, b). The details on the derivation for considering viscous effect in (6.2.3c) are provided in Chapter 4.

6.3 Validation

6.3.1 Comparison with the Keller-Miksis equation

Figure 6.3 compares the results obtained from the VCBIM (solid red line) with the Keller-Miksis equation (KME) (blue dash line). The bubble is with an initial diameter of 26 μm is driven by eight-cycles of acoustics wave with pressure amplitude of 20 kPa and frequency of 130 kHz. The two results agree for the first three cycles, but discrepancy occurs subsequently.

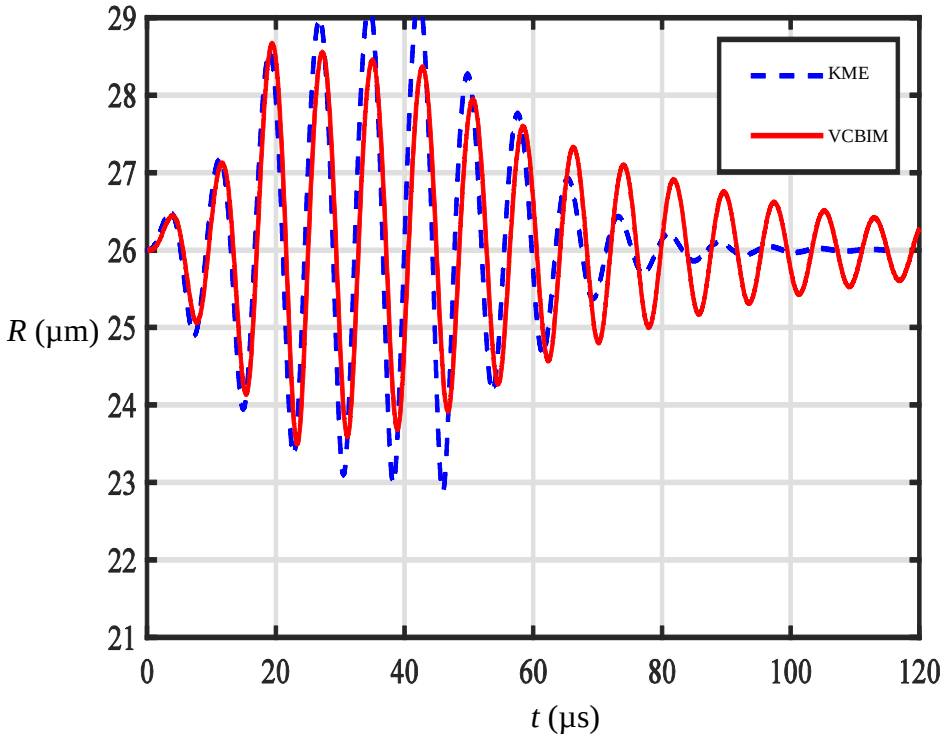

Figure 6.3. Comparison between results obtained from the VCBIM (red solid line) and the Keller Miksis model (blue dotted line) radius history $R(t)$ curves of a bubble with a resting diameter of 26 μm insonified at 130 kHz and 20 kPa for eight cycles. The other parameters are $\lambda = 1.4$, $\sigma = 0.073$ N/m, $p_0 = 101$ kPa, $p_v = 98.02$ kPa and $\rho = 1000$ kg·m^{-3}.

6.3.2 Comparison with experiment for bubble shapes

Versluis et al. [119] carried out a series of carefully controlled experiments for dynamics of a gas bubble driven by an ultrasound wave. They observed shape oscillation for various mode number $n = 2$ to 6 of microbubbles. They found that the mode number n is dependent on the bubble radius but is independent of the pressure amplitude. To compare with the experiments, we consider the experimental case for a gas bubble having an initial radius 36 μm subject to an acoustic wave with the frequency of 130 kHz and pressure amplitude of 120 kPa. The bubble shapes are shown in figure 6.4 with the left column for the experimental images and the right column for the computational results. The computation results are also plotted in

dashed lines over the experimental images for quantitative comparison. The bubble shapes are shown roughly at the maximum and minimum bubble volumes.

Figure 6.4a shows the bubble shapes from the beginning to the 5th cycle of oscillation. The bubble is in equilibrium state before the arriving of the acoustic wave. In the first frame, the bubble starts to collapse as the acoustic wave defined by (6.2.1) arrives, since the acoustic pressure is positive at $t = 0$ and $x = 0$. During the first five cycles, the bubble vibrates in a spherical shape ($n = 0$), and the bubble shape and radius agree well with the experimental images in the very closing time with experiment results.

Figure 6.4b shows the bubble shapes from the 6^{th} to 9^{th} cycles of oscillations. As the bubble at the 6^{th} maximum volume, the left side part of the bubble surface is slightly oblate and the right part is slightly elongated. At the 6^{th} minimum, its cross section takes a square shape with rounding corners and a jet forming on the left side. The jet develops as the bubble expands until the end of the expansion (the 7^{th} maximum). The surface mode $n = 4$ becomes obvious at and after the 7^{th} minimum volume.

The computational results agree excellently with the experimental images for all nine cycles of oscillation, with all features reproduced by the computations. However, the jet is not visible in the experimental images due to the opaqueness of the bubble.

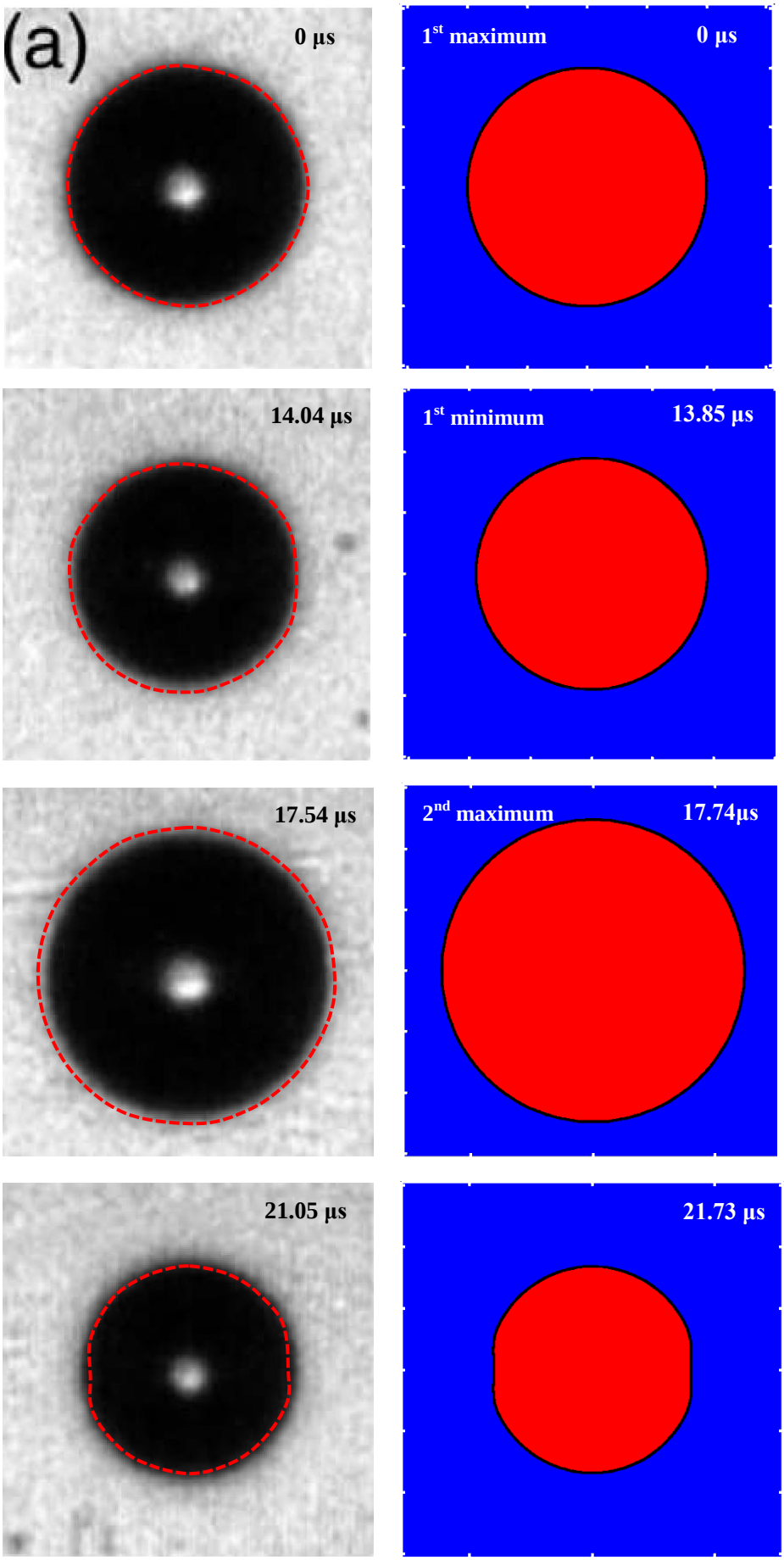
(a)
0 µs
1st maximum
0 µs
14.04 µs
1st minimum
13.85 µs
17.54 µs
2nd maximum
17.74µs
21.05 µs
21.73 µs

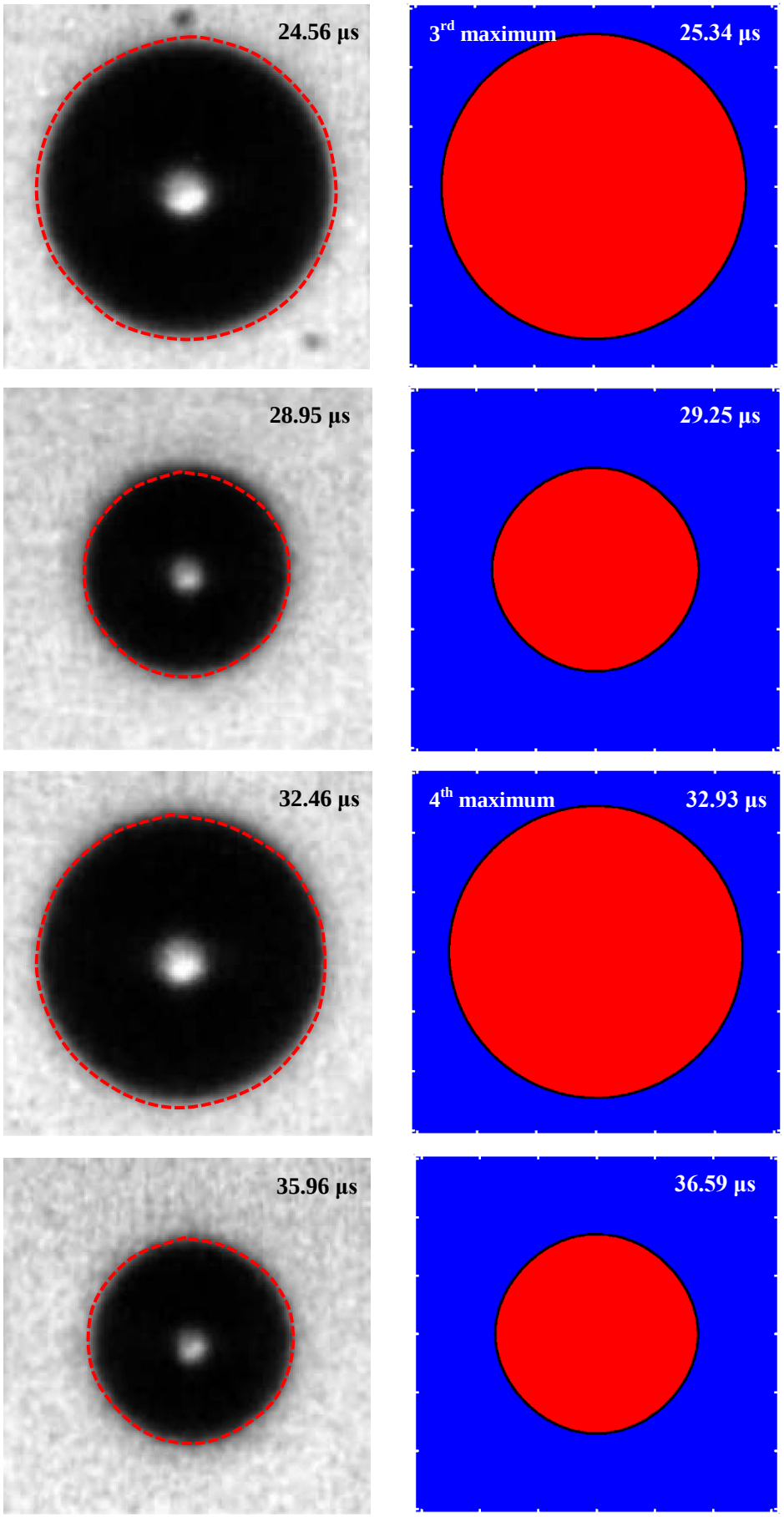
24.56 µs
3rd maximum
25.34 µs
28.95 µs
29.25 µs
32.46 µs
4th maximum
32.93 µs
35.96 µs
36.59 µs

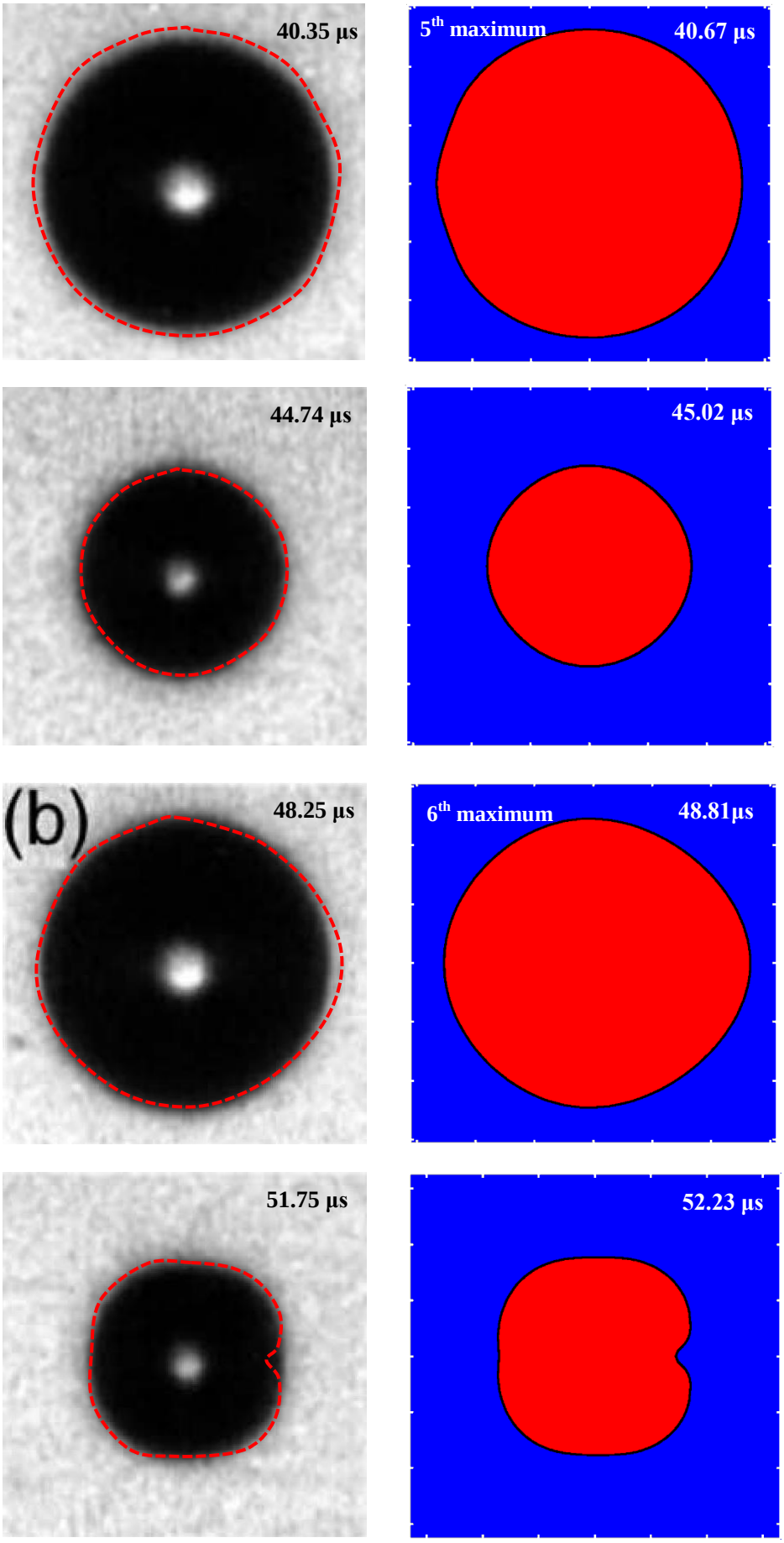
40.35 µs
5th maximum
40.67 µs
44.74 µs
45.02 µs
(b)
48.25 µs
6th maximum
48.81µs
51.75 µs
52.23 µs

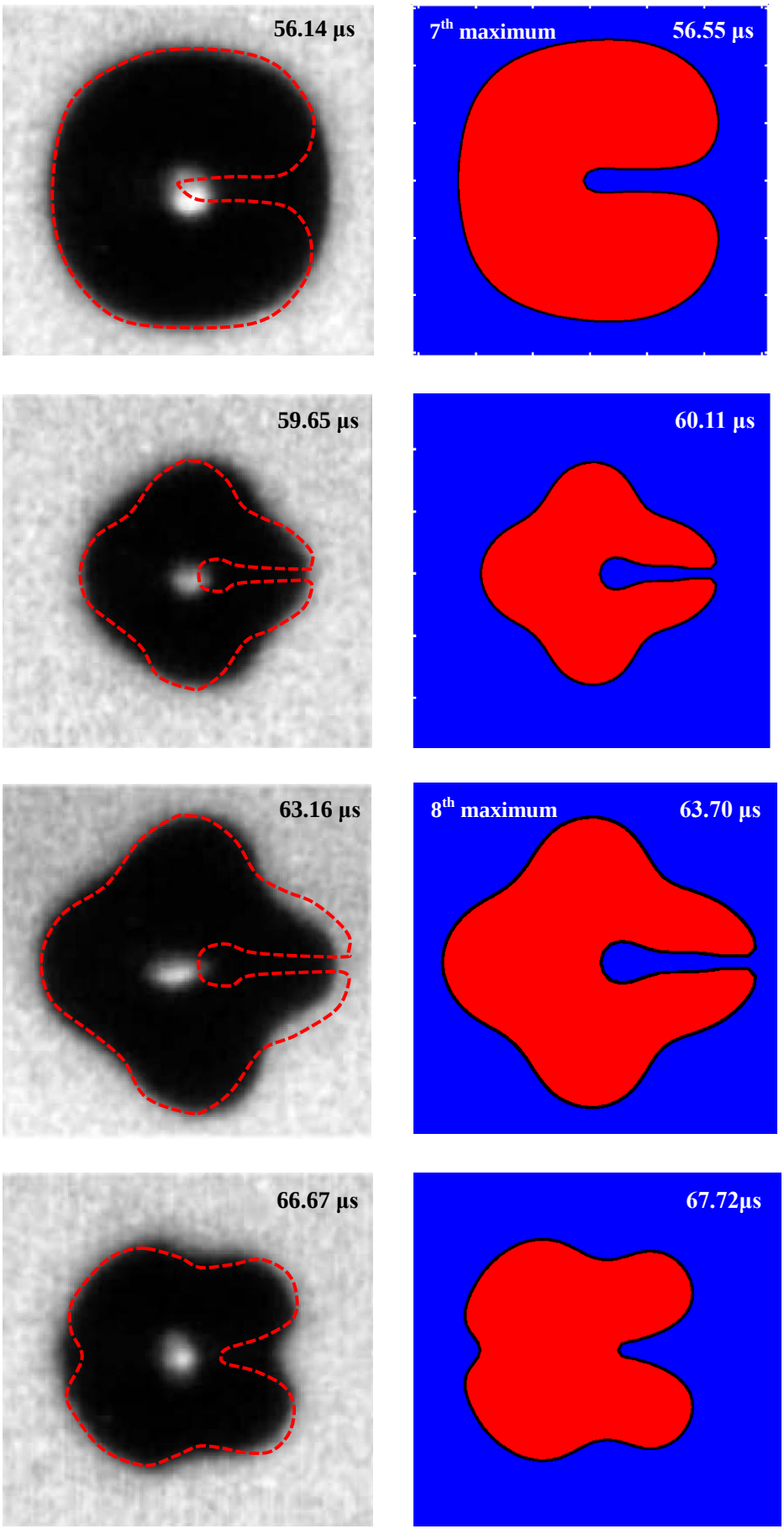
56.14 µs
7th maximum
56.55 µs
59.65 µs
60.11 µs
63.16 µs
8th maximum
63.70 µs
66.67 µs
67.72µs

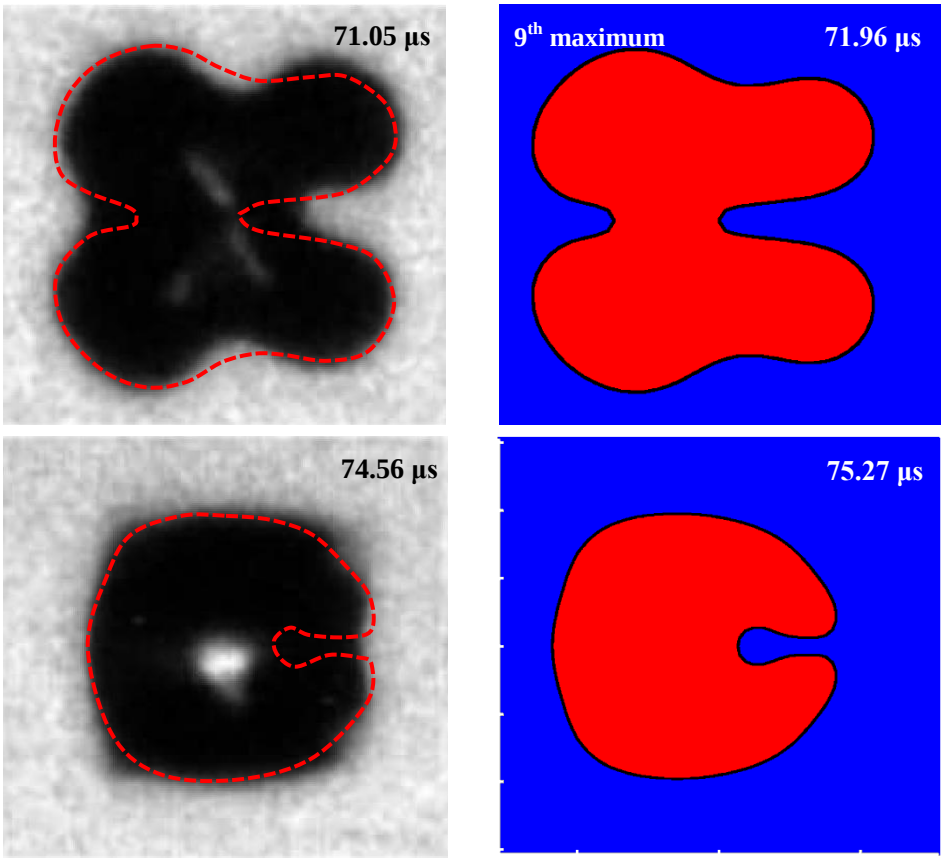

Figure 6.4. Comparison between the bubble shapes of the VCBIM (in the right column) and the experiments (in the left column Veraluis et al. [119]) for a gas bubble of a radius 36 µm subject to an acoustics wave with the frequency 130 kHz and pressure amplitude 120 kPa: (a) spherical oscillation for the first five cycles of oscillation and (b) the development of a surface mode $n = 4$ from the 6^{th}-9^{th} cycles of oscillation. The frame width is 56 µm. The remaining parameters are $\lambda = 1.4$, $\sigma = 0.073$ N/m, $p_0 = 101$ kPa, $p_v = 98.02$ kPa and $\rho = 1000$ kg·m^{-3}.

6.4 Numerical results and discussions

6.4.1 Effects of the pressure amplitude of ultrasound p_a

In this section, we perform the numerical analyses of microbubble dynamics driving by an ultrasound wave, propagating from the left side to the right side. To study the effects of the pressure amplitude, we consider three cases for the pressure amplitude $p_a = 40$, 47 and 50 kPa, respectively, with the remaining parameters keep the same as in figure 6.5.

Figure 6.5 shows the bubble shapes for pressure amplitude $p_a = 40$ kPa at its successive maximum and minimum volumes after its 18 cycles of oscillation. It keeps being spherical for subsequent five cycles. The driving pressure amplitude is lower than the critical pressure threshold; the bubble keeps spherical during the whole oscillation period. This is consistent with the observation of Versluis et al. [119].

Figure 6.6 shows the bubble shapes for pressure amplitude $p_a = 47$ kPa at its successive maximum and minimum volumes after its first 14 cycles of spherical oscillation. The bubble is approximately spherical at the 15^{th} minimum and maximum volumes, but hits left side is slightly flattened. From the next oscillation, the right side is flattened at the 16^{th} minimum and maximum volumes. A jet forms at the 17^{th} and 18^{th} minimum volumes at the left side right side alternatively. Surface mode $n = 3$ becomes obvious subsequently.

Figure 6.7 shows the bubble shapes for pressure amplitude $p_a = 50$ kPa after eight cycles of spherical oscillation. The bubble is slightly oblate and the right part elongated at the 9^{th}

minimum and maximum volumes. The jet forms at the right side at the 10^{th} minimum volume, and it changes to the left side at the 11^{th} minimum volume. Surface mode $n = 3$ develops obviously subsequently. As compared to figure 6.6 for $p_a = 47$ kPa, the ultrasound at larger amplitude generates shape mode earlier and at large amplitude.

Figure 6.5, 6.6 and 6.7 show pressure amplitude $p_a = 40$, 47 and 50 kPa, and the bubble keeps spherical oscillations for twenty-four, fourteen and eight cycles, respectively. When the bubble is subject to the larger pressure amplitude of the ultrasound wave, it becomes non-spherical earlier as it is under a larger Bjerknes force.

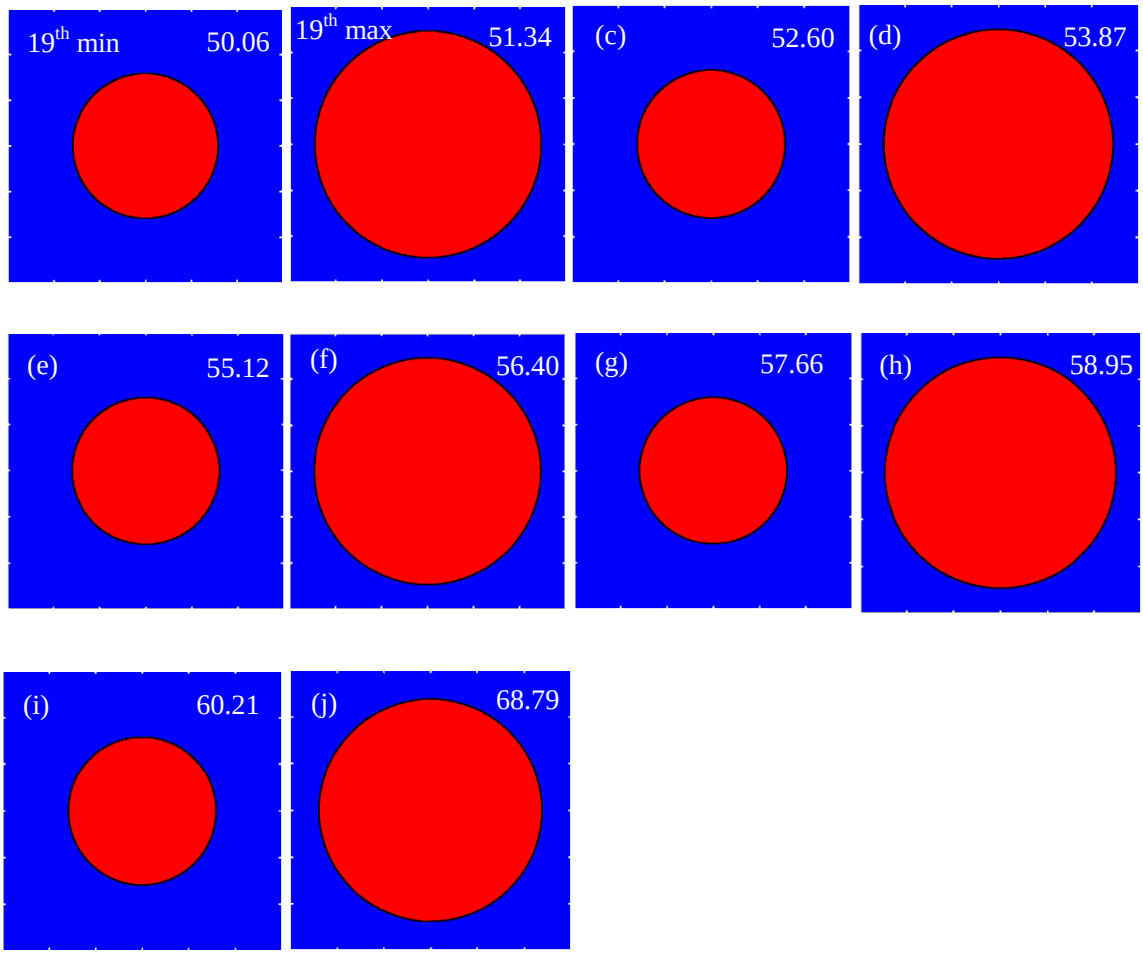

Figure 6.5. Dynamics of a bubble with an equilibrium radius R_0 = 30 μm driving by an acoustic wave for pressure amplitude p_a = 40 kPa and frequency f = 130 kHz. The remaining parameter are σ = 0.073 N·m^{-1}, p_0 = 101 KPa, p_v =98.02 kPa, ρ = 1000 kg/ m^3 and κ = 1.4. The dimensionless time is shown on the right-up corner in each frame.

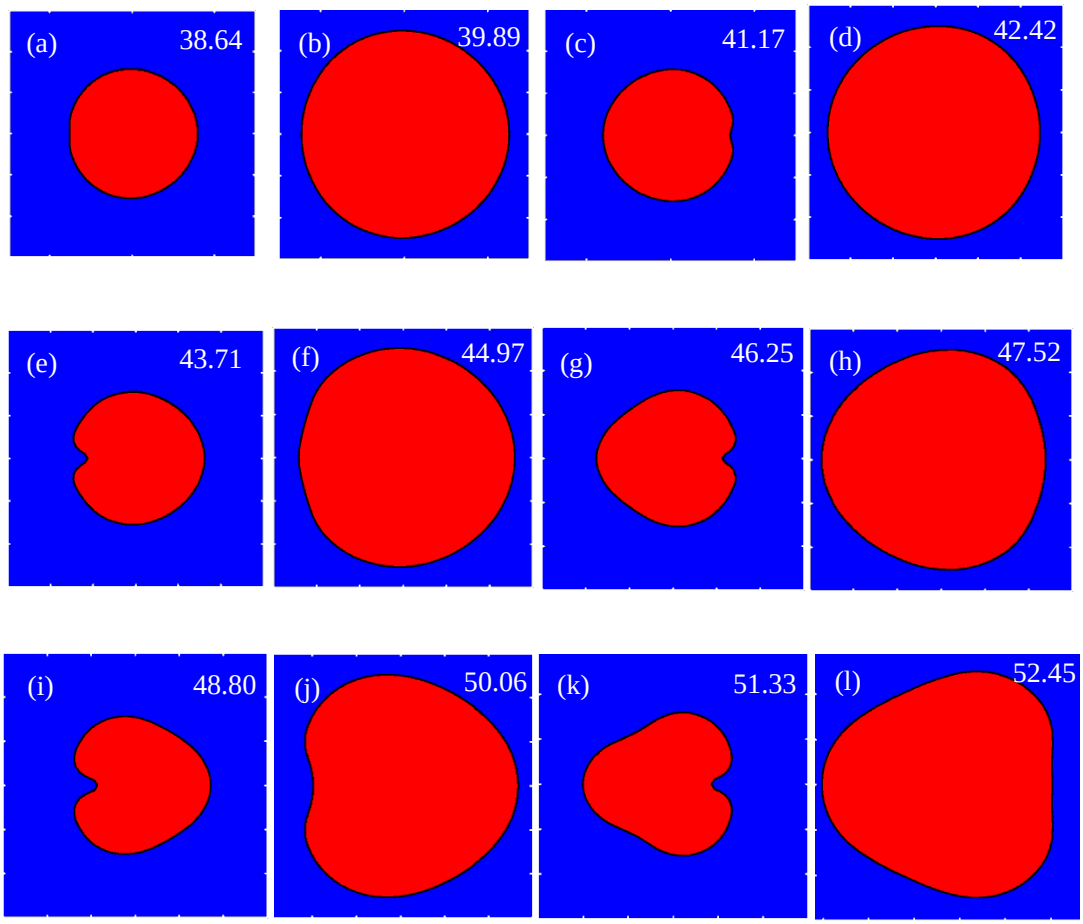

Figure 6.6. Dynamics a bubble driving by an acoustic wave of pressure amplitude $p_a = 47$ kPa.

The remaining parameters are the same as in figure 6.5.

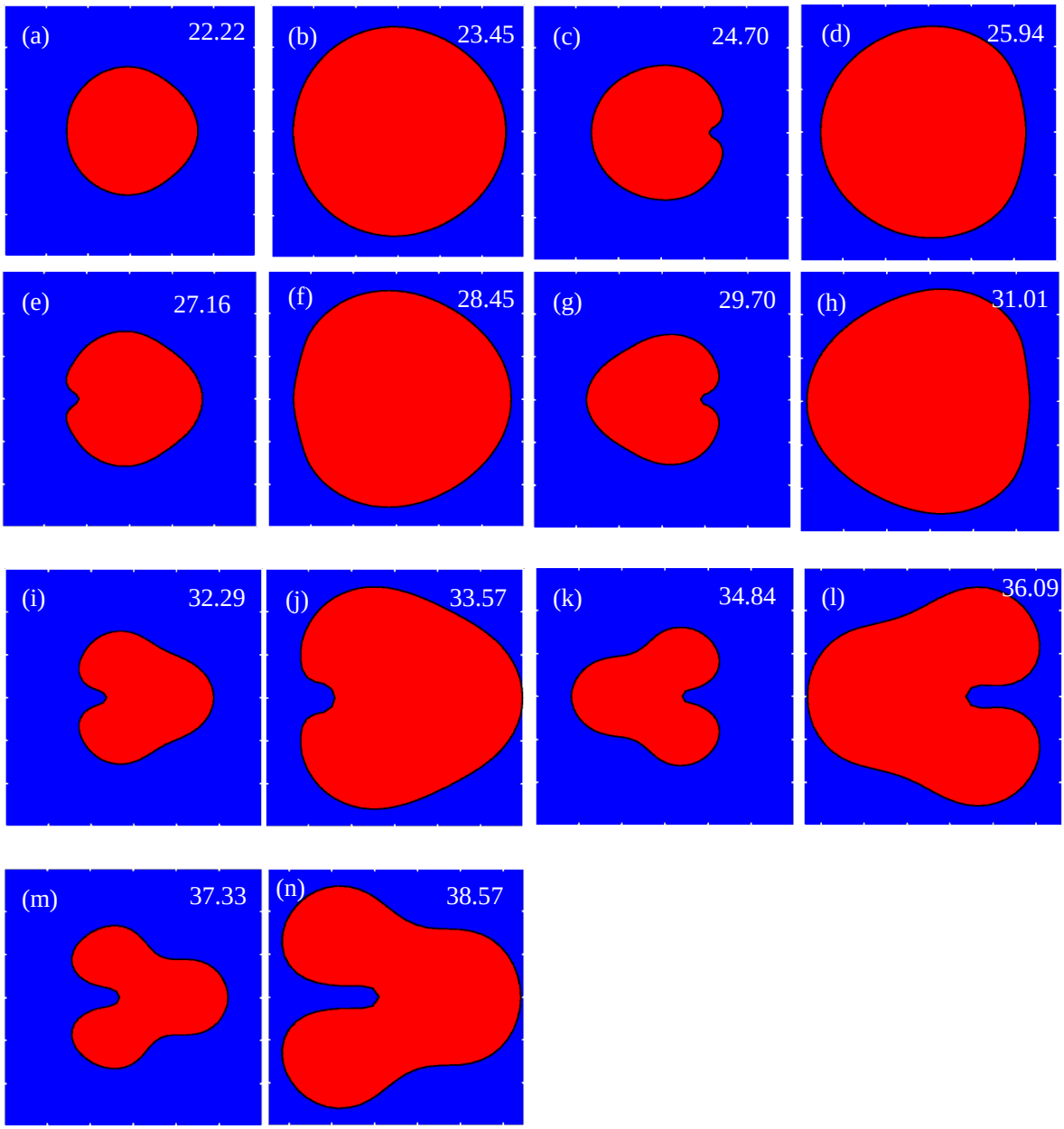

Figure 6.7. Dynamics of a bubble driving by an acoustic wave for pressure amplitude $p_a = 50$ kPa. The remaining parameters are the same as in figure 6.5.

6.4.2 Effects of the driving frequency of ultrasound

To consider the effects of the driving frequency, we repeat the case shown in figure 6.6 for acoustic pressure amplitude p_a = 47 kPa and frequency f = 85, f_0, where $f_0 = 1.1\times10^5$ Hz is the natural frequency of the bubble obtained from

$$f_0 = \frac{1}{2\pi}\sqrt{\frac{3\kappa p_0}{\rho R_0^2}}\,. \qquad (6.4.2.1)$$

Figure 6.8 shows the bubble shapes at the time of reaching its maximum and minimum volumes for each cycle of oscillation for $f = f_0 = 1.1\times10^5$ Hz. The bubble is spherical during most of the time of the first cycle of oscillation but a jet forms at the left side at the end of the first collapse phase, as shown in frames a-c. The bubble re-takes a spherical shape at the 2nd maximum volume (frame f) and the jet re-appears at the end of the 2nd minimum volume (frame g). The bubble at the 3rd and 4th maximum volumes (frames h, j) become oblate along the wave direction. Two contour jets develop at the 4th minimum volume (frame k) and impacts each other during the subsequent expansion becoming toroidal (frames l, m). The bubble then rejoins before reaching the 5th maximum volume. The singly connected bubble further oscillates.

Figure 6.9 shows the bubble shapes after 20 cycles of oscillation for f = 85 kHz. The bubble oscillates spherically from 21st to 24th cycles. The bubble undergoes obvious non-spherical oscillation as the driving frequency is equal to the natural frequency of the bubble $f = f_0$. It oscillates spherically as $f > f_0$ (figure 6.9) and $f < f_0$ (figure 6.6).

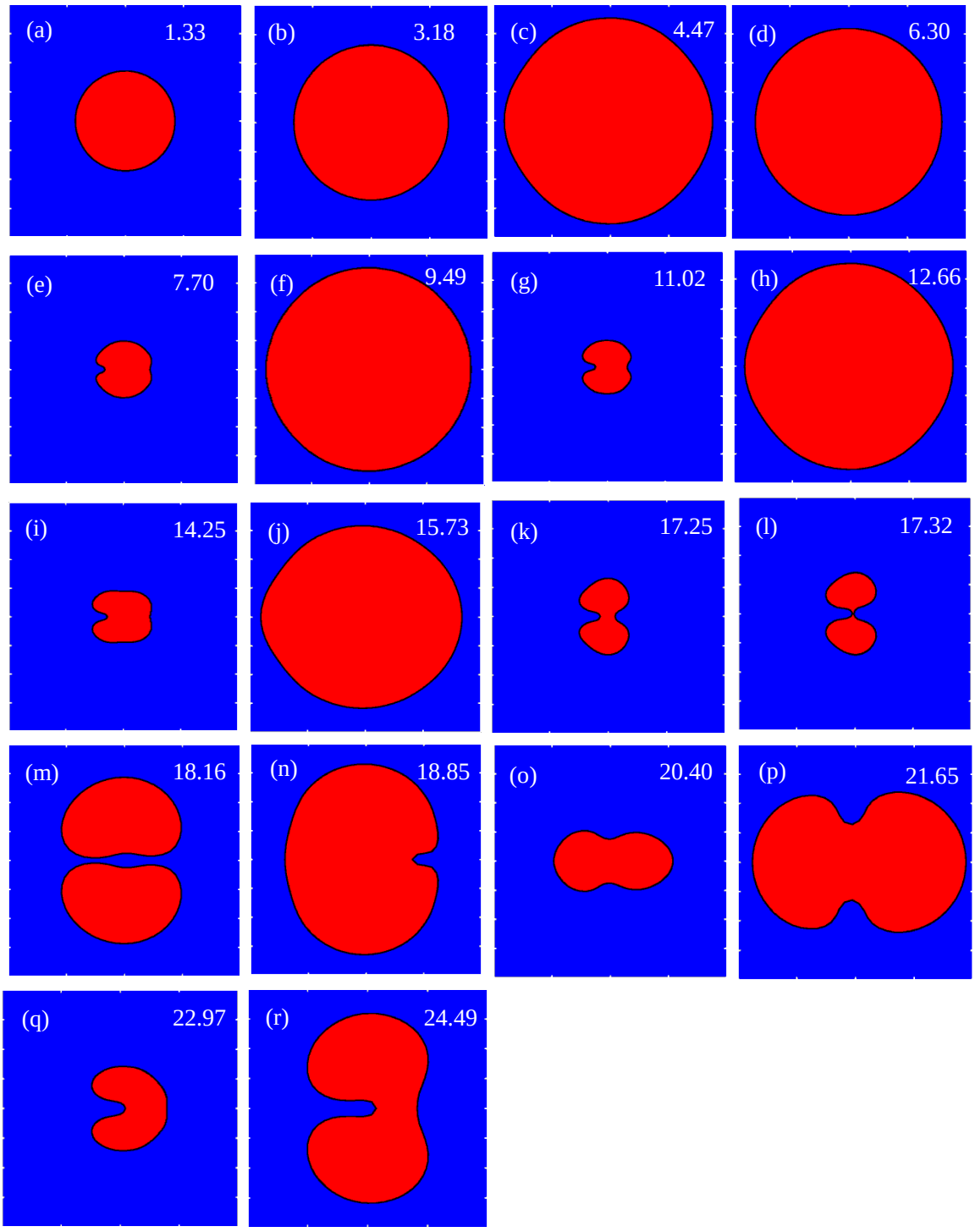

Figure 6.8. Bubble dynamics subject to an acoustic wave with the pressure amplitude $p_a = 47$ kPa and frequency $f = f_0 = 1.1\times10^5$ Hz. The remaining parameters are the same as in figure 6.5.

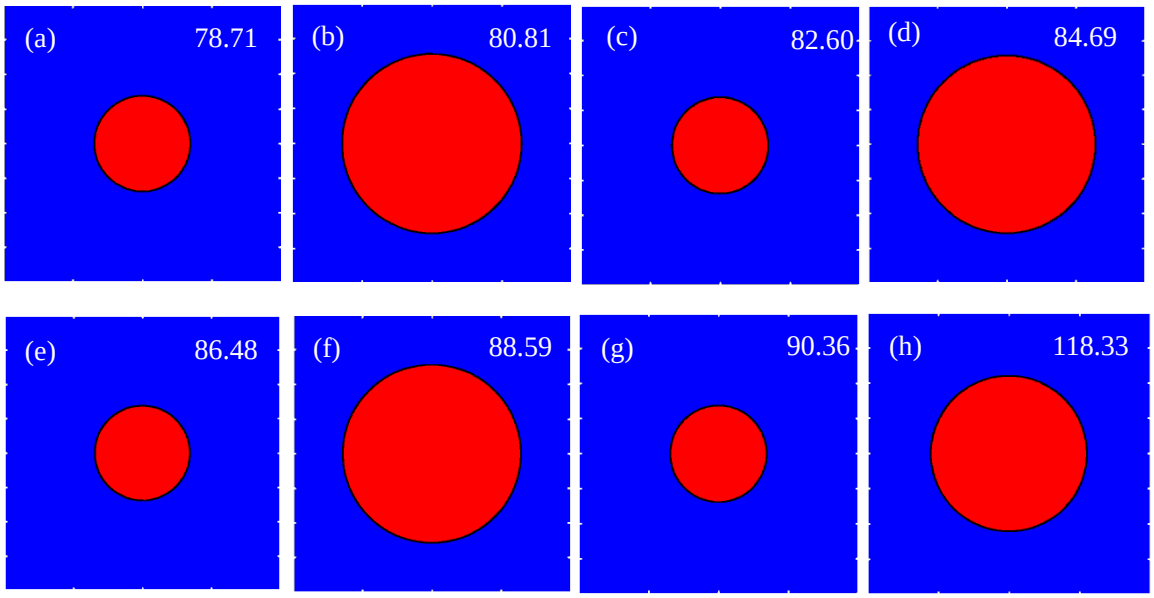

Figure 6.9. Bubble dynamics subject to acoustic wave for $f = 8.5\times10^{4}\,\mathrm{Hz}$. The rest of the parameters are the same as in figure 6.5.

Figure 6.10 illustrates the histories of the bubble volume $(3/4\pi)v_*$ and centroid x_{cen*} for the three cases shown in figures 6.6, 8 and 9. When the driving acoustic wave is equal to the natural frequency of the bubble, the amplitude of oscillation and translation is much larger than the other two cases.

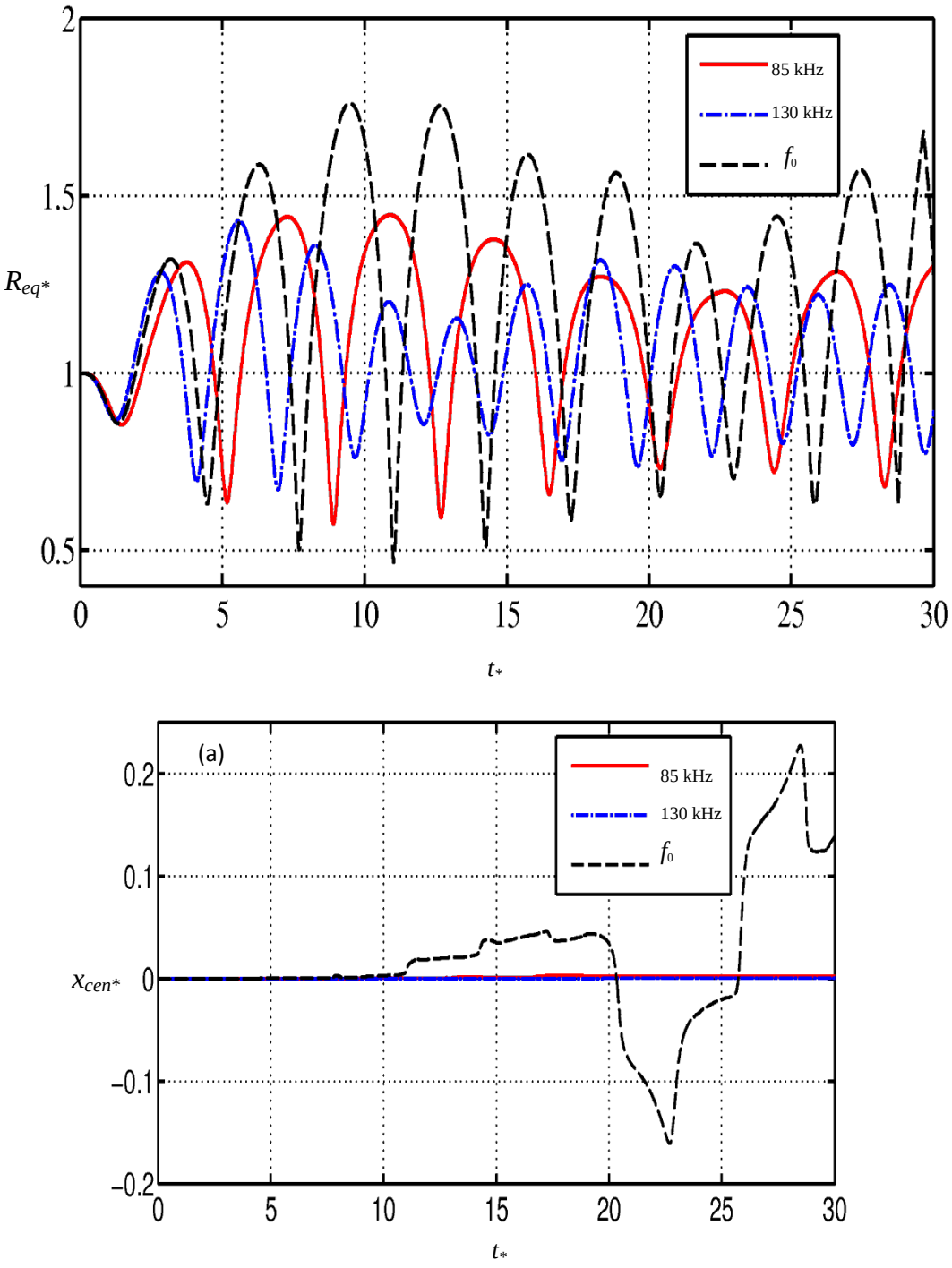

Figure 6.10. Time histories of (a) the bubble volume $(3/4\pi)v_*$ and (b) the centroid x_{cen*} for the cases shown in figures 6.7, 8 and 9.

6.4.3 Driving frequency equal to parametric resonance frequency

The natural frequency ω_n of shape modes n of bubbles is given as [119]

$$\omega_n^2 = (n-1)(n+1)(n+2)\frac{\sigma}{\rho R_0^3}, \qquad (6.4.3.1)$$

For $R_0 = 39$, $\sigma = 0.073$ N·m^{-1}, $\rho = 1000$ kg/ m^3 and $\kappa = 1.4$, the natural frequencies for shape modes for n = 3, 4, 6 are f_3=7.0623×10^4 Hz, f_4=1.4473×10^{5}Hz and f_6=1.9427×10^5 Hz.

Figure 6.11 shows the bubble shapes at the maximum and minimum volumes for the driving pressure amplitude p_a = 40 kPa and frequency f_3=7.0623×10^4 Hz. The bubble oscillates for cycles in spherical volumetric mode and the Figure 6.11 (a), (b) present the first cycle, the bubble developed the surface mode $n = 3$ when it reaches the end of collapsing and when it expands to the maximum volume, the left part of the bubble has been flattened. The bubble oscillates as the surface mode $n = 3$ for the rest of oscillations. Figure 6.11 (c), (d) show the thirteenth oscillation of the bubble whose minimum and maximum volume are roughly same as the previous cycle, the difference is that the jet is oppositely directed at the end of collapse and the right part of the bubble has been flatten in the end of the expansion. The next four cycles of the oscillation are similar to the Figure 6.11 (a)-(d) with it repeats for every two cycles of oscillation.

Figure 6.12 shows the bubble shapes for driving pressure p_a = 75 kPa and frequency f_4=1.4473×10^{5}Hz at its maximum and minimum volumes for each cycle of oscillation. The bubble becomes non-spherical at the 3rd minimum volume. In the fourth oscillation, the bubble is elongated along the wave direction. The bubble becomes square shape in both 5th

and 8th minimum and maximum volumes, displaying the surface mode n = 4. During the 9th cycle, two counter jets develop along the wave direction and impacts each other at the end of the 9^{th} collapse.

Figure 6.13 shows the bubble shapes for driving pressure amplitude p_a = 235 kPa and frequency $f_6 = 1.9427 \times 10^5$ Hz. The bubble oscillates for thirteen cycles in spherical volumetric mode and the Figure 6.13 (a), (b) present the first cycle, the bubble developed the surface mode $n = 6$ at the end of the collapsing, and is formed as the square shape at the end of the expansion. For the next three cycles of the oscillation, the bubble oscillates as the surface mode $n = 4$ but in the different shapes of mode 4. Figure 6.13 (i), (j) show the eighteenth cycle of the oscillation when the bubble reaches the minimum volume surface mode $n = 6$ formed again. For the next cycle of oscillation the bubble forms as the surface mode $n = 4$. In the end Figure 6.13 (m)-(p) present the bubble development of the surface mode n = 6 in both maximum and minimum volumes.

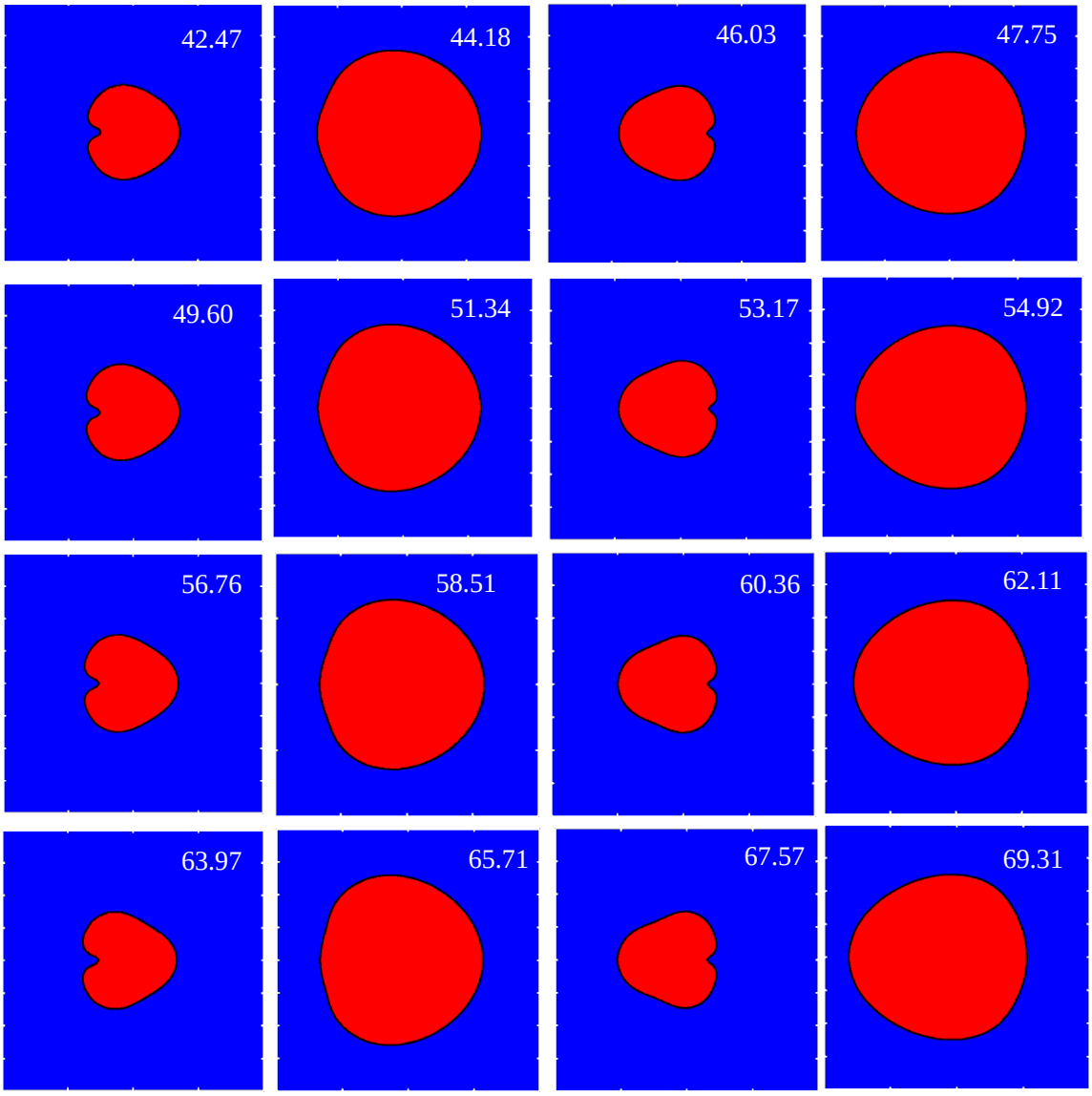

Figure 6.11. The motion of a bubble with the initial steady state radius R_0 = 39 μm driving by an acoustic wave the driving pressure amplitude p_a = 40 kPa and frequency f_3=7.0623×10^4 Hz . The remaining parameters are the same as in Figure 6.5.

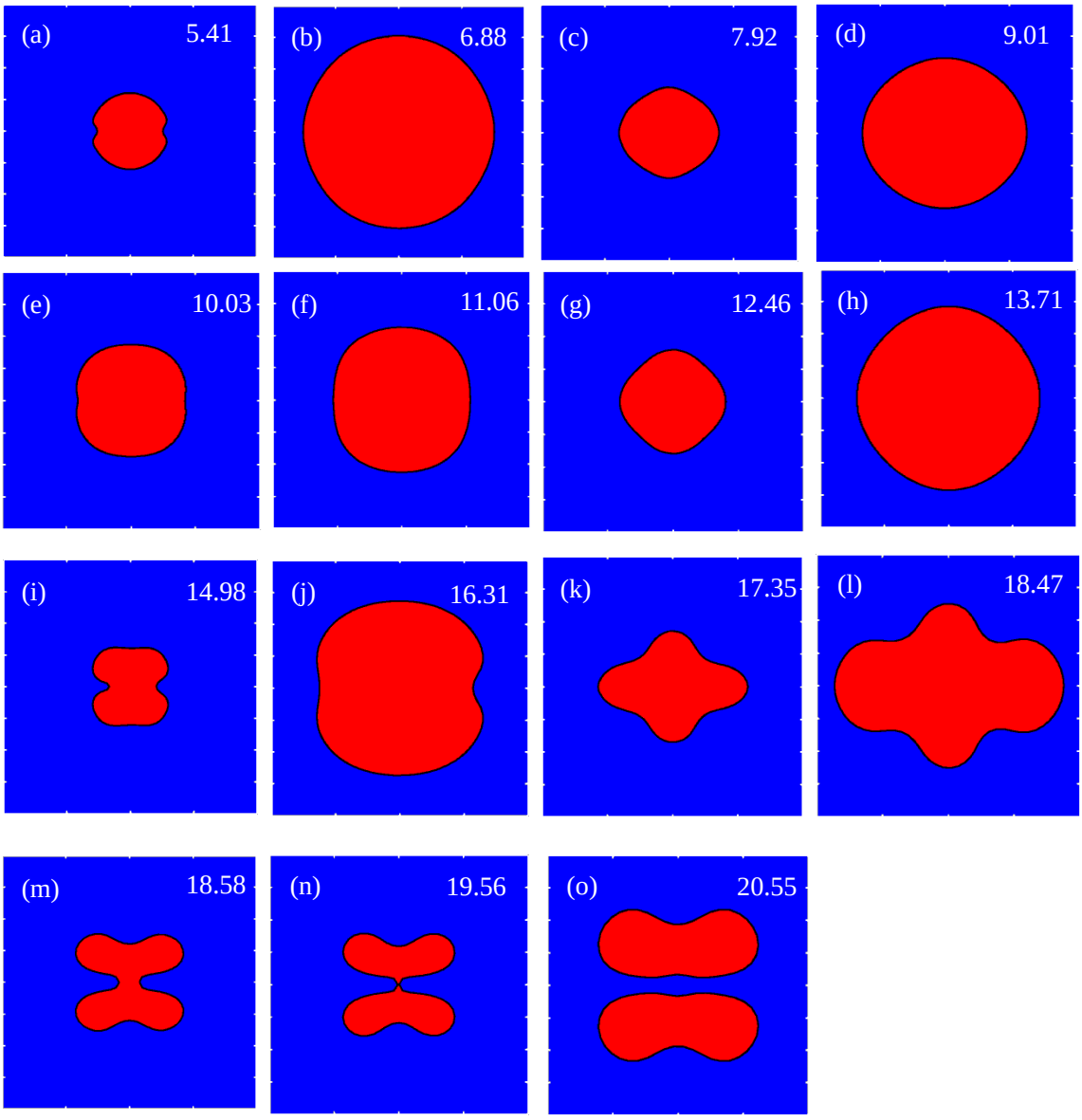

Figure 6.12. The motion of a bubble with the initial steady state radius $R_0 = 39$ μm driving by an acoustic wave for $p_a = 75$ kPa and $f_4 = 1.4473 \times 10^5$ Hz. The remaining parameters are the same as in Figure 6.5.

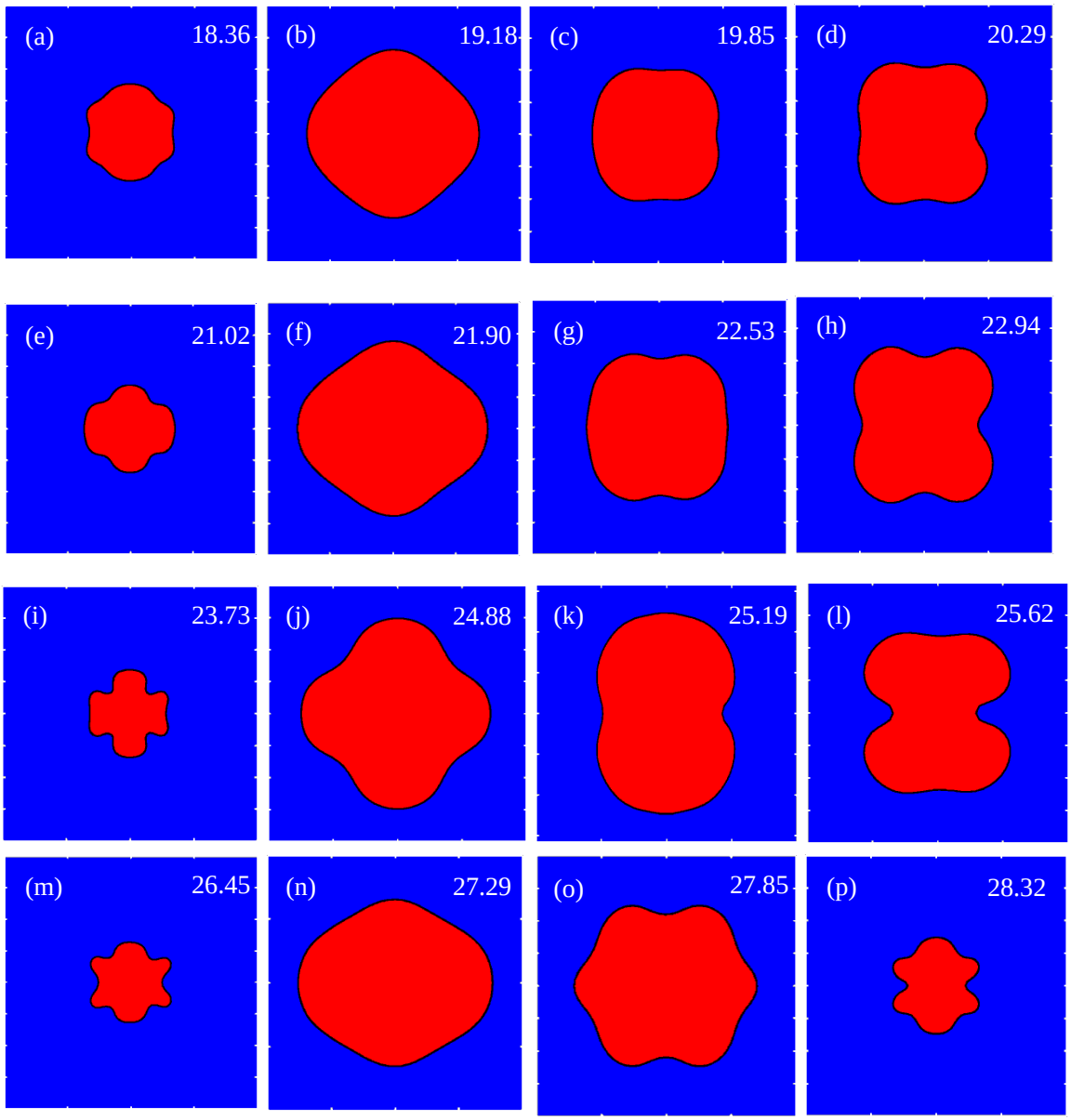

Figure 6.13. The motion of a bubble with the initial steady state radius R_0=39 μm driving by an acoustic wave for p_a = 235 kPa and frequency f_6=1.9427×10^5 Hz . The remaining parameters are the same as in Figure 6.5.

Figure 6.14 illustrates the convergence of the numerical results in terms of the mesh size for m = 51, 61 and 71, for the time history of the bubble equivalent radius R_{eq^*}. The numerical results for m = 61 and 71 agree excellently for nine cycles of oscillation. Most of the

calculations in this thesis were done for $m = 61$.

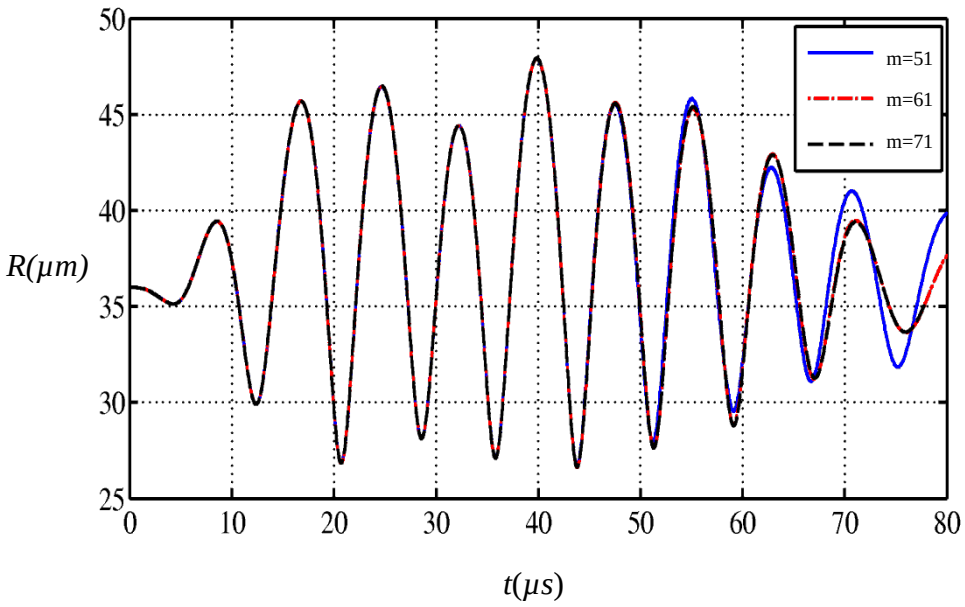

Figure 6.14. Convergence test in terms of the mesh size m for the time histories of the equivalent bubble radius R_{eq*} using the CVBIM for R_0 = 36 μm, $p_a = 1.2\times10^5$ Pa and f = 1.3×10^5 Hz. The remaining parameters are the same as in Figure 6.5.

Figure 6.15 presents the comparison of the computational results between the compressible inviscid BIM (ICBIM) and VCBIM for the bubble radius history for the case in figure 6.14. The amplitude of the oscillation predicted by the VCBIM considering the viscous damping effects is lower than that of CIBIM. The VCBIM is more stable and its calculation lasts longer time.

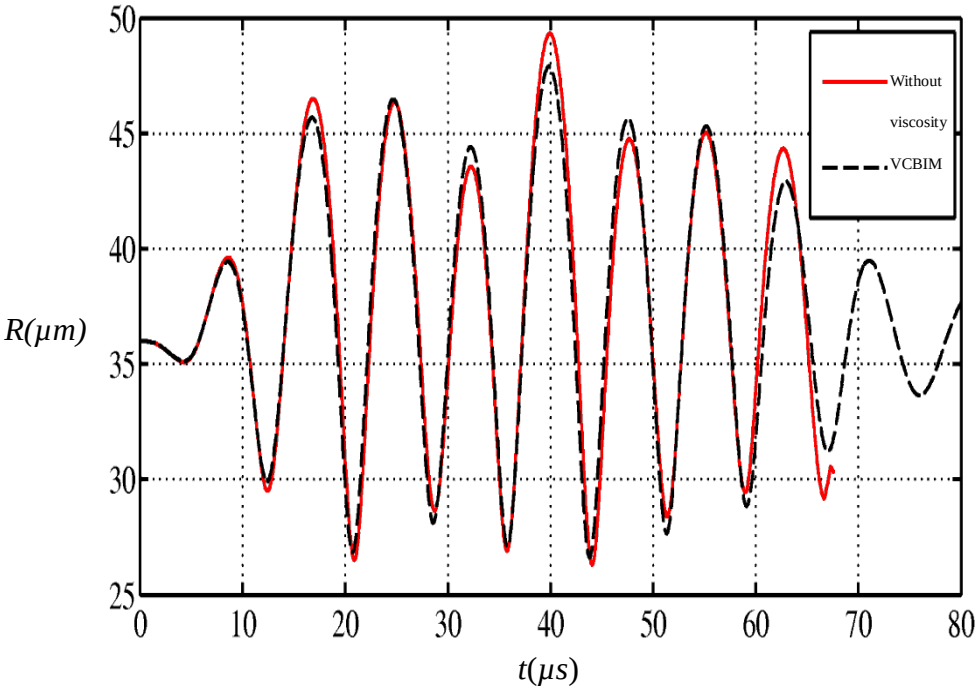

Figure 6.15. Comparison of the computational results between the CIBIM and VCBIM for the bubble radius history for the case in figure 6.5. Dynamics of a bubble with an equilibrium radius R_0 = 30 μm driving by an acoustic wave for pressure amplitude p_a = 40 kPa and frequency f = 130 kHz. The remaining parameters are the same as in Figure 6.5.

Chapter7

SUMMARY, CONCLUSIONS AND FUTURE WORKS

7.1 Summary

The boundary integral method (BIM) based on the incompressible potential flow theory is widely used in simulating bubble dynamics. Using the VCBIM the dimension of the problem reduces by one, and it thus is grid free in the flow domain and costs less CPU time as compared to the domain approaches. However, the compressible effects of liquid are essential, which are associated with acoustic radiation at the inception of a bubble and the end of collapse. Viscous effects may be important for very small bubbles since the Reynolds number associated is often $O(10)$ or larger, and the flow is potential in the bulk volume of the liquid except for a thin viscous boundary layer at the bubble surface.

This thesis is concerned with microbubble dynamics in a viscous compressible liquid near a rigid boundary. The compressible effects are modelled by using the weakly compressible theory of Wang & Blake [103, 104], since the Mach number is relatively small. The viscous effects are approximated using the viscous potential flow theory by Joseph & Wang [29], because the flow field is characterised as being an irrotational flow in the bulk volume but with a thin viscous boundary layer at the bubble surface. Consequently, the phenomenon is modelled by using the viscous compressible boundary integral method, in which the compressible and viscous effects are incorporated into the model through including corresponding additional terms in the far field condition and the dynamic boundary condition

at the bubble surface, respectively.

The following new developments have been carried out in the thesis:

- We developed the compressible viscous BIM for microbubble dynamics using the weakly compressible flow theory and viscous potential flow theory.
- We show that the compressible viscous BIM are shown in good agreement with the Keller-Miksis equation, experiments and computations based on the Navier-Stokes equations.
- Numerical studies were carried out for microbubble dynamics near a rigid wall as well as subject to an acoustic wave. The bubble oscillation, topological transform, jet development and penetration through the bubble and the energy of the bubble system are simulated and analysed in terms of the compressible and viscous effects.

7.2 Conclusions

Some of important features of the bubble dynamics near a rigid boundary have been noticed. A bubble initiated near a rigid boundary may be nearly in contact with the boundary because of its expansion and migration to the boundary, where a thin layer of water forms between the bubble and the boundary thereafter. The pressure in the thin layer of liquid is presented to be approximately constant and equal to the pressure of the bubble gas. The bubble side of the thin layer remains flattened because of surface tension effects. The flow velocity within the thin layer is close to zero.

The bubble starts nearly touching the rigid boundary during the expansion period when $\gamma < 1$,

where γ is the dimensionless standoff distance of the bubble from the boundary in terms of the equivalent maximum bubble radius. This leads to (i) the direct impact of a high speed liquid jet on the boundary once it penetrates through the bubble at the end of collapse, (ii) the direct contact of the bubble ring at high temperature and high pressure at its minimum volume with the boundary, and (iii) the direct impingement of a shock wave on the boundary once it is emitted at the end of collapse. These phenomena have clear potential to damage the boundary. We believe these are possible new mechanisms of cavitation damages.

At the inception of a bubble, the energy of a bubble system loses significantly for a very short time period, which is associated with the emission of a shockwave. This part of energy loss does not depend on the viscous effects and the presence of a rigid boundary. If the Reynolds number is large, the energy remains constant during the most part of oscillation period, where the compressible effects are negligible. The loss of the local energy at the end of collapse increases with the standoff distance. If the Reynolds number is not large, the energy loses gradually due to the viscous effects. At the end of the collapse, the energy decreases rapidly and significantly, when another shockwave emits. For a large Reynolds number, a stronger shockwave emits at the end of collapse.

When subject to an acoustic wave, a microbubble oscillates spherically. Beyond a critical threshold of the acoustic pressure amplitude, surface modes can be produced by acoustic wave after several acoustic cycles. The threshold decreases as the acoustic frequency are equal to the natural frequency of the bubble. As the pressure amplitude increases, the shape mode develops earlier as the bubble is under a larger Bjerknes force. The shape mode of a bubble is activated if the driving acoustic frequency is equal to the natural frequency of the

shape mode.

7.3 Future works

This study is concerned with microbubble dynamics in a compressible viscous liquid for an axisymmetric configuration, using the viscous potential flow theory and weakly compressible theory coupled with the boundary integral method. This modelling can be developed for a three-dimensional configuration since the methodology is suitable for the latter. Another development is to model the heat and mass transfer associated with microbubble dynamics. Heat and mass transfer across the bubble surface can be included in the model Szeri et al. [93]. Other possible important topics in the field include the interaction of multi-bubbles, interaction of a microbubble and a particle, etc.

It is also possible to develop a VCBIM for 3D bubble dynamics. Although the viscous effects have been considered in 3D bubble dynamics, there is no 3D model, which considers both compressible and viscous effects. This could be very useful when the bubble is not axisymmetric, but the compressible effects are not negligible. There could be an important application for cancer detection by using the bubble driving by ultrasound acoustic wave. The difference between the cancer cell and the normal cell is the cancer cell is much harder than the normal cell. Observing the bubble driven by an acoustic wave oscillates near a cell, which could show the different types of oscillations. Then analysing this it could be very useful to detect a cancer cell.

Appendix

A. Calculation of $\partial^2\varphi/\partial n^2$

To calculate normal stress τ_n, $\partial^2\varphi/\partial n^2$ needed can be calculated as follows: We assume a fixed Cartesian coordinate system *O-xyz* and a cylindrical coordinate system *O-rθz*. We define a curve (C) in the *O-rθ* plane parameterised by the arc length s. At a given point (N) on the curve (C), we denote a local Cartesian set by the direct orthonormal basis ($\mathbf{e_n}$, $\mathbf{e_s}$, $\mathbf{e_\theta}$) where $\mathbf{e_n}$, $\mathbf{e_s}$ and $\mathbf{e_\theta}$ are the normal, tangential and circumferential unit vector respectively on the curve. The azimuthal angle along the curvilinear abscissa s in the plane *O-rθ* is *β*.

If we consider a curved surface at each point on a given surface two radii of curvature are need to describe the shape. We can determine these radii at point P the normal to the surface at this point is constructed through the surface containing the normal which will intersect the surface in a plane curve. The radius of the curvature of the curve at P is defined by R_1. If we construct a second plane through the surface which containing the normal and perpendicular to the first plane. This line intersects with surface and the second radius of the curvature R_2 at point P. These two radii define the curvature at P. It is can be shown the mean curvature of the surface $\frac{1}{R_1}+\frac{1}{R_2}$ is constant which is independent of the choice of the planes.

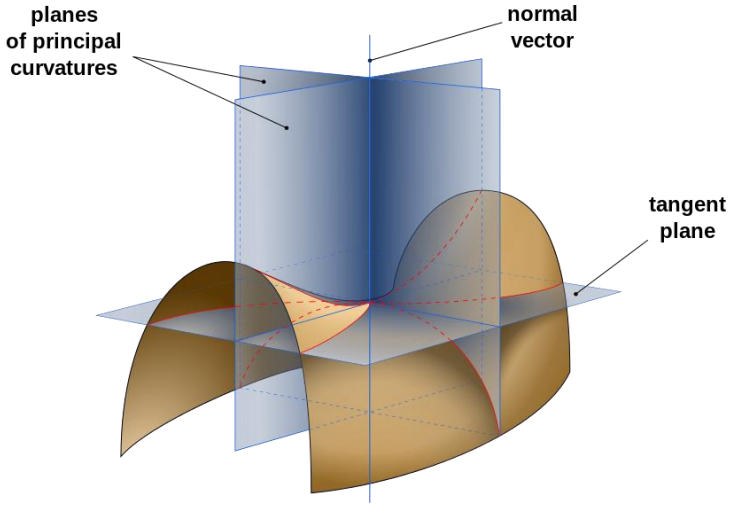

Figure A1. Illustration of the two perpendicular planes cut the surface at a fix point on the plane P. The two radius of the curvature *R1* and *R2* determined the curvature at P completely

We give the expression of the curvature κ in the axisymmetric model. According to the definition of mean curvature and Young-Laplace equation, the local curvature of a certain point on the surface is defined as:

$$\kappa = \kappa_1 + \kappa_2 = \frac{1}{R_1} + \frac{1}{R_2} , \tag{A.1.1}$$

where R_1 and R_2 are corresponding to principle radius of curvature. From the definition of the principal curvature, one has $\kappa_1 = \frac{\partial \beta}{\partial s}$. Let the plane curve be given by Cartesian parametric equation $r = r(t)$ and $z = z(t)$.

$$\kappa_1 = \frac{d\beta}{ds} = \frac{d\beta/dt}{ds/dt} = \frac{d\beta/dt}{\sqrt{\left(\frac{dr}{dt}\right)^2 + \left(\frac{dy}{dt}\right)^2}} = \frac{d\beta/dt}{\sqrt{x'^2 + y'^2}} ,$$

where the β is the tangential angle and s is the arc length. The derivation for the $d\beta/dt$ can be found using the identity

$$\tan\beta = \frac{dr}{dz} = \frac{dr/dt}{dr/dz} = \frac{r'}{z'} ,$$

hence

$$\frac{d}{dt}(\tan\beta)=\sec^2\beta\frac{d\beta}{dt}=\frac{r''z'-z''r'}{z'^2},$$

and

$$\frac{d\beta}{dt}=\frac{1}{\sec^2\beta}\frac{d}{dt}(\tan\beta)=\frac{1}{1+\tan^2\beta}\frac{r''z'-z''r'}{z'^2}=\frac{1}{1+\frac{r'}{z'}}\frac{r''z'-z''r'}{z'^2}=\frac{r''z'-z''r'}{z'^2+r'^2}.$$

Then we combine the above equations gives

$$\frac{r''z'-z''r'}{\left(z'^2+r'^2\right)^{3/2}}=\kappa_1 \tag{A.1.2}$$

The other principle radius of curvature is obtained by extending the normal of the curve to intersect with the z-axis. From analytical geometry, the principle radius of curvatures can be represented by the following equations for an axisymmetric surface:

$$\kappa_1=\frac{r''z'-z''r'}{\left(r'^2+z'^2\right)^{3/2}},\quad \kappa_2=\frac{-z'}{r\left(r'^2+z'^2\right)^{1/2}}, \tag{A.1.3}$$

where r' z' and r'' z'' denote the first and second derivatives with respect to t respectively.

$$\begin{aligned}\nabla^2\varphi&=\left(\mathbf{e_n}\frac{\partial}{\partial n}+\mathbf{e_s}\frac{\partial}{\partial s}+\mathbf{e_\theta}\frac{\partial}{r\partial\theta}\right)\cdot\left(\frac{\partial\varphi}{\partial n}\mathbf{e_n}+\frac{\partial\varphi}{\partial s}\mathbf{e_s}+\frac{\partial\varphi}{r\partial\theta}\mathbf{e_\theta}\right)\\&=\frac{\partial^2\varphi}{\partial n^2}+\frac{\partial\varphi}{\partial s}\frac{\partial\mathbf{e_s}}{\partial n}\mathbf{e_n}+\frac{\partial\varphi}{r\partial\theta}\frac{\partial\mathbf{e_\theta}}{\partial n}\mathbf{e_n}+\frac{\partial\varphi}{\partial n}\frac{\partial\mathbf{e_n}}{\partial s}\mathbf{e_s}+\frac{\partial^2\varphi}{\partial s^2}\\&+\frac{\partial\varphi}{r\partial\theta}\frac{\partial\mathbf{e_\theta}}{\partial s}\mathbf{e_s}+\frac{\partial\varphi}{\partial n}\frac{\partial\mathbf{e_n}}{r\partial\theta}\mathbf{e_\theta}+\frac{\partial\varphi}{\partial n}\frac{\partial\mathbf{e_s}}{r\partial\theta}\mathbf{e_\theta}+\frac{\partial^2\varphi}{r^2\partial\theta^2}\\&=0\end{aligned}$$

$$\frac{\partial \mathbf{e_s}}{\partial n}\mathbf{e_n} = \mathbf{e_n}\cdot\nabla\mathbf{e_s}\cdot\mathbf{e_n} = 0$$
$$\frac{\partial \mathbf{e_n}}{\partial s}\mathbf{e_s} = -\frac{\partial \beta}{\partial s}\mathbf{e_s}\cdot\mathbf{e_s} = -\kappa_1$$
$$\frac{\partial \mathbf{e_n}}{r\partial \theta}\mathbf{e_\theta} = -\frac{n_r}{r}\mathbf{e_\theta}\cdot\mathbf{e_\theta} = \kappa_2\mathbf{e_\theta}\cdot\mathbf{e_\theta} = \kappa_2 \quad ,$$
$$\frac{\partial \varphi}{r\partial \theta} = 0$$
$$\frac{\partial^2\varphi}{\partial n^2} + \frac{\partial^2\varphi}{\partial s^2} - \left(\kappa_1+\kappa_2\right)\frac{\partial\varphi}{\partial n} + \kappa_2\frac{\partial\varphi}{\partial s} = 0\,, \qquad \text{(A.1.4)}$$

$\lim_{r\to 0}\frac{1}{r}\frac{\partial\varphi}{\partial s} = \frac{\partial^2\varphi}{\partial s^2}$ and $n_z = 1$ when

$$\frac{\partial^2\varphi}{\partial n^2} + 2\frac{\partial^2\varphi}{\partial s^2} - \left(\kappa_1+\kappa_2\right)\frac{\partial\varphi}{\partial n} = 0\,. \qquad \text{(A.1.5)}$$

References

1. M. Delius, R. Denk, C. Berding, H. G. Liebich, M. Jordan, and W. Brendel, 1990, "Biological effects of shock waves: Cavitation by shock waves in piglet liver," Ultrasound in medicine & biology, **16**(5), 467-472.

2. E. Klaseboer, C. K. Turangan, B. C. Khoo, A. J. Szeri, M. L.Calvisi, G. N. Sankin, and P. Zhong, 2007, "Interaction of lithotripter shockwaves with single inertial cavitation bubbles," J. Fluid Mech. **593**, 33–56.

3. J. I. Iloreta, N. Fung, and A. J. Szeri, 2008, "Dynamics of bubbles near a rigid surface subjected to a lithotripter shock wave. Part 1. Consequences of interference between incident and reflected waves," J. Fluid Mech. **616**, 43–61.

4. M. L. Calvisi, J. I. Iloreta and A. J. Szeri, 2008, "Dynamics of bubbles near a rigid surface subjected to a lithotripter shock wave: II. Reflected shock intensifies non-spherical cavitation collapse," J. Fluid Mech. 616, 63–97.

5. W. W. Roberts, T. L. Hall, K. Ives, J. S. Wolf Jr, J. B. Fowlkes, and C. A. Cain, 2006, "Pulsed cavitational ultrasound: a noninvasive technology for controlled tissue ablation (histotripsy) in the rabbit kidney," The Journal of urology, **175**(2), 734-738.

6. C. Coussios and R. A. Roy, 2008, "Applications of acoustics and cavitation to noninvasive therapy and drug delivery," Ann. Rev. Fluid Mech. **40**, 395-420.

7. G. A. Curtiss, D. M. Leppinen, Q. X. Wang and J. R. Blake, 2013, "Ultrasonic cavitation near a tissue layer," J. Fluid Mech. **730**, 245-272.

8. T. A. Leslie, and J. E. Kennedy, 2006, "High-intensity focused ultrasound principles, current uses, and potential for the future," Ultrasound Quart **22**:263–272.

9. K. S. Suslick, Sonochemistry. 1990, Science 247, 1439–1445.

10. W. D. Song, M. H. Hong, B. Lukyanchuk & T. C. Chong, 2004, “Laser-induced cavitation bubbles for cleaning of solid surfaces,” J. Appl. Phys. **95** (6), 2952.

11. C. D. Ohl, M. Arora, R. Ikink, N. de Jong, M. Versluis, M. Delius & D. Lohse, 2006a, “Sonoporation from jetting cavitation bubbles,” Biophys. J. **91**, 4285-4295.

12. J. R. Blake, B. B. Taib & G. Doherty, 1986, “Transient cavities near boundaries. Part 1. Rigid Boundary,” J. Fluid Mech. **170**, 497.

13. J. R. Blake, B. B. Taib & G. Doherty, 1987, “Transient cavities near boundaries. Part 2. Free surface,” J. Fluid Mech. **181**, 197.

14. G. L. Chahine & T. O. Perdue, 1988, “Simulation of the three-dimensional behaviour of an unsteady large bubble near a structure,” in Proc. 3rd Intl Colloq. on Drops and Bubbles, edited by Taylor G. Wang, (American Institute of Physics, New York).

15. M. L. Calvisi, O. Lindau, J. R. Blake and A. J. Szeri, 2007, “Shape stability and violent collapse of microbubbles in acoustic traveling waves,” Phys. Fluids **19**, 047101.

16. Q. X. Wang and J. R. Blake, 2010, “Non-spherical bubble dynamics in a compressible liquid. Part 1. Travelling acoustic wave,” J. Fluid Mech. **659**, 191-224.

17. Q. X. Wang & J. R. Blake, 2011, “Non-spherical bubble dynamics in a compressible liquid. Part 2. Acoustic standing wave,” J. Fluid Mech. **679**, 559-581.

18. E. Klaseboer & B. C. Khoo, , 2004a, “Boundary integral equations as applied to an oscillating bubble near a fluid-fluid interface,” Computational Mechanics **33**, 129–138.

19. E. Klaseboer & B. C. Khoo, 2004b, “An oscillating bubble near an elastic material,” Journal of Applied Physics **96** (10), 5808–5818.

20. S. W. Fong, E. Klaseboer, C. K. Turangan, B. C. Khoo, & K. C. Hung, 2006, “Numerical analysis of a gas bubble near biomaterials in an ultrasound field,” Ultrasound in Medicine and Biology **32** (6), 925–942.

21. S. W. Fong, E. Klaseboer & B. C. Khoo, 2008, “Interaction of microbubbles with high intensity pulsed ultrasound,” J. Acoust. Soc. Am. **123**(3), 1784- 1793.

22. Q. X., Wang, and K. Manmi. 2014, “Three dimensional microbubble dynamics near a wall subject to high intensity ultrasound." Physics of Fluids (1994-present) **26**.3: 032104.

23. S. Popinet, and S. Zaleski, 2002, “Bubble collapse near a solid boundary: a numerical study of the influence of viscosity,”. Journal of Fluid Mechanics, **464**, 137-163.

24. S. J. Lind, and T. N. Phillips, 2012, “The influence of viscoelasticity on the collapse of cavitation bubbles near a rigid boundary,”. Theoret. & Comput. Fluid Dyn., **26**(1-4), 245-277.

25. Gilmore, F. R. 1952, The growth or collapse of a spherical bubble in a viscous compressible liquid, Report or Paper (Technical Report).

26. Plesset M. S. & Prosperetti A. 1997, Bubble dynamics and cavitation. Annual Review of Fluid Mechanics, 9(1), 145-185.

27. S. J. Kim, K. H. Lim, & C. Kim, 2006, “Deformation characteristics of spherical bubble collapse in Newtonian fluids near the wall using the finite element method with ALE formulation,”. Korea-Australia Rheology Journal, **18**(2), 109-118.

28. V. Minsier, J. De Wilde, and J. Proost, 2009, “Simulation of the effect of viscosity on jet penetration into a single cavitating bubble,”. Journal of Applied Physics, **106**(8), 084906.

29. D. D. Joseph, and J. Wang, 2004, “The dissipation approximation and viscous potential flow,” Journal of Fluid Mechanics, **505**, 365-377.

30. A. M. Zhang and B. Y. Ni, 2014, “Three-dimensional boundary integral simulations of motion and deformation of bubbles with viscous effects,” Computers & Fluids **92**, 22-33.

31. Lamb, Hydrodynamics (6th Ed.), Cambridge University Press 1932.

32. Q. X. Wang, 1998, “The evolution of a gas bubble near an inclined wall,” Theor. Comput. Fluid Dyn. 12(1):29–51.

33. Q. X. Wang, 2004, “Numerical modelling of violent bubble motion,” Phys. Fluids 16 (5), 1610-1619.

34. Q. X. Wang. 2005, Unstructured MEL modelling of unsteady nonlinear ship waves. J. Comput. Phys. 210 (1) 183-224.

35. C. Wang, B. C. Khoo & K. S. Yeo, 2003, “Elastic mesh technique for 3D BIM simulation with an application to underwater explosion bubble dynamics,” Computers & fluids, 32(9), 1195–1212.

36. Y. L. Zhang, K. S. Yeo, B. C. Khoo, and C. Wang, 2001, “3D jet impact and toroidal bubbles,” J. Comput. Phys. 166, 336–360.

37. C. Wang, & B. C. Khoo, 2004, “An indirect boundary element method for three dimensional explosion bubbles,” J. of Comput. Phy. 194(2), 451–480.

38. Ohl, C. D., Arora, M., Dijkink, R., Janve, V., & Lohse, D. 2006, Surface cleaning from laser-induced cavitation bubbles. Applied physics letters 89(7), 074102.

39. Benjamin, T. B. and Ellis, A. T. 1966, The collapse of cavitation bubbles and the pressure thereby produced against solid boundaries. Phil. Trans. R. Soc. Lond. A **260** 221–40.

40. Best, J. P. 1993, The formation of toroidal bubbles upon collapse of transient cavities. *J. Fluid Mech*. **251**, 79-107.

41. Blake, J. R. and Gibson, D. C. 1987, Cavitation bubbles near boundaries. Annu. Rev. Fluid Mech. **19**, 99-123.

42. Blake, J. R., Hooton, M. C., Robinson, P. B. and Tong, P. R. 1997, Collapsing cavities, toroidal bubbles and jet impact. *Phil. Trans. R. Soc. Lond*. A **355**, 537-550.

43. Blake, J. R., Taib, B. B. and Doherty, G. 1986, Transient cavities near boundaries. Part 1. Rigid boundary. J. Fluid Mech. **170**, 479.

44. Brennen, C. E. 1995, Cavitation and Bubble Dynamics, Oxford University Press (available online).

45. Brujan E.A., Nahen K., Schmidt P. and Vogel A. 2001, Dynamics of laser induced cavitation bubbles near elastic boundaries: influence of the elastic modulus. J. Fluid Mech. 433, 283–314.

46. Brujan, E. A. and Matsumoto, Y. 2012, Collapse of micrometer-sized cavitation bubbles near a rigid boundary. Microfluid Nanofluid, **13**, 957–966.

47. Calvisi, M. L., Iloreta, J. I. and Szeri, A. J. 2008, Dynamics of bubbles near a rigid surface subjected to a lithotripter shock wave: II. Reflected shock intensifies non-spherical cavitation collapse. J. Fluid Mech. **616** 63–97.

48. Chahine, G.L. and Bovis, A. 1980, Oscillation and collapse of a cavitation bubble in the vicinity of a two-liquid interface. Cavitation and Inhomogeneities in Underwater Acoustics, Springer-Verlag ed. New York, pp. 23-29.

49. Chahine G.L. and Harris G. 1998, Multi-Cycle underwater explosion bubble model. Part I: Theory and validation examples for free-field bubble problems. U.S. Naval Surface Warfare Center Indian Head Division, Report IHCR 98-64.

50. Chahine, G.L. and Harris, G. 1998, Multi-Cycle underwater explosion model. Part II: Validation Examples for Hull Girder Whipping Problems. U.S. Naval Surface Warfare Center Indian Head Division, Report IHCR 98-65.

51. Chahine, G. L. and Perdue, T. O. 1988, Simulation of the three-dimensional behaviour of an unsteady large bubble near a structure. In Proc. 3rd Intl Colloq. on Drops and Bubbles, Monterey, CA.

52. Cole, R. H. 1948, Underwater Explosions. Princeton University Press.

53. Coussios, C. C. and Roy, R. A. 2007, Applications of Acoustics and Cavitation to Non-invasive Therapy and Drug Delivery. Annu. Rev. Fluid Mech. **40**, 395-420.

54. Curtiss, G. A., Leppinen, D. M., Wang, Q. X. and Blake, J. R. 2013, Ultrasonic cavitation near a tissue layer. J. Fluid Mech. 730, 245-272.

55. Delius, M. 1990, Effect of lithotripter shock waves on tissues and materials. In Proc. 12th ISNA: Frontiers of Nonlinear Acoustics (ed. M. F. Hamilton and D. T. Blackstock), 31-46. Elsevier.

56. Duncan, J. H., Milligan, C. D. and Zhang, S. G. 1996. On the interaction between a bubble and a submerged compliant structure. J. Sound & Vibration **197** (1), 17-44.

57. Duncan, J. H. and Zhang, S. G. 1993, On the interaction of a collapsing cavity and a

compliant wall. J. Fluid Mech. **226**, 401-423.

58. Guerri, L., Lucca, G. and Prosperetti, A. 1981, A numerical method for the dynamics of non-spherical cavitation bubbles. Proc. 2nd Int. Colloq. on Drops and Bubbles (California), p. 175.
59. Hung, C. F. and Hwangfu, J. J. 2010, Experimental study of the behavior of mini-charge underwater explosion bubbles near different boundaries. J. Fluid Mech. **651**, 55-80.
60. Iloreta J. I., Fung, N. M. and Szeri A. J. 2008, Dynamics of bubbles near a rigid surface subjected to a lithotripter shock wave: I. Consequences of interference between incident and reflected waves J. Fluid Mech. **616**, 43–61.
61. Jayaprakash, A. Chao-Tsung, H. and Chahine, G. 2010, Numerical and experimental study of the interaction of a spark-generated bubble and a vertical wall. J. Fluids Engineering **134** (3), 031301-1.
62. Jayaprakash, A., Singh, S. and Chahine, G. 2011, Experimental and Numerical Investigation of Single Bubble Dynamics in a Two-Phase Bubbly Medium. J. Fluids Engineering **133**, 121305.
63. Kornfeld, M. & Suvorov, L. 1944, On the destructive action of cavitation. J. Appl. Phys. 15, 495-506.
64. Klaseboer, E., Fong, S. W., Turangan, C. K., Khoo, B. C., Szeri, A. J., Calvisi, M. L., Sankin, G. N. and Zhong, P. 2007, Interaction of lithotripter shockwaves with single inertial cavitation bubbles J. Fluid Mech. **593**, 33–56.
65. Klaseboer, E., Hung, K. C., Wang, C., Wang, C. W., Khoo, B. C., Boyce, P., Debono,S and Charlier, H. 2005, Experimental and numerical investigation of the dynamics of an underwater explosion bubble near a resilient/ rigid structure. J. Fluid Mech. **537**, 387–413.

66. Lauterborn, W. and Bolle, H. 1975, Experimental investigations of cavitation-bubble collapse in the neighbourhood of a solid boundary J. Fluid Mech. **72**, 391–9.

67. Lauterborn, W. and Kurz, T. 2010, Physics of bubble oscillations. Rep. Prog. Phys. **73**, 10650.

68. Lauterborn, W. and Ohl, C. D. 1997, Cavitation bubble dynamics. Ultrasonics Sonochem. 4, 65–75.

69. Lauterborn, W. and Vogel, A. 2013, Shock wave emission by laser generated bubbles. In Bubble Dynamics & Shock Waves (ed. C.F. Delale), 67-103. Springer-Verlag Berlin Heidelberg.

70. Lee, M., Klaseboer, E. and Khoo B. C. 2007, On the boundary integral method for the rebounding bubble. J. Fluid Mech. **570**, 407–429.

71. Lenoir, M. 1979, A calculation of the parameters of the high-speed jet formed in the collapse of a bubble. J. Applied Mech. Technical Phys. **20**(3), 333-337.

72. Lezzi, A. and Prosperetti, A. 1987, Bubble dynamics in a compressible liquid. Part. 2. Second-order theory. J. Fluid Mech. **185**, 289-321.

73. Leslie, T. A. and Kennedy, J. E. 2006, High-intensity focused ultrasound principles, current uses, and potential for the future. Ultrasound Quart **22**, 263–272.

74. Leighton, T. 1994, The Acoustic Bubble. Academic Press, London.

75. Leighton, T. G., Turangan, C.K., Jamaluddin, A.R., Ball, G.J. and White, P.R. 2013, Prediction of far-field acoustic emissions from cavitation clouds during shock wave lithotripsy for development of a clinical device. Proceedings of the Royal Society A: Mathematical, Physical and Engineering Sciences, 469, (2150), 20120538-[21pp].

76. Leighton, T. G., Fedele, F., Coleman, A. J., McCarthy, C., Ryves, S., Hurrell, A. M., De Stefano, A. and White, P. R. 2008, A passive acoustic device for real-time monitoring the efficacy of shockwave lithotripsy treatment. Ultrasound in Medicine & Biology, 34, (10), 1651-1665.

77. Lind, S. J. and Phillips, T. N. 2010, The effect of viscoelasticity on a rising gas bubble. *Journal of non-Newtonian fluid mechanics* 165(15-16), pp. 852-865.

78. Lind, S. J. and Phillips, T. N. 2013, The effect of viscoelasticity on the dynamics of gas bubbles near free surfaces. *Physics of Fluids* 25(2), pp. 022104-022135.

79. Lindau, O. and Lauterborn, W. 2003, Cinematographic observation of the collapse and rebound of a laser-produced cavitation bubble near a wall. J. Fluid Mech. **479**, 327–48.

80. Ni, B.Y., Zhang, A. M. and Wu, G.X. 2014, Numerical and experimental study of bubble impact on a solid wall. To be published in J. Eng. Flulids.

81. Pearson, A., Blake, J. R. and Otto, S. R. 2004, Jets in bubbles. J. Eng. Math. **48** (3-4), 391-412,.

82. Philipp, A. and Lauterborn, W. 1998, Cavitation erosion by single laser-produced bubbles. J. Fluid Mech. **361**, 75–116.

83. Plesset, M. S. and Chapman, R. B. 1971, Collapse of an initially spherical vapour cavity in the neighbourhood of a solid boundary. J. Fluid Mech. **47**, 283-290.

84. Plesset, M. S. and Prosperetti, A. 1977, Bubble dynamics and cavitation. Ann. Rev. Fluid Mech. **9**. 145-185.

85. Prosperetti, A. and Lezzi, A. 1986, Bubble dynamics in a compressible liquid. Part. 1. First-order theory. J. Fluid Mech. **168**, 457-478.

86. Ohl, C. D., Arora, M., Ikink, R., de Jong, N., Versluis, M., Delius M. & Lohse, D. 2006, Sonoporation from jetting cavitation bubbles. Biophys. J. 91, 4285-4295.

87. Rayleigh, Lord. 1917, On the pressure developed in a liquid during the collapse of a spherical cavity. Phil. Mag. **34**, 94–98.

88. Roberts, W. W., Hall T. L., Ives, K., Wolf, J. S., Fowlkes, J. B. and Cain, C. A. 2006, Pulsed cavitational ultrasound: a noninvasive technology for controlled tissue ablation (histotripsy) in the rabbit kidney. J. Urol. **175**, 734–738.

89. Shima, A., Takayama, K., Tomita, Y. and Miura, N. 1981, An experimental study on effects of a solid wall on the motion of bubbles and shock waves in bubble collapse. Acustica 48, 293-301.

90. Song, W.D., Hong, M.H., Luk'yanchuk, B. and Chong, T.C., 2004, Laser-induced cavitation bubbles for cleaning of solid surfaces. J. Appl. Phys. **95** (6): 2952.

91. Suslick, K. S. 1990, Sonochemistry. Science 247, 1439–1445.

92. Suslick, K. S. & Crum, L. A. 1997, Encyclopedia of Acoustics (ed. Crocker, M. J.) 271-282 Wiley-Interscience, New York.

93. Szeri, A. J., Storey, B. D., Pearson, A. and Blake, J. R. 2003, Heat and mass transfer during the violent collapse of nonspherical bubbles. Phys. Fluids **15**, 2576–2586.

94. Taylor, G. I. 1942, Vertical motion of a spherical bubble and the pressure surrounding it. In Underwater Explosion Research, **2**, 131–144, Office of Naval Research, Washington, DC.

95. Tomita, Y. and Shima, A. 1986, Mechanisms of impulsive pressure generation and damage pit formation by bubble collapse. J. Fluid Mech. **169**, 535–564.

96. Vogel, A., Lauterborn, W. and Timm, R. 1989, Optical and acoustic investigations of the

dynamics of laser-produced cavitation bubbles near a solid boundary. J. Fluid Mech. **206**, 299–338.

97. Vogel, A., Schweiger, P., Frieser, A., Asiyo, M. and Birngruber, R. 1990, Intraocular Nd:YAG laser surgery: damage mechanism, damage range and reduction of collateral effects. IEEE J. Quant. Electr. **26**, 2240-2260.
98. Wang, Q. X. 1998, The numerical analyses of the evolution of a gas bubble near an inclined wall. Theoret. & Comput. Fluid Dyn. **12**, 29-51.
99. Wang, Q. X. 2004, Numerical modelling of violent bubble motion. Phys. Fluids **16** (5), 1610-1619.
100. Wang, Q. X. 2013, Underwater explosion bubble dynamics in a compressible liquid. Phys. Fluids **25**, 072104.
101. Wang, Q. X. 2014, Multi-oscillations of a bubble in a compressible liquid near a rigid boundary, J. Fluid Mech. 745, 509-536.
102. Wang, Q. X. 2015, Where does the energy of a violently collapsing bubble system go? Submitted to J. Fluid Mech.
103. Wang, Q. X. and Blake, J. R. 2010, Non-spherical bubble dynamics in a compressible liquid. Part 1. Travelling acoustic wave. J. Fluid Mech. **659**, 191-224.
104. Wang, Q. X. and Blake J. R. 2011, Non-spherical bubble dynamics in a compressible liquid. Part 2. Acoustic standing wave. J. Fluid Mech. **679**, 559-581.
105. Wang, Q. X. & Manmi K. 2014, Microbubble dynamics near a wall subjected to a travelling acoustic wave. Phys. Fluids 26, 03.
106. Wang, Q. X., Yeo, K. S., Khoo, B. C. and Lam, K. Y. 1996, Nonlinear interaction between gas bubble and free surface. Computers & Fluids **25** (7), 607.

107. Wang, Q. X., Yeo, K. S., Khoo, B. C. and Lam, K. Y. 1996, Strong interaction between buoyancy bubble and free surface. Theor . Comput. Fluid Dyn. **8**, 73.

108. Wang, Q. X., Yeo, K. S., Khoo, B. C. and Lam, K. Y. 2005, Vortex ring modelling for toroidal bubbles. Theoret. & Comput. Fluid Dyn. **19** (5), 303-317.

109. Yang, Y. X., Wang, Q. X. and Keat, T. S. 2013, Dynamic features of a laser-induced cavitation bubble near a solid boundary. Ultrasonics Sonochemistry 01.

110. Young, F. R. 1989, Cavitation. McGraw-Hill.

111. Zhang, S. G. and Duncan, J. H. 1994, On the non-spherical collapse and rebound of a cavitation bubble. Phys. Fluids **6** (7), 2352–2362.

112. Zhang, S. G., Duncan, J. H., and Chahine G. L. 1993, The final stage of the collapse of a cavitation bubble near a rigid wall. J. Fluid Mech. **257** 147-181.

113. Zhang, Y. and Li, S. C, 2014, Mass transfer during radial oscillations of gas bubbles in viscoelastic mediums under acoustic excitation. Int. J. Heat Mass Transfer, 69, 106-116,.

114. Zhang, Y. L., Yeo, K. S. Khoo, B. C. and Wang, C. 2013, D jet impact and toroidal bubbles. J. Comput. Phys. 166 (2), 336–360.

115. Boulton-Stone JM, Blake JR. 1993, Gas bubbles bursting at a free surface. J Fluid Mech, 254:437–66.

116. Moore DW. 1963, The boundary layer on a spherical gas bubble. J Fluid Mech, 6:113–30.

117. E. A. Brujan, G. S. Keen, A. Vogel, and J. R. Blake, 2002, The final stage of the collapse of a cavitation bubble close to a rigid boundary. Phys. Fluids 14 (1) 85.

118. J. R. Blake and D. C. Gibson, 1981, Growth and collapse of a vapour cavity near a free surface, J. Fluid Mech, 111, 123.

119. M. Versluis, David E. Goertz, Peggy Palanchon, Ivo L. Heitman, Sander M. van der Meer, Benjamin Dollet, Nico de Jong, and Detlef Lohse, 2010, Microbubble shape oscillations excited through ultrasonic parametric driving, Phyical Review E 82, 026321.

120. P. C. Palanchon, 2004, PhD thesis, Ultrasound harmonic classification of microemboli, Dept. of Experimental Echocardiograph, Thoraxscentre, Erasmus MC, the Netherland,.

121. Y. L. Chen and J. Israelachvili. 1991, New mechanism of cavitation damage. Science, 252:1157-1160.

122. Stroud, A. H. and Secrest, D, 1966, Gaussian Quadrature Formulas, Prentice-Hall, Englewood Cliffs, N. Y.

123. K Manmi, QX Wang, 2017, Acoustic microbubble dynamics with viscous effects. Ultrasonics Sonochemistry, 36, 427-436.

124. T. J. Pedley, 1968, On the instability of viscous flow in a rapidly rotating pipe. J. Fluid Mech, 35, 97-115.

125. T. S. Lundgren, N. N. Mansour, 1991, Vortex ring bubbles. J. Fluid Mech, 224, 177-196.